EFFECT OF PLASTIC DEFORMATION ANISOTROPIES
ON SHOCK-INDUCED PHASE TRANSITIONS
IN METALLIC SINGLE CRYSTALS

PUNAM GHIMIRE

Department of Physics

APPROVED:

Ramon Ravelo, Chair, Ph.D.

Jorge Lopez, Ph.D.

Rajendra Zope, Ph.D.

Cesar Carrasco, Ph.D.

Charles Ambler, Ph.D.
Dean of the Graduate School

To my

parents whose unwavering support from 8400 miles away has kept me sane in the past 4 years.

EFFECT OF PLASTIC DEFORMATION ANISOTROPIES ON SHOCK-INDUCED PHASE TRANSITIONS IN METALLIC SINGLE CRYSTALS

by

PUNAM GHIMIRE

THESIS

Presented to the Faculty of the Graduate School of

The University of Texas at El Paso

in Partial Fulfillment

of the Requirements

for the Degree of

MASTER OF SCIENCE

Department of Physics

THE UNIVERSITY OF TEXAS AT EL PASO

Acknowledgements

My relationship with you has been a tumultuous one. I have loved you and hated you. I have craved you and been averse of you. There have been giggles and tears, sleepless nights and mindless days. When I was new, I felt trapped, imprisoned, desperate to get out, but from a labyrinth without a clue. At times, I felt you crushed my vision and made me hopeless, you changed me who I was and made me insane. In this city of dead dream with a dead ends, I felt great deal of my life as wasted. Later, during some semblance of transient hope, I noticed I was pushed back to a distant and it was the last place I ever wanted to go.

Things are different now, we have both grown up and understand each others expectations. Today, I can look back and boast of my own independence. Thank you for excruciating life and lessons you taught me along the way. Next time when I visit you, I will visit you on my own terms dear El Paso; to explore the city and meet the warmest people who have added essence to my life.

Dr. Ramon Ravelo: I must express my heart-felt gratitude to my thesis adviser Dr. Ramon Ravelo for his unending support and academic parenting. You persistently held my best interests at heart, and overturned the countless hurdles as you helped me finish my study at UTEP.

You met me at the worst point of my life while I was in the midst of quiet desperation, a thought that has always repelled me. I am so grateful that I have/had you as my adviser, as you carried me through a time while I was incompetent and uncommitted. Despite my hopelessness, you have shone a light on me and brightened me with a positive shift in my attitude through various questions/conversations. These two and half years of working in

research under your supervision have been an eye opening experience. I experienced failure that I had never imagined before, found myself suddenly without passion for what I was doing and watched myself slipping away from my commitments. I have fathomed the depth of my weaknesses and tested the intensity of my true desire for success. Yet, most importantly, after years of denial, I have internalized that there was only one thing that was keeping me from doing what I wanted to do- MYSELF! In retrospect, I reflect: they taught me priceless lessons for my life.

Certainly, without your enduring patience, there would be no research and hence no thesis. I am emotionally and intellectually indebted to you forever for reconciling with me along the way and still guiding me through this research. But most of all, that indefinable divine influence you had on my life can never be etched away from my very core.

Dr. Vivian Incera: The inimitable influence, whom I significantly missed over past 3 years here. You inspired me and I came from afar with a new vision to embark on new lessons of life on this land of opportunity. What we saw in each-other was once Real, and that can't be denied, but life often takes a diverging course as our perception and reality do not envelope, we get along with some and fall apart with others...that I understand... I wish with all my might that things be different between us, but I accept what can't be changed, as we think differently. I will always remember you as the initial role model... I am thankful to you for your support during the outset of my career at UTEP, without which I would not be here today writing this thesis.

Dr. Eric Hagedorn: His unconditional supports are priceless! I am grateful to him for the rest of my life.

Without thanking **UTEP Campus Police**, my acknowledgement will remain incomplete. I want to thank the Campus Police team for countless rides from UTEP to my apartment,

whether on windy nights or the solitude of a cold morning at 5:00 AM.

Thesis Committee Members: Additionally, I wish to thank members of my thesis committee, Dr. Jorge Lopez and Dr. Rajendra Zope of the Physics Department and Dr. Cesar Carrasco of the Civil Engineering Department, all at the University of Texas at El Paso.

Friends/Family: Henry Moncada Lopez, a good friend of mine and my current roommate: you have been my adviser away from my thesis adviser. Perhaps because we shared similar passion for learning and science, I have always learned something new from you. I am very grateful to you for helping me and encouraging me at times, and criticizing when needed. Without hospitable gestures extended by yourself and my other roommates Surendra, Mukunda and Kamal, I would not have completed my thesis this semester. Thank you all for accommodating me in your apartment with such short notice.

Thanks to my colleague Madawa for intellectually stimulating talks and teaching me how to think like a computational scientist. Additionally, I am grateful to my friends; Gerard Ross for letting me sleep in his couch and Courtney Boss for letting me stay in her house while I was in the white-heat of poverty.

And I want to thank my mother-in-law whose support during my return to El Paso has especially provided me with great strength.

Ryan Lee: And finally I must thank my dear husband Ryan Lee. You deserve a Nobel Prize for putting up with my frustration and adamant, and still continually loving and supporting me. What I feel for you is deep and I can not express it all here. All I want to say is I love you baby with all my heart!

Collaborators / Research Agencies: Special thanks to our collaborator Dr. Timothy Germann, from Los Alamos National Laboratory for providing us with the rendering and visualization routines used to generate the orientation images. Additionally, I want to acknowledge Dr. Alex Stukowski, who provided us with the crystal analysis tool (CAT), mentioned in this thesis.

We acknowldege support from the Air Force Office of Scientific Research, under AFOSR Award FA9550-12-1-0476, and The University of Texas at El Paso, which supported a part of my research for a semester (Spring 2014) under COS Grant No. 14-7000-6453.

Abstract

Most metals and alloys undergo plastic deformation at shear stresses and/or pressures in the kbars regime. On the other hand, typical pressure-induced structural transitions, take place at much higher pressures, in the tens of GPa range. Surprisingly, there has not been to date, a systematic study on the role plastic deformation plays on the dynamics of defect-mediated phase transformations. The main purpose of this work was to investigate via atomistic simulations, the contribution of pre-existing defect densities on the kinetics of structural transformations under dynamic loading. We have carried out molecular dynamics simulations –including large-scale non-equilibrium molecular dynamics (NEMD), of defect-mediated phase transformations under shock and quasi-isentropic compression (QIC). An analytical embedded atom method (EAM) description is used to model a fcc-bcc phase transition (PT) boundary chosen to occur below or above the elastic-plastic threshold in order to model systems undergoing a PT with and without plasticity. As expected, for conditions in which plastic deformation precedes the phase transformation, the defect-mediated PT proceeds at faster rates than the corresponding defect-free ones. The bcc fraction growth rate can be correlated with a sharp decrease in the dislocation densities originally present in the parent phase.

Table of Contents

List of Tables

List of Figures

Introduction

A solid material can be stretched, bent or compressed depending upon the external force applied to a body. Under the action of such force, the material undergoes displacements and deformation, and produces internal forces. A measure of deformation is defined as strain. The intensity of internal forces is termed as stress. These properties strains, stresses and the displacements in a deformable body are interlinked. Thus, whenever external load is applied to a system, there is a resultant strain; similarly, whenever a system is strained in some way, there is then some stress upon the system. Specifically, the way metallic materials deform depends primarily upon the elastic properties of the constituent crystalline materials. In particular, the speed of body waves passing through a material is entirely dependent upon the elastic coefficients, material's density and the crystallographic direction in which external load is applied.

Deformation of crystalline materials under extreme environments (pressures in upwards of hundreds of GPa, temperatures in 1000's of degrees Kelvin, strain rates $> 10^8$ s^{-1}) depends on underlying microscopic process such as plastic deformation, structural transformations and melting. The material strength and durability is determined by defect mediated interactions and the response of the defects to external effects such as shock waves. Generally, shock waves are a type of propagating disturbances which are supersonic in nature that leads to large changes in compression, density, particle velocity, pressure and internal energy in almost a discontinuous manner. The velocity of a shock wave is intimately dependent on the elastic constants of the material which are pressure dependent. This explains why waves speed is faster in high pressure condition in comparison to its value at room temperature and pressure (RTP) conditions. When the material is subjected to shock wave compression, it deforms quasi-uniaxially and the resulting uniaxial strain rate can create a tri-axial stress state in the material. The loading achieved during plate impacts, high intensity laser experiments or explosives are few example of high strain rate loading. In the case of high strain rates of compression, interaction between shock wave

and accompanied plastic deformation play a major role in the resulted micro-structure and the material behavior.

The study of material response subjected to high strain rates of deformation (typically rates $> 10^6\ s^{-1}$ is attractive due to its many industrial, transportation and defense application[1] involving shock and impacts. Therefore, it is very important to understand the behavior of materials under static, quasi-static, and dynamic thermochemical extremes. This motivates one to look at the motion of atoms and electrons within a material under extremes to gain insight into defect production and eventual evolution into micro-structural components, such as dislocations, voids, and grain boundaries. Experimentally, it is not easy to get data at these high deformation rates because of the measurement of deformation mechanism at such high rates (meaning short time scales) is difficult[2]. The advancement in the high-pressure x-ray diffraction technique, in implementing Diamond Anvil Cell (DAC) along with the advancement in numerical simulation have enhanced the way for better understanding of crystal phase-stability dramatically. However, there are numerous issues that remain in our current understanding of materials at extreme conditions in metal. For example, Iron has a body-centred cubic (bcc) ground state ($\alpha - Fe$) and undergoes a structural transition to hexagonal close-packed (hcp) phase ($\epsilon - Fe$) in a pressure-induced transition around 13GPa at room temperature. Experiment in polycrystalline iron shows a structural phase transition ($\alpha - \epsilon$) which is preceded by plasticity. However, the recent atomistic simulations performed by Gunkelmann et. al.[3] could not detect the occurrence of any plastic activity before the phase change in iron. Therefore, in our research we wanted to investigate the role of plasticity in the phase transformation of face-centred cubic (fcc) metallic single crystals under extreme case.

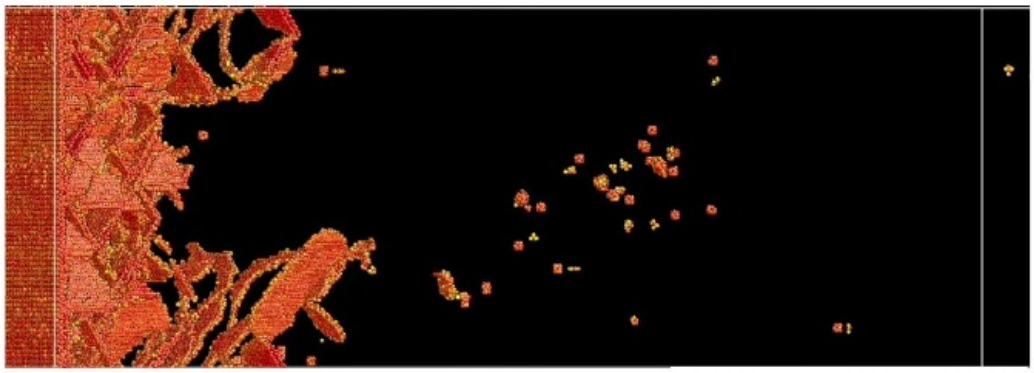

Figure 1: Embedded atom method (EAM) Cu model, Mishin et. al. PRB 63, 224106(2002). Shock simulations: Low density of pre-existing defect, Ravelo et al, 2009

We start our discussion by defining few terms that are important to understand the concept behind material's mechanical behavior. Before we go into detail of the mechanical properties of solids, lets carry out some thought experiment. Consider a cylindrical test specimen of length L with A_0 as its cross-sectional area. Let F be the applied load which elongates the specimen by δL. We plot the graph of tensile force per unit area (stress) versus strain, as shown below in the figure. In the graph Fig. 2, the region where tensile load is linearly proportional to the elongation is called proportional range. Now, the removal of applied load (also refer as unloading) results in retrieving of the original length. The property of a material to regains its original shape/length after removal of applied force is what we called elasticity. However, the application of much larger load than F and its removal will result in the extra length and leaves body with a permanent elongation. Engineers use engineering tension test to understand the basic design information regarding the material's strength and as an acceptance test for the material's specification. Tensile strength, yield strength, percent elongation or reduction of area are important areas in which engineers pay close attention. During such test, an specimen is subjected to continuous increasing uniaxial tensile force and the change of length of specimen is observed. One of such typical

stress-strain curve for metal is as shown below.

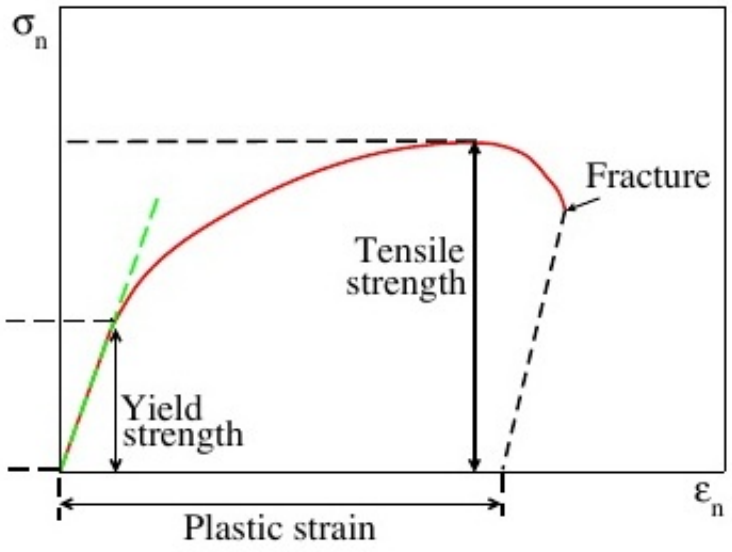

Figure 2: A tensile stress-strain curve.

1. **Elastic Limit:** The elastic limit is the limit beyond which the material will no longer go back to its original shape when the load is removed, or it is the maximum stress that may be developed such that there is no permanent or residual deformation when the load is entirely removed.

2. **Yield strength:** The maximum stress that can be applied without exceeding a specified value of permanent strain.

3. **Modulus of elasticity:** It is the slope of the initial linear portion of the stress-strain diagram. The modulus of elasticity may also be characterized as the 'stiffness' or ability of a material to resist deformation within the linear range.

4. **Ultimate strength:** The maximum stress the material can withstand based on the original area.

5. **Plasticity:** Plasticity is defined as the ability of certain metals to change the shape permanently when it is subjected to the load of intermediate magnitude between those producing elastic behavior and those causing a failure of the material. Theory of plasticity involves the mathematical description of material deformation mechanism in terms of loads, stress and strains. From the viewpoint of design, plasticity is concerned with predicting the safe limits for the use of a material under the maximum load without causing a material failure.

6. **Anisotropic:** Materials whose properties depend upon the direction. Example: metallic crystals.

Outline of the Thesis

- **Chapter 1:** In this chapter, we discuss the governing equations related to the concept of stress/strain at a point. Then, we carry out the analysis of stress/strain at a point to develop the ideas of stress/strain invariants, maximum shear stress, principal stress. We also discuss the concept of linear strain for small deformation. We show the relationship between stress-strain for small deformation of linearly elastic materials. However, these relations are not directly useful for analyzing material's behavior under large deformation (i.e. plastic behavior), their development gives a method of expressing qualitative material behavior into quantitative form and we use this knowledge to develop the stress-strain relationship for large deformation that will be needed in Chapter 3.

- **Chapter 2:** This chapter discusses the method of Molecular Dynamics (MD) that are required to carry out the atomistic simulations. With the introduction of various ensembles, the chapter focuses on the constant stress Hugoniostat (NPzzHug), quasi-isentropic compression and concept of shock wave. The chapter ends with the formalism of Embedded Atom Method (EAM) used to model atomic interaction.

- **Chapter 3:** This chapter introduce the concept of wave propagation in crystals. We derived the equation for acoustic wave propagation in cubic crystals. The wave propagation instabilities are analysed for two crystallographic directions namely (100) and (110). The concept of solid-solid phase transformation is introduced and the phase stability criterion is mentioned.

- **Chapter 4:** In this chapter, I show the results of MD simulation where FCC metallic single crystals is compressed quasi-isentropically. The result from shock simulations are compared. The role of directional dependency of plasticity in phase transformation is examined, and the the rate of plastic deformation and the BCC fraction growth rate are calculated.

Chapter 1

Linear Elasticity: Fundamental Concepts

1.1 The Strain

Let us consider a body with arbitrary shape as shown below in the Fig. 1.1. Now, a radius vector $\mathbf{X}$ (with component X_1, X_2 and X_3)defines the initial position of any point $\mathbf{P}$ in some coordinate system. Let us apply an external force that is exerted on the surface. Now point $\mathbf{P}$ moves to the point $\mathbf{p}$ with co-ordinate $\mathbf{x}$ (with component x_i) where

$$\mathbf{u} = \mathbf{x} - \mathbf{X} \tag{1.1}$$

is called the deformation vector and gives a measure of deformation due to the application of external force. or

$$u_i = x_i - X_i \tag{1.2}$$

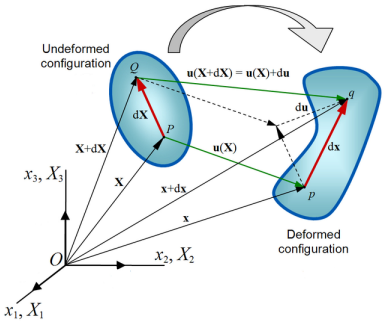

Figure 1.1: Deformation of a continuum body.

Since the co-ordinate x_i due to deformation is a function of the co-ordinates X_i of the initial point. Hence the displacement vector u_i is also a function of initial coordinates before displacement. If $\mathbf{u}$ is a function of X_i than we can determine the deformation of a body. Let us consider two points $\mathbf{P}$ and $\mathbf{Q}$ close to each other initially before the application of external force. After deformation of a body, the point change to $\mathbf{p}$ and $\mathbf{q}$. Let $\boldsymbol{dx}$ be the radius vector joining them, then radius vector is given as $dx_i = dX_i + du_i$. The distance

$$PQ = dX = \sqrt{dX_1^2 + dX_2^2 + dX_3^2} \tag{1.3}$$

and after deformation

$$pq = dx = \sqrt{{dx_1}^2 + {dx_2}^2 + {dx_3}^2} \tag{1.4}$$

In more condensed form we can write

$$dX^2 = \sum_i^3 dX_i^2 \tag{1.5}$$

$$dx^2 = \sum_i^3 {dx_i}^2 = \sum_i^3 (dX_i + du_i)^2 \tag{1.6}$$

But $du_i = (\frac{\partial u_i}{\partial X_k})dX_k$. Substituting this in the above equation,

$$dx^2 = dX^2 + 2\frac{\partial u_i}{\partial X_k}dX_i dX_k + \frac{\partial u_i}{\partial X_k}\frac{\partial u_i}{\partial X_l}dX_k dX_l \tag{1.7}$$

After taking summation over both suffixes i and k in the second term on the right, we can write

$$\frac{\partial u_i}{\partial X_k}dX_i dX_k = \frac{\partial u_k}{\partial X_i}dX_i dX_k \tag{1.8}$$

Now interchanging i and l in the last term of expression for dx^2, we obtain

$$dx^2 = dX^2 + 2u_{ik}dX_i dX_k \tag{1.9}$$

where the tensor u_{ik} is given by

$$u_{ik} = \frac{1}{2}(\frac{\partial u_i}{\partial X_k} + \frac{\partial u_k}{\partial X_i} + \frac{\partial u_l}{\partial X_i}\frac{\partial u_l}{\partial X_k}) \tag{1.10}$$

Equation (1.10) gives the strain tensor u_{ik} which is also called Green-Lagrangian strain tensor and, it gives the change in an element of the body after deformation. Since strain tensor is symmetrical (Lagrangian strain tensor is also represented by η_{ik}), we can write $u_{ik} = u_{ki}$ where

$$2\frac{\partial u_i}{\partial X_k}dX_i dX_k = (\frac{\partial u_i}{\partial X_k} + \frac{\partial u_k}{\partial X_i})dX_i dX_k \tag{1.11}$$

was used in the expression of dx^2. Since u_{ik} is symmetrical, we can diagonalized so that we get non-zero diagonal components u_{11}, u_{22}, and u_{33}. Let us denote each components as $u^{(1)}$,$u^{(2)}$ and $u^{(3)}$ respectively. For a diagonalized tensor at a given point, the dx^2 of equation (1.9) becomes

$$dx^2 = (\delta_{ik} + 2u_{ik})dX_i dX_k \tag{1.12}$$

$$= (1 + 2u^{(1)})dX_1^2 + (1 + 2u^{(2)})dX_2^2 + (1 + 2u^{(3)})dX_3^2 \tag{1.13}$$

This expression is the sum of three independent terms. It means the strain in any volume element may be regarded as composed of independent strains in 3 mutually perpendicular directions, namely those of the principal axes of the strain tensors. These strains represents a simple elongation or compression in their respective direction. For example, the length after deformation along X_1 axis becomes

$$dx_1 = \sqrt{(1 + 2u^{(1)})}dX_1, \tag{1.14}$$

and similarly

$$dx_2 = \sqrt{(1 + u^{(2)})}dX_2 \tag{1.15}$$

$$dx_3 = \sqrt{(1 + u^{(3)})}dX_3 \tag{1.16}$$

along dX_2 and dX_3 axis respectively. Therefore,

$$\sqrt{(1 + 2u^{(i)})} - 1 = \frac{dx_i - dX_i}{dX_i} \tag{1.17}$$

along the i^{th} principal axis where right hand side gives the relative extension(or compression) of the element. Also, in another form, the change in the squared lengths that occurs

as a body deforms from the reference to the current configuration can be expressed relative to x as

$$e_{ik} = \frac{1}{2}(\frac{\partial u_i}{\partial x_k} + \frac{\partial u_k}{\partial x_i} - \frac{\partial u_l}{\partial x_i}\frac{\partial u_l}{\partial x_k}) \tag{1.18}$$

where e_{ij} is called the Euler strain tensor. In most practical cases the strain is less than 1 as the original length before deformation is always greater than the deformed length. For a body subjected to small deformation, we can neglect the non-linear term in the definition of Green strain tensor. In such case, no distinction is made between the material coordinates X and the spatial coordinates x. Therefore, the linear Green strain tensor and the Euler strain tensor become same. If we denote infinitesimal strain tensor by ϵ, we can write

$$u_{ik} = e_{ik} = \epsilon_{ik} = \frac{1}{2}(\frac{\partial u_i}{\partial x_k} + \frac{\partial u_k}{\partial x_i}) \tag{1.19}$$

Thus, we can write

$$\frac{dx_i - dX_i}{dX_i} = \sqrt{(1 + u^{(i)})} - 1 \approx u^{(i)} \tag{1.20}$$

This means that the principal values of the strain tensors u_{ik} is nothing but the relative extension (compression) along the i^{th} principal axes. We can write strain tensor in the matrix form as follows:

$$\begin{pmatrix} u_{11} & u_{12} & u_{13} \\ u_{21} & u_{22} & u_{23} \\ u_{31} & u_{32} & u_{33} \end{pmatrix} = \begin{pmatrix} \partial u_1/\partial x_1 & \frac{1}{2}(\partial u_1/\partial x_2 + \partial u_2/\partial x_1) & \frac{1}{2}(\partial u_1/\partial x_3 + \partial u_3/\partial x_1) \\ \frac{1}{2}(\partial u_2/\partial x_1 + \partial u_1/\partial x_2) & \partial u_2/\partial x_2 & \frac{1}{2}(\partial u_1/\partial x_3 + \partial u_3/\partial x_1) \\ \frac{1}{2}(\partial u_3/\partial x_1 + \partial u_1/\partial x_3) & \frac{1}{2}(\partial u_3/\partial x_2 + \partial u_2/\partial x_3) & \partial u_3/\partial x_3 \end{pmatrix} \tag{1.21}$$

1.2 The Stress Tensor

For undeformed body, the atomic arrangements correspond to the thermal equilibrium. All parts of the body must be in mechanical equilibrium. This means, if we consider any specific part of the body, the net force on the that part would be zero. During deformation process, the atomic arrangement in the body changes and a body which was initially in the equilibrium state will no longer remains in the equilibrium state. During such case, a

body tend to return back to original state of equilibrium as the forces arise therein. These internal force occurred during deformation is called internal stresses. The inter-atomic forces are responsible for the occurrence of internal stresses. The point to be considered in the study of theory of elasticity is that the inter-atomic force has very short range of action. Hence, the impact of inter-atomic forces are only up to the neighborhood of atom exerting them, where an order of the distance is same as an inter-atomic distance. But in the macroscopic theory of elasticity, the distance under observation are larger than the inter-atomic distances. That is why the range of action of the inter-atomic force is considered to be zero. Therefore, the surrounding part exerts force on any other part is effective only on the surface. According to Newton's third law of motion and conservation of linear and angular momentum, when external contact forces act on a body, internal contact forces pass from point to point inside the body to balance their action. The density of internal forces at every point in a solid body is not necessarily even. It means there is a distribution of stress.

According to Cauchy stress principle[4], upon any surface that divides the body, the action of one part of the body on the other is equivalent (equipollent) to the system of distributed forces and couples on the surface dividing the body, and we can represent it by a vector field $\boldsymbol{t}_n$, called the stress vector, defined on the surface A and assumed to depend continuously on the surface's unit vector $\hat{\boldsymbol{n}}$. To define the stress vector (on a plane) at point P of the body, let us consider a plane passing through point P with a unit normal $\hat{\boldsymbol{n}}$. On both parts of body resulted due to plane, there are distributed internal forces acting on the cutting plane and exerted by the other half. In left half, consider small area around P. If $\triangle \boldsymbol{F}$ be a resultant force acting on a small area $\triangle A$ on the surface A around P exerted by the right half, then the stress vector at the point P on the surface is given as

$$\boldsymbol{t}_n = \lim_{\triangle A \longrightarrow 0} \frac{\triangle \boldsymbol{F}}{\triangle A}$$

The component of $\boldsymbol{t}_n$ normal to the plane is called as normal stress component, which is

denoted by σ_n. It is given as

$$\sigma_n = (\boldsymbol{t}_n)_i n_i \tag{1.22}$$

The component of $\boldsymbol{t}_n$ along the plane is called as the shear stress component. It is represented by τ.

The state of stress at point P is defined as the set: $\{\boldsymbol{t}_n \; \forall \; \boldsymbol{n}$ through $P\}$, which requires a knowledge of infinite number of $\boldsymbol{t}_n$'s. However, Cauchy theorem reduces this set to merely by knowing the stress vectors on three mutually perpendicular planes. The stress vector on any plane passing through that point can be found through coordinate transformation equation (proof is given in the Appendix B). We can pass an infinite number of planes through point P to obtain infinite number of stress vectors at that point. The set of stress vectors acting on each plane which pass through the point P describes the state of stress at point P. Since each point in the body is under static equilibrium, only nine stress components from three planes are needed to describe the state of stress at a point P. And these 9 components can form a matrix and represented as

$$\sigma_{ij} = \begin{pmatrix} \sigma_{11} & \sigma_{12} & \sigma_{13} \\ \sigma_{21} & \sigma_{22} & \sigma_{23} \\ \sigma_{31} & \sigma_{32} & \sigma_{33} \end{pmatrix} \tag{1.23}$$

The component σ_{ij} of the stress tensor represents the stress on a plane perpendicular to the x_i coordinate and in the x_j coordinate direction. The matrix elements corresponding to

$\sigma_{ij} = \delta_{ij}\{i = j$, is called normal stress

$i \neq j$, is called shear stress.

The Cauchy's relation is:

$$\begin{pmatrix} t_1 \\ t_2 \\ t_3 \end{pmatrix} = \begin{pmatrix} \sigma_{11} & \sigma_{12} & \sigma_{13} \\ \sigma_{21} & \sigma_{22} & \sigma_{23} \\ \sigma_{31} & \sigma_{32} & \sigma_{33} \end{pmatrix} \begin{pmatrix} n_1 \\ n_2 \\ n_3 \end{pmatrix} \tag{1.24}$$

The Cauchy's relation $(t_n)_i = {\sigma_{ij}}^T n_j$, suggests that if the matrix $[\sigma]$ is known, we can uniquely determine the stress vector $\mathbf{t}$ on any inclined plane. It means that the stress tensor

σ_{ij} fully characterises the state of stress at a given point. We show the perpendicular and parallel components of stress in the following Fig. 1.2

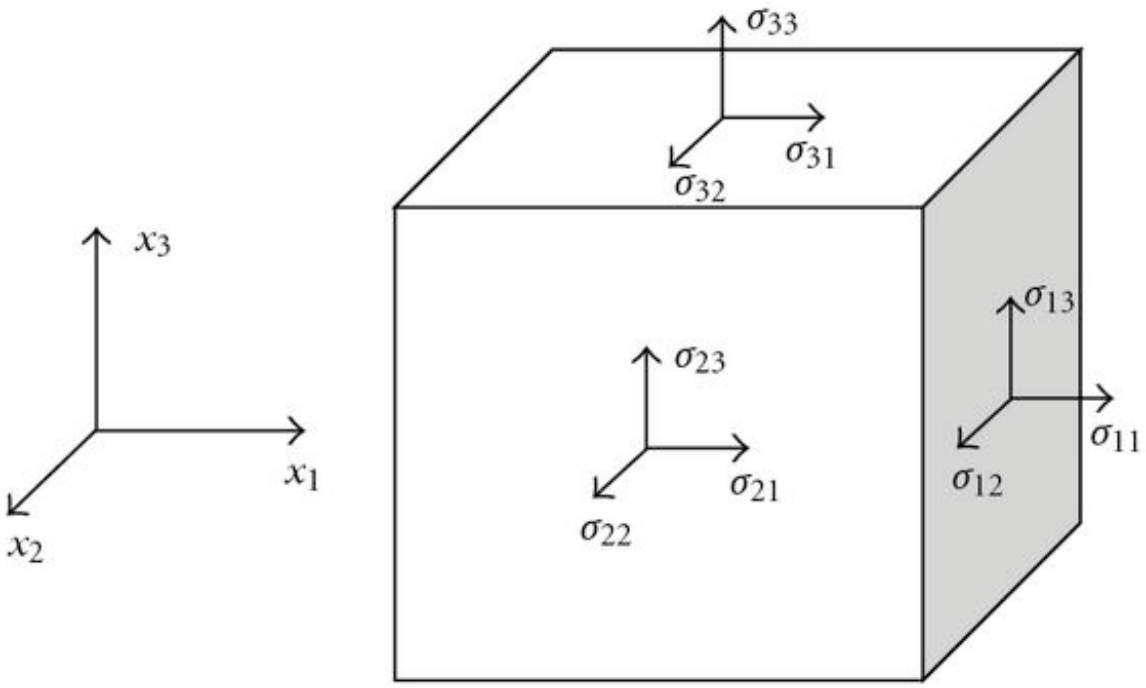

Figure 1.2: State of stress at a point of continuum.

For a given point, the principle stresses is the result of the combination of the maximum and the minimum values of the normal stresses within all planes. As we have mentioned earlier, the stress that arise due to the force vector component parallel to the material's cross section is called shear stress. It is denoted by τ where as a normal stress is denoted by σ is defined as the component of stress perpendicular to the material cross section at a point of action. For the normal stress σ and shear stress τ, the maximum shear stress can be calculated as follows:

$$(\tau)_{max} = \frac{1}{2}|(\sigma)_{max} - (\sigma)_{min}|, \tag{1.25}$$

$$(\sigma)_{max} \leq \sigma \leq (\sigma)_{min} \tag{1.26}$$

The two mutually perpendicular planes, on which this maximum shearing stress acts, bisect the planes of the largest and the smallest normal stress. In the case of uniaxial compression along the z-axis where the principal stress is directed along z-axis, the shear stresses are given by

$$\tau_{xz} = \frac{1}{2}|\sigma_{zz} - \sigma_{xx}| \tag{1.27}$$

$$\tau_{yz} = \frac{1}{2}|\sigma_{zz} - \sigma_{yy}| \tag{1.28}$$

And τ_{zz} is given by

$$\tau_{zz} = \frac{1}{2}(\tau_{xy} + \tau_{yz}) \tag{1.29}$$

1.3 Stress-strain relations for general anisotropic material

Let us apply an stress where the applied stress tensor is represented as σ_{ij}, such that the ith component of the force on a surface area $\boldsymbol{da}$. Now the force is given as

$$f_i = \sum_j \sigma_{ij} da_j \tag{1.30}$$

Now, the displace $\triangle X$ in the ith direction is given by

$$\triangle X_i = \sum_k u_{ik} X_k \tag{1.31}$$

Therefore, the work done by the crystal against the applied stress is given as

$$-\sum_i f_i \triangle X_i = -\sum_{ijk} \sigma_{ij} u_{ik} X_k da_j \tag{1.32}$$

The total work done by the crystal is just the integral over the surface $\boldsymbol{a}$

$$\triangle W = -\int_S \sum_{ijk} \sigma_{ij} \triangle u_{ik} X_k da_j \tag{1.33}$$

Now using Gauss theorem and changing surface integral to volume integral,

$$\triangle W = -\int_V \sum_{ij} \sigma_{ij} \triangle u_{ij} dV = -V(X) \sum_{ij} \sigma_{ij} \triangle u_{ij} \tag{1.34}$$

Since $\sigma_{ij} = \sigma_{ji}$, we can replace the displacement gradient by the Lagrangian strain $\triangle\eta_{ij}$.

$$dW = -V(X)\sum_{ij}\sigma_{ij}d\eta_{ij} \tag{1.35}$$

But from the First Law of Thermodynamics,

$$dU = TdS - dW \tag{1.36}$$

substituting the expression for work, we get

$$dU = TdS + V(X)\sum_{ij}\sigma_{ij}d\eta_{ij} \tag{1.37}$$

where the internal energy is path independent. For dU to be a total differential,

$$\sigma_{ij} = \frac{1}{V(X)}(\frac{\partial U}{\partial \eta_{ij}})_S \tag{1.38}$$

$$T = (\frac{\partial U}{\partial S})_\eta \tag{1.39}$$

To calculate the stress change with strain, lets consider two configurations, say $\boldsymbol{X}$ and $\bar{\boldsymbol{X}}$. Now, calculate $\sigma_{ij} - \bar{\sigma_{ij}}$. The description of the stress-strain relation at finite strain to the first order in the strain η_{ij} from X to $\bar{X}$ can be written as[5].

$$\sigma_{ij} = \sigma^0_{ij} + \sum_{kl}[-\sigma^0_{ij}\delta_{kl} + \sigma^0_{il}\delta_{jk} + \sigma^0_{jk}\delta_{il} + C^S_{ijkl}]\eta_{kl} \tag{1.40}$$

where the elastic stiffness coefficients are defined as

$$B_{ijkl} = -\sigma^0_{ij}\delta_{kl} + \sigma^0_{il}\delta_{jk} + \sigma^0_{jk}\delta_{il} + C^S_{ijkl} \tag{1.41}$$

where σ^0_{ij} is the component of the applied stress tensor. In the case of small deformation, the Lagrangian strain tensor η_{ij} reduce to the infinitesimal stress strain tensor ϵ_{ij} and if there is no initial applied stress, the stress-strain relation reduces to

$$\sigma_{ij} = C^S_{ijkl}\eta_{kl} = C^S_{ijkl}\epsilon_{kl} \tag{1.42}$$

where

$$C^S_{ijkl} = (\frac{\partial^2 U}{\partial \eta_{ij}\partial \eta_{kl}})_S \tag{1.43}$$

is called adiabatic elastic coefficients (superscript S is dropped here after for brevity). In the most general case, it would require 81 elastic constants to characterise a material fully. However, the symmetry of stress ($\sigma_{ij} = \sigma_{ji}$) and strain ($\epsilon_{ij} = \epsilon_{ji}$) reduces the number of independent elastic constants to 36. It is customary in mechanics of material to use a contracted notation (Voigt notation) for the stress, strain and stiffness tensors as follows: $11 \longrightarrow 1$, $22 \longrightarrow 2$, $33 \longrightarrow 3$, $23 \longrightarrow 4$, $13 \longrightarrow 5$, $12 \longrightarrow 6$, Stress-strain relation can be written in terms of stiffness C as:

$$\sigma_i = C_{ij}\epsilon_j \tag{1.44}$$

And in terms of Compliance S as:

$$\epsilon_i = S_{ij}\sigma_j \tag{1.45}$$

Since, strain and stress are second order tensor, therefore elastic constants C as well as compliance S are fourth order tensors. Here, the summation on repeated subscript is implied from 1 to 6. Since for the nature of C_{ij} depends on the symmetry of the crystal and for anisotropic material with $C_{ij} = C_{ji}$, the number of independent coefficients reduce to 21.

$$\begin{pmatrix} \sigma_1 \\ \sigma_2 \\ \sigma_3 \\ \sigma_4 \\ \sigma_5 \\ \sigma_6 \end{pmatrix} = \begin{pmatrix} C_{11} & C_{12} & C_{13} & C_{14} & C_{15} & C_{16} \\ C_{21} & C_{22} & C_{23} & C_{24} & C_{25} & C_{26} \\ C_{31} & C_{32} & C_{33} & C_{34} & C_{35} & C_{36} \\ C_{41} & C_{42} & C_{43} & C_{44} & C_{45} & C_{46} \\ C_{51} & C_{52} & C_{53} & C_{54} & C_{55} & C_{56} \\ C_{61} & C_{62} & C_{63} & C_{64} & C_{65} & C_{66} \end{pmatrix} \begin{pmatrix} \epsilon_1 \\ \epsilon_2 \\ \epsilon_3 \\ \epsilon_4 \\ \epsilon_5 \\ \epsilon_6 \end{pmatrix} \tag{1.46}$$

1.3.1 Application to cubic crystals

If one applies the symmetry elements of the cubic system, it turns out that the stiffness coefficients C_{ij} may be reduced to just three independent elastic constants: C_{11}, C_{12}, and C_{44}.

- $C_{11} = C_{22} = C_{33} \longrightarrow$ modulus for axial compression, i.e. a stress σ_{11} results in a strain ϵ_{11} along an axis;
- $C_{44} = C_{55} = C_{66} \longrightarrow$ shear modulus, i.e., a shear stress σ_{23} results in a shear strain ϵ_{23} across a face;
- $C_{12} = C_{13} = C_{23} \longrightarrow$ modulus for compression, i.e., an axial stress σ_{11} results in a strain ϵ_{22} along a perpendicular axis.

All other $C_{ij} = 0$. From these three, a useful combination can be written. For single crystals, the elastic constants can be related to common elastic moduli such as:

Shear modulus: $\mu = C_{44}$ and $C' = \frac{(C_{11}-C_{12})}{2}$

However, $\frac{(C_{11}-C_{12})}{2}$ turns out to be the stiffness associated with shear perpendicular to the $< 110 >$ direction. In certain case, this modulus can approach zero which corresponds to a structural instability. Zener proposed a measure of elastic anisotropy[6] based on the ratio $A = \frac{C_{44}}{C'} = \frac{2C_{44}}{C_{11}-C_{12}}$. This is a useful criterion for identifying materials that are elastically anisotropic.

Bulk modulus: $K = \frac{(C_{11}+2C_{12})}{3}$

Chapter 2

Molecular Dynamics Methods And Ensembles

Molecular dynamics (MD) is a computer simulation technique with which one predict time evolution of a system of interacting particles such as atoms, molecules, etc. The basic idea involved in MD simulation is that for a given system, we specify a set of initial conditions such as initial position and velocities of all the particles and we need an interaction potential for deriving the forces among all the particles. In this chapter, I will give a short overview of molecular dynamics method in the first half and conclude with the implication of MD specific to my research.

Recent development in experiments using high powered laser driven wave pulse gives us a different perspective of how a material can behave under the influence of high strain rates. We know that the high strain rates affect the mechanisms of deformation but some mechanism are too slow to respond on the time scale of an experiment. Thus, the study of material deformation at extreme conditions require the use of computer simulations so that trajectories can produce the average dynamic physical properties of interest. Atomistic MD simulations provide a way of visualizing and understanding the mechanism of plasticity, phase change and failure in solids at an extreme conditions in a detailed microscopic way, which otherwise would not be possible experimentally. Hence, MD simulation is ideal to study the plastic deformation at the high strain rates (otherwise the simulations would require too much time). However, irreversible heating is very severe in computer simulations involving high strain rates. Gigahertz to Tera-hertz strain rates are required if the induced stress are to overcome the natural thermal fluctuations present in small systems. Therefore,

the time scale required for a significant change in shape in MD simulation lies between nanoseconds $10^{-9}s$ to picoseconds ($10^{-12}s$).

2.1 Classical Lagrangian and Hamiltonian Dynamics

In classical regime, the time evolution of interacting particles and many-body systems are given as a variational re-statement of the Newton's second law of motion. For conservative systems, the Lagrangian is defined as follows:

$$L(\boldsymbol{q}, \dot{\boldsymbol{q}}) = K - V = \sum_{k}^{N} \frac{1}{2} m_k \dot{\boldsymbol{q}}_k^2 - V(\boldsymbol{q_1}, ..., \boldsymbol{q_N}) \tag{2.1}$$

Under the variational approach, we obtained the classical equations of motion and are given by Euler-Lagrange Equations:

$$\frac{d}{dt}(\frac{\partial L}{\partial \dot{\boldsymbol{q}}_k}) - \frac{\partial L}{\partial \boldsymbol{q}_k} = 0 \tag{2.2}$$

For a given initial condition, a solution of the equations of motion gives the trajectory of the system. It is clear that L is a function of the generalized coordinates q_k and their time derivatives $\dot{q}_k$, where N number of particles are interacting via a potential V. By using Lagrangian formulation via Euler-Lagrange equation, one can obtain the governing equation of motion of a system in any set of coordinates and not just the Cartesian coordinates. For a Cartesian coordinates system with a mass m for an atom i,

$$\frac{\partial L}{\partial \dot{\boldsymbol{r}}_i} = m_i \dot{\boldsymbol{r}}_i \tag{2.3}$$

$$\frac{\partial L}{\partial \boldsymbol{r}_i} = -\frac{\partial V}{\partial \boldsymbol{r}_i} = -\boldsymbol{\nabla}_{\boldsymbol{r_i}} V = \boldsymbol{F}_i \tag{2.4}$$

Therefore,

$$\frac{d}{dt}(\frac{\partial L}{\partial \dot{\boldsymbol{r}}_i}) - \frac{\partial L}{\partial \boldsymbol{r}_i} = m_i \ddot{\boldsymbol{r}}_i - \boldsymbol{F}_i \tag{2.5}$$

Hence, the Euler-Lagrange formulation is equivalent to Newton's second law. Lets define conjugate momenta as

$$\dot{\boldsymbol{p}}_i = \frac{\partial L}{\partial \dot{r}_i} \tag{2.6}$$

and Kinetic energy as

$$K = \sum_{i}^{N} \frac{\boldsymbol{p}_i{}^2}{2m_i} \tag{2.7}$$

For Hamiltonian dynamics, we define a functional of position and momentum which is independent of time for an isolated system. Hamiltonian gives the total energy of the system and is given as: $H(\boldsymbol{p}, \boldsymbol{r}) = \sum_i^N \frac{\boldsymbol{p_i}^2}{2m_i} + V(\boldsymbol{r_1}, ..., \boldsymbol{r_N})$. In terms of Lagrangian, we write Hamiltonian as follows:

$$H(\boldsymbol{p}, \boldsymbol{r}) = \sum_i \dot{r}_i p_i - L(\boldsymbol{r}, \dot{\boldsymbol{r}}) \tag{2.8}$$

where $\dot{\boldsymbol{r}}_i = \frac{\boldsymbol{p}_i}{m_i}$ The Hamilton's equations:

$$\dot{\boldsymbol{r}}_i = \frac{\partial H}{\partial \boldsymbol{p}_i} \tag{2.9}$$

$$\dot{\boldsymbol{p}}_i = -\frac{\partial H}{\partial \boldsymbol{r}_i} \tag{2.10}$$

gives the equation of motion for a given system. The solution of the Hamilton's equation is what gives a trajectory in terms of positions and momenta as a function of time. In the case of equilibrium, a dynamics or time-dependent behavior can be obtained, but in non-equilibrium but near equilibrium or far from equilibrium the detailed balance is prevented by constant flux.

2.2 Classical Molecular Dynamics and Force Computation

In MD, the Hamiltonian equations of motion are integrated in time based on an atomic interaction potential function (or force field) governing the behavior of the atoms and the forces on the particles are obtained. At instant t, if the initial position, velocity and other dynamic information are give then we can obtain the position, velocity and other dynamic information at later time $t + dt$ with enough accuracy by using suitable algorithm for

integration of the equation of motion (Verlet Algorithm). If $\boldsymbol{r}(t)$ represents a position at time t, then the the position at $t+dt$ (forward) and at $t-dt$ (backward) is given as follows:

$$\boldsymbol{r}(t+dt) = \boldsymbol{r}(t) + \delta t\boldsymbol{v}(t) + (\frac{1}{2})\delta t^2\boldsymbol{a}(t) + \frac{1}{3!}\delta t^3\boldsymbol{b}(t) + O(\delta t^4)... \tag{2.11}$$

$$\boldsymbol{r}(t-dt) = \boldsymbol{r}(t) - \delta t\boldsymbol{v}(t) + (\frac{1}{2})\delta t^2\boldsymbol{a}(t) - \frac{1}{3!}\delta t^3\boldsymbol{b}(t) + O(\delta t^4)... \tag{2.12}$$

Adding these two Taylor expansion, we obtain the equation for advancing the position and is given as

$$\boldsymbol{v}(t+dt) = 2\boldsymbol{r}(t) - \boldsymbol{r}(t-\delta t) + \delta t^2\boldsymbol{a}(t) + O(\delta t^4) \tag{2.13}$$

It is clear from the above expression that for evolving system in δt, the truncation's error of the algorithm is of the order of δt^4. Since there is a presence of $\boldsymbol{v}(t+\delta t)$ and $\boldsymbol{v}(t-\delta t)$, Verlet Algorithm is a time reversible in nature. For a given conservative force, this symmetry results in the conservation of momentum. Rearranging the basic form of Verlet algorithm, we get

$$\boldsymbol{a}(t) = \frac{\boldsymbol{v}(t+dt) - 2\boldsymbol{r}(t) + \boldsymbol{r}(t-\delta t)}{\delta t^2} \tag{2.14}$$

As we are integrating the Newton's equation of motion, $\boldsymbol{a}(t)$ is simply the force divided by mass where we have force as a function of position.

$$\boldsymbol{a}(t) = -\frac{1}{m}\nabla V(\boldsymbol{r}(t)) \tag{2.15}$$

The weakness of this Verlet algorithm is that the velocity of the system is not computed directly[7]. Even though one does not need to know the velocity to compute the system's evolution, however they are necessary in calculating the kinetic energy and hence in verifying the conservation of total energy (very important step to check whether the MD is proceeding correctly). Therefore, one could generate velocities from position by using

$$\boldsymbol{v}(t) = \frac{\boldsymbol{r}(t+\delta t) - \boldsymbol{r}(t-\delta t)}{2\delta t} \tag{2.16}$$

We can immediately see that the error related to this velocity computation is of the order of δt^2 rather than δt^4 (basic Verlet).To overcome such numerical imprecision, some variation

in the Verlet algorithm have been developed. One of such algorithm is leap-frog algorithm where velocity is handled in somewhat better manner but not the best[7]. Therefore, an equivalency of Varlet algorithm known as 'velocity Verlet' is developed, where positions, velocities,and accelerations at time $t + \delta t$ are obtained from the same quantities at time t as shown below:

$$\boldsymbol{v}(t + \delta t) = \boldsymbol{r}(t) + \boldsymbol{v}(t)\delta t + \frac{1}{2}\boldsymbol{a}(t)\delta t^2 \tag{2.17}$$

$$\boldsymbol{v}(t + \frac{\delta t}{2}) = \boldsymbol{v}(t) + \frac{1}{2}\boldsymbol{a}(t)\delta t \tag{2.18}$$

$$\boldsymbol{a}(t + \delta t) = -\frac{1}{m}\nabla V(\boldsymbol{r}(t + \delta t)) \tag{2.19}$$

$$\boldsymbol{v}(t + \delta t) = \boldsymbol{v}(t + \frac{\delta t}{2}) + \frac{1}{2}\boldsymbol{a}(t + \delta t)\delta t \tag{2.20}$$

Clearly, we need 9N memory storage to save the 3N, $\boldsymbol{v}$, $\boldsymbol{a}$, but we never have to have simultaneously stored the values at two different times for any of these quantities. This makes velocity Verlet algorithm, simple to program, numerically stable and convenient make it the most attractive algorithm[7]. Molecular Dynamics can be divided into two regions; one that deals with the system at equilibrium or near equilibrium and the one that deals with non-equilibrium phenomena which is far away from equilibrium. NPT or NVT or NPH simulations are only appropriate for equilibrium and are not for doing time dependent studies.

2.2.1 How macroscopic properties can be extracted from the Molecular Dynamics?

Statistical mechanics plays great role in connecting the computer generated microscopic information to the macroscopic information in terms of pressure, energy, etc. For an isolated system (constant energy E) with large number of particles, any fluctuations in a system

must fluctuate about a constant energy. And hence, any experimentally observable macroscopic property is given by the time average taken over a long finite time interval. However, statistical mechanics does not use this time average approach, it rather uses the concept of 'ensemble average'. And for a system, on the basis of ergodic hypothesis, the time averages is replaced by ensemble average[7]. The time evolution of coordinates in a phase space (position and momentum or ensemble average of particle trajectories) gives the information on the basis of statistical mechanics. For stationary ensemble which does not explicitly depend on time, the average value of any physical quantity (for isolated system, it is energy), will be independent of time. Clearly, such ensemble represents a system in equilibrium. For an isolated system with constant energy E, constant number of particles N restricted in a fixed volume V, these extensive variables (N,V and E) determines the thermodynamic state and termed as NVE or micro-canonical ensemble. Since MD simulation gives the time evolution of position and velocity at various test condition, one can look at the plastic deformation of a material by applying stress or strain on a lattice and observing the change in energy.

2.3 Ensembles

An ensemble is a collection of all microstates of a system, consistent with the constrains with which we characterize a system macroscopically. There are three ensembles which are commonly used: microcanonical (NVE) as mentioned above, canonical (constant NVT) where T is a constant temperature in absolute scale, and isothermal-isobaric (constant NPT) where P is a fixed pressure. For each ensembles, the mentioned extensive variables are kept fixed. In principle, by ensemble averaging, one can derived any other thermodynamical quantity. However, for the real world phenomena, such average deviates and hence the fluctuations occur. One can calculate various dynamic as well as structural and energetic properties from the average or the fluctuations of these quantities over the ensemble generated.

2.3.1 Microcanonical Ensemble

In a situation where no control over temperature and pressure is required, we can solve the Newton's equation to obtain NVE ensemble. As mentioned earlier, energy is conserved where a microcanonical ensemble is generated. Since, we can not get energy flow by controlling temperature in NVE, this limits in attending a desired temperature and hence not useful for equilibration of the real world system such as in our research where we are required to preset a constant value of T.

2.3.2 Canonical Ensemble

It is also known as NVT ensemble where number of particles, statistical temperature and total volume is kept constant. To carry out MD in the NVT ensemble, a modulation of temperature of a system is required and is done via thermostat. Therefore, requirement of NVT ensemble is that the particles must interact with a thermostat. The constant statistical temperature can be maintained either stochastically or dynamically (extended Lagrangian). However, one should not confused the purpose of introducing thermostat as to keep constant temperature (total kinetic energy), rather it should be taken as a way of obtaining the desired average temperature for a system. It is this extended Lagrangian in which we are interested to. One of the most widely used algorithms that can correctly reproduce the dynamics according to NPT or NVT ensemble is the Nosè-Hoover thermostat[8]. Under this approach, one need to couple the system temperature to heat bath via thermostat. Therefore, an extra degree of freedom is introduced to represent this thermal reservoir. The fluctuation in the Hamiltonian of the simulated or physical system occurs but the sum of the energy of the physical system along with heat reservoir is conserved. Therefore, the quantities that are conserved in the extended system are total Hamiltonian, total momentum and total angular momentum. Particles are allowed to exchange energy dynamically with a reservoir which has its own thermal inertial parameter. And for ergodic system, the stationary states give rise to canonical distribution. For a system under

consideration, to obtain extended system, extra terms to Newton's equation of motion is added. As we have discussed in details in a earlier section, Lagrangian for a conservative system is given by

$$L(\boldsymbol{q}, \dot{\boldsymbol{q}}) = K - V = \sum_{k}^{N} \frac{1}{2} m_k \dot{\boldsymbol{q}}_k^2 - V(\boldsymbol{q_1}, ..., \boldsymbol{q_N}) \tag{2.21}$$

And Newton's law is derived by substituting the above equation into the Euler-Lagrange equation (2.5). Now for the extended Lagrangian, all we need to do is to introduce new coordinate ζ which minimizes the difference between the statistical temperature and the instantaneous kinetic. This new coordinate which evolves in time is known as a frictional coefficient. Now, the modified equations of motion in Hoover formulation of Nose with frictional coefficients[8] looks like this:

$$\dot{v}_\alpha = \frac{F_\alpha}{m} - \nu_p \zeta v_\alpha \tag{2.22}$$

such that

$$\dot{\zeta} = \nu_T (\frac{T}{T_0} - 1) \tag{2.23}$$

By adjusting ζ, the simulation is allowed to reach an equilibrium state whose constant statistical temperature or desired temperature is T_0. Now, T_0 is considered as a parameter where as T as an instantaneous value fluctuates depending upon the thermal energy in the system at that instant. ν_p and ν_T are frequencies (also known as coupling-rate parameters). One can easily prove that the equations of motion derived above produce configurations in the canonical ensemble at externally set temperature T_0[8].

2.3.3 Isobaric-isothermal Ensemble

Isobaric-isothermal is also known as NPT ensemble and is very similar to the NVT ensemble with the exception of Pressure (P) being constant, rather than Volume (V). The equation of motion governing NPT ensemble are given as follows:

$$\dot{r}_\alpha = \nu_\alpha + \nu_p \eta_\alpha r_\alpha \tag{2.24}$$

$$\dot{v}_\alpha = \frac{F_\alpha}{m} - (\nu_p \eta_\alpha + \nu_T \zeta) v_\alpha \tag{2.25}$$

$$\dot{L}_\alpha = \nu_p \eta_\alpha L_\alpha \tag{2.26}$$

$$\dot{\zeta} = \nu_T (\frac{T}{T_0} - 1) \tag{2.27}$$

$$\dot{\eta_\alpha} = \frac{\nu_p}{B_0} (\sigma_{\alpha\alpha} - P_{\alpha\alpha}) \tag{2.28}$$

where the internal stress tensor $\sigma_{\alpha\beta}$ is given by

$$\sigma_{\alpha\beta} = \frac{[\sum m_i (v_{\alpha i} v_{\beta i}) + \sum r_{\beta i} F_{\alpha i}]}{V} \tag{2.29}$$

where η_α is a strain-rate variable that dynamically modifies the length of the computational box in the shock direction L_α

2.4 Non-equilibrium Molecular Dynamics (NEMD) Simulations

Shock waves are intrinsically a non-homogeneous, nonlinear phenomena. It is not possible to exactly reproduce the stress and density gradients present at the shock front, just by using an equilibrium molecular dynamics formulation. Therefore it was necessary to supplement the work done by the barostat with the right heat flow, controlled by the ergostat.

2.4.1 Shock Wave Equation of State

Whether impacting a target with high speed piston or detonating explosives, generates the shock wave that propagates through the material giving rise to compressed state of materials under study. For an steady shock velocity U with respect to the laboratory frame can be defined. We can write the following general relation governing the conservation of mass, conservation of momentum and conservation of energy across a shock front: These

conservation laws are known as the Rankine-Hugoniot conditions and are given below:

$$\rho_1 = \rho_0(U - u_0)/(U - u_1) \tag{2.30}$$

$$P_1 - P_0 = \rho_0(u_1 - u_0)(U - u_0) \tag{2.31}$$

$$E_1 - E_0 = (P_1 + P_0)(\frac{1}{\rho_0} - \frac{1}{\rho_1})/2 = \frac{1}{2}(u_1 - u_0)^2 \tag{2.32}$$

where ρ_0, u_0, P_0, E_0 are density, particle velocity, shock pressure and internal energy per unit mass respectively, for the shock front state whereas ρ_1, u_1, P_1, E_1 are for the state that is behind the shock front. Here, the term pressure is used for the one-dimensional stress normal to wave front. The internal energy per unit mass equation implies that the kinetic energy per unit mass is equal to the increase of internal energy per unit mass of the material under consideration. These three conservation equations are valid only when the shock wave is steady resulting the short relaxation time or rise time in comparison of characteristic time for which the high density, pressure etc. are constant.

In the simple case, when we observe single shock state through shock front, measurement of U, u_1, and ρ_0 in the Rankine-Hugoniot equations, lead us to determine shock state P_1, ρ_1,and $E_1 - E_0$. The final shock state in a material is obtained by passing a shock wave of pressure P_1. If we assume $u_0 = 0$, we can denote particle velocity as u_p and u_s as shock velocity. When the shock passed through material, initial values jumps to final values. The final states obtained for various shock strengths form the Hugoniot curve. Hugoniot curve can be plotted as a nearly straight line for u_s versus u_p, or as a non-linear plot of P_{zz} versus V. Such final shock state is shown in the PV plane (as in Figure 2.1) by using the following equations: For shock propagation along z-direction,

$$u_p = \sqrt{(P_1 - P_0)(V_0 - V_1)} = \sqrt{(P_{zz} - P_0)(V_0 - V)} \tag{2.33}$$

$$u_s = \sqrt{\frac{(P_1 - P_0)}{V_0 - V_1}}V_0 = \sqrt{\frac{(P_{zz} - P_0)}{V_0 - V}}V_0 \tag{2.34}$$

The curve describing the locus of final states defines the shock Hugoniot. A cusp in the Hugoniot as shown in the Fig. 2.1 occurs at an elastic-plastic transition (HEL) or at

structural phase transition and it can lead to split wave-structure. In the case of shock state, there are regions which can not be accessed. Therefore, a thermodynamic path known as Rayleigh line is used to go from one state to the final shock state.

It is useful empirical fact that for the most materials, the relation between u_s and u_p is linear. When Hugoniot crosses a phase line, however this relationship may no longer hold, and the $u_s - u_p$ plot may show a discontinuity. This happens because steady shock wave requires the sound speed that increases with compression. A first order phase transition violates this requirement, with the result that the wave breaks up into two parts[9]. The low pressure waves corresponds to the untransformed material, and the high-pressure waves corresponds to the transformed material. This two-wave region appears as a flat segment of constant u_s on the $u_s - u_p$ plot. When the shocked velocity in the transformed material rises above that of the untransformed material, a third segment appears on the $u_s - u_p$ plot. The appearance of discontinuities indicates the phase transition.

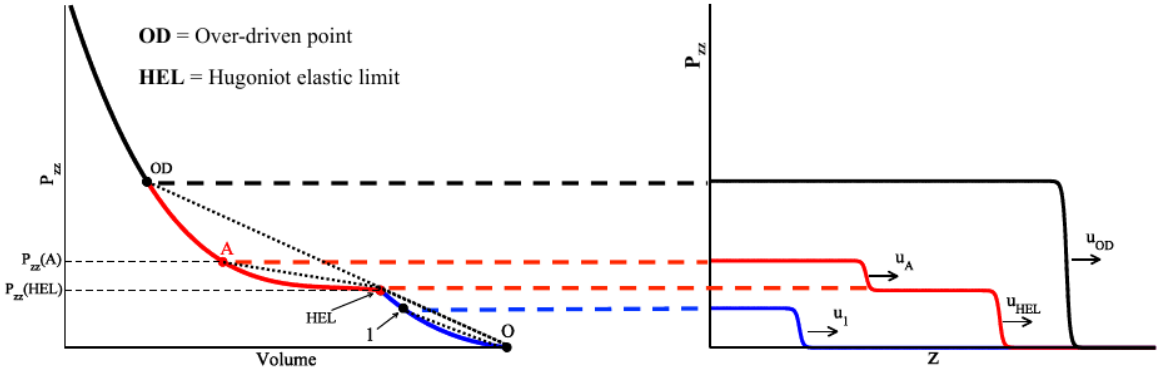

Figure 2.1: A generic Hugoniot.

2.5 Quasi-isentropic Compression

In the past, material properties under extraordinary strain rates were studied by the use of shock waves. However, shock loading results in the heating of the material simulta-

neously which is not suitable to obtain high pressure and high density state in experimental platforms. Therefore there exist an alternative approach known as quasi-isentropic compression-a shockless ramp compression in which non-steady-state waves are tailored to have a rapid rise but not as abrupt as a shock wave at the same pressure. Ideal isentropic loading is a state where the entropy remains constants and it is a shockless thermodynamics states. The entropy of a system is given as $dS = dQ/T$ where dS is the change in entropy, T is the absolute temperature and dQ is the amount of heat released or absorbed. However, in the real world it is not possible to obtain such ideal situation. Therefore, all the real world deformation phenomena are accompanied by the dissipation of heat due to plastic deformation. Hence, in the quasi-isentropic compression (approximately constant entropy) higher material compressions can be achieved resulting in lower temperatures that compressions produced via shock waves. In this case, the loading can be though as due to repeated smaller shocks or a smooth ramp. Therefore, quasi-isentropic simulations can be used to analyse the high pressure dynamical properties of materials at temperatures well below its melting point.

Quasi-isentropic molecular dynamics (MD) is different than Hugoniostat in a sense that the Hugoniostat describes the asymptotic state of the material behind the shock whereas quasi-isentropic MD loads the system along an isentrope and results in and increase of the internal energy by the work done on the system (no heat enters of exits the system during the compression). In order to simulate such a process, the MD equations of motion are modified to include a strain-rate variable as proposed by Ravelo et al[10]

$$\dot{r}_\alpha = v_\alpha + \dot{\epsilon_\alpha} r_\alpha \tag{2.35}$$

$$\dot{v_\alpha} = \frac{F_\alpha}{m} - \dot{\epsilon_\alpha} v_\alpha \tag{2.36}$$

$$\dot{L_\alpha} = \dot{\epsilon_\alpha} L_\alpha \tag{2.37}$$

where $\dot{\epsilon_\alpha}$ is a strain rate and is equal to $f(t,\tau)$; a time profile function with necessary conditions $f(t=0,\tau) = f(t,0)$. The following figures $(2.1-2.4)$ show a possible profile functions for the quasi-isentropic compression (constant strain-rate). We know that from the first law of thermodynamics, the rate of internal energy, heat and work done can be written as:

$$\dot{E} = \dot{Q} - \dot{W} = \sum_i m_i v_i \dot{v_i} + \sum_{i,j} \frac{\partial U}{\partial r}\dot{r} = \sum_i^N m_i v_i . \dot{v_i} - \sum_i^N F_i . \dot{r_i} \tag{2.38}$$

Since, v along α is given as

$$\dot{v}_\alpha = \frac{F_\alpha}{m} - \dot{\epsilon}_\alpha v_\alpha \tag{2.39}$$

The time rate of Energy is reduced to

$$\dot{E} = \sum_i^N m v_i (\frac{F}{m} - \dot{\epsilon} v_i) - F\dot{r}_i \tag{2.40}$$

$$= \sum_i^N [v_i F - m\dot{\epsilon} v_i v_i - F\dot{r}_i] \tag{2.41}$$

By substituting

$$v_i = \dot{r}_i - \dot{\epsilon_\alpha} r_i, \tag{2.42}$$

we get

$$\sum_i^N [(\dot{r}_i - \dot{\epsilon_\alpha} r_i)F_\alpha - m\dot{\epsilon} v_i v_i - F_\alpha \dot{r}_i] \tag{2.43}$$

Therefore,

$$\dot{E} = -\dot{\epsilon}_\alpha [\sum_i^N (r_i F_j + m_i (v_i)^2)] \tag{2.44}$$

But, stress tensor is given by $\sigma_{\alpha\beta} = \frac{1}{V}\sum_i^N [m_i(v_{\alpha i} v_{\beta i}) + r_{\beta i} F_{\alpha i}]$. Now, substituting this to the energy rate equation, we obtained:

$$\dot{E} = \dot{\epsilon_\alpha} V \sigma_{\alpha\alpha} = -\sigma_{\alpha\alpha}\dot{V} = -\dot{W} \tag{2.45}$$

The above equation clearly shows that $\dot{Q} = 0 \Rightarrow T\dot{S} = 0$. Hence entropy is constant. Now the energy difference between initial state at $E(t=0)$ and final state $E(t)$, gives

$$E(t) - E(0) = \triangle W = -\int_0^\tau \sigma_{\alpha\alpha}\dot{V} dt = -\int_0^\tau \dot{\epsilon}_\alpha \sigma_{\alpha\alpha} V dt \tag{2.46}$$

Therefore, $\triangle S = 0$ and no heat transfer is involved during the compression.

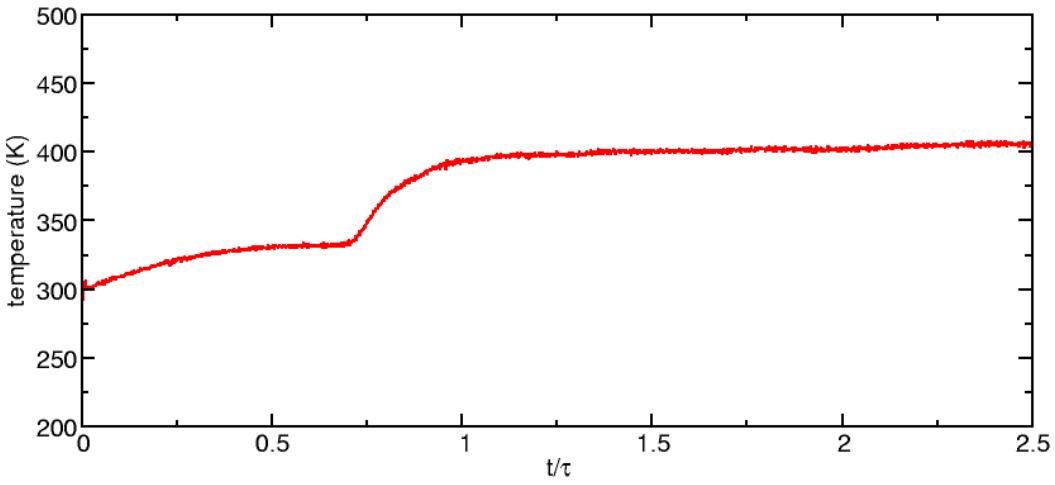

Figure 2.2: Time profile of temperature under uniaxial quasi-isentropic compression along (100) for ZM[11]model potential.

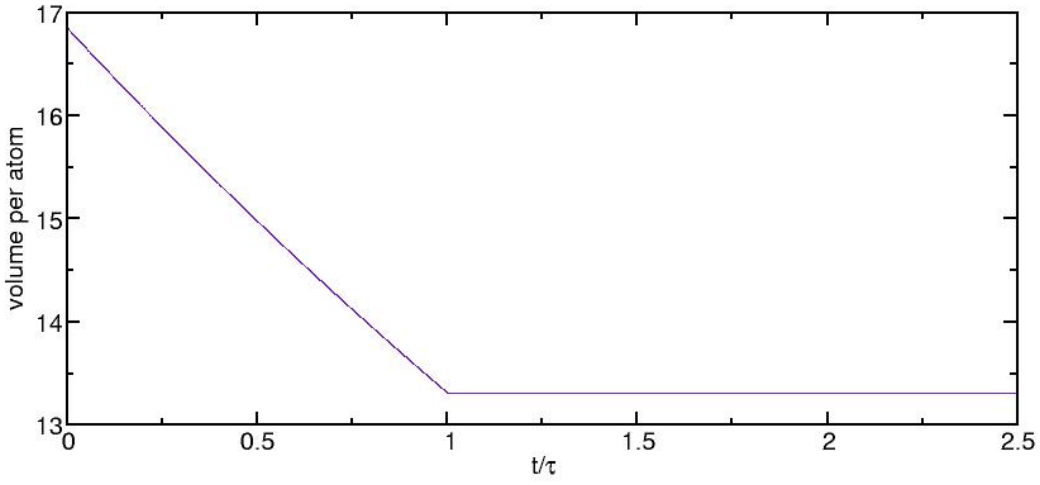

Figure 2.3: Time profile of volume per atom under uniaxial quasi-isentropic compression along (100) for ZM[11]model potential.

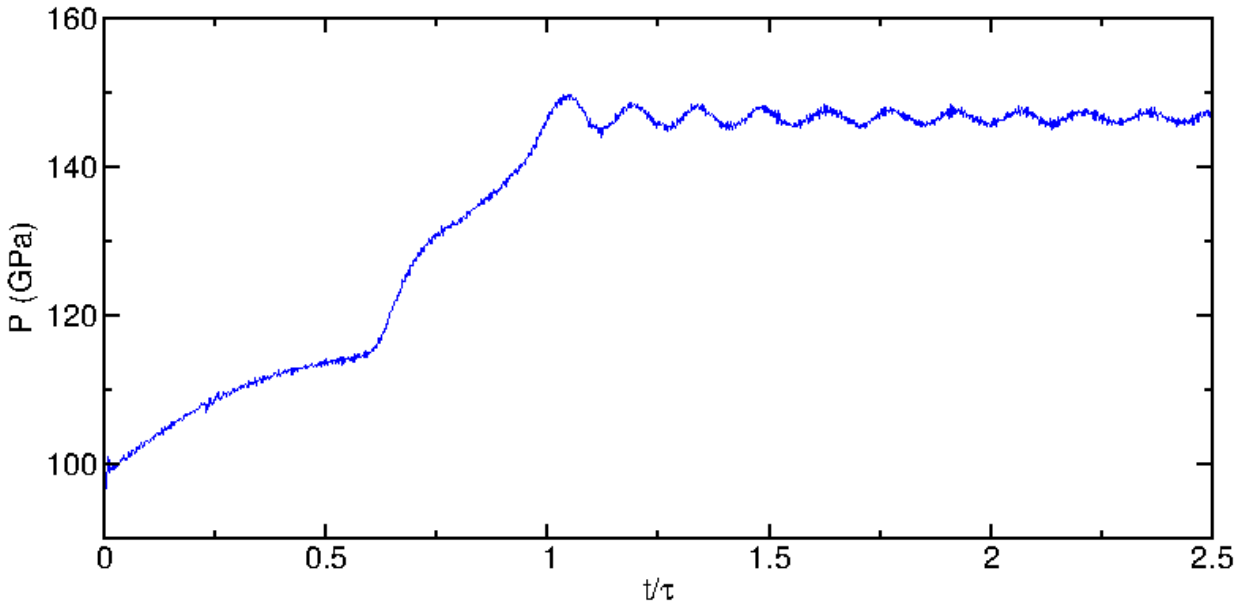

Figure 2.4: Time profile of pressure under uniaxial quasi-isentropic compression along (100) for ZM[11]model potential.

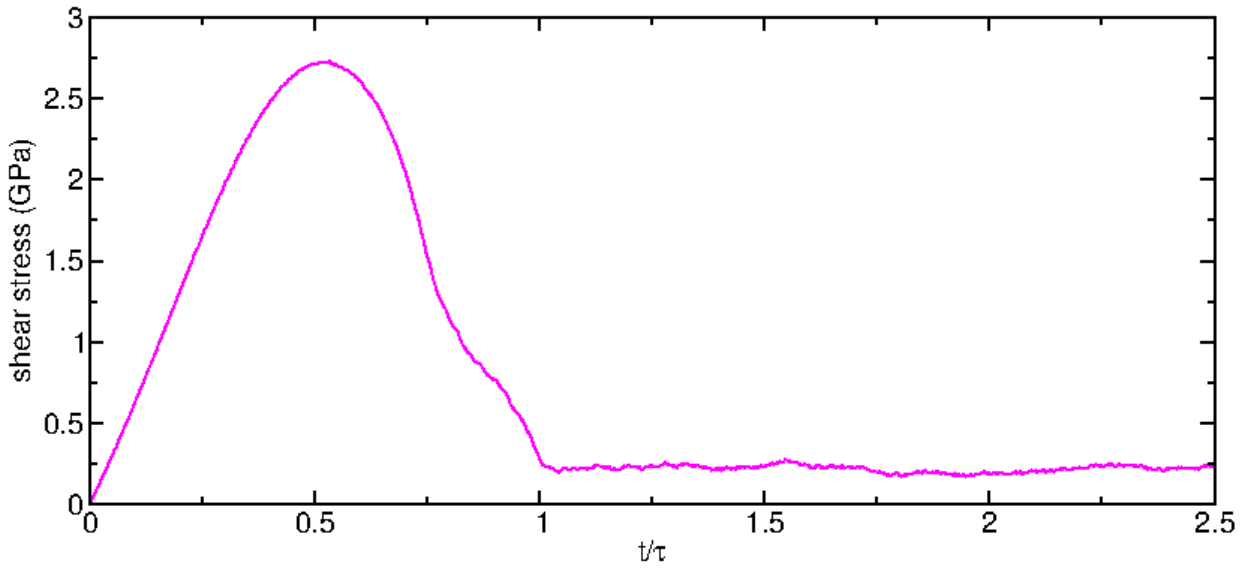

Figure 2.5: Time profile of shear stress under uniaxial quasi-isentropic compression.

2.5.1 Hugoniostat Simulation

Hugoniostat simulation is one of the important part of equilibrium MD tool, which is used to obtain the thermodynamic and structural properties of metallic single crystals under shock loading. Hugoniostat is different than Quasi-isentrope in a sense that the Hugoniostat describes the state in a material just behind the shock, whereas quasi-isentrope due to adiabatic compression is seen below the Hugoniostat. Hugoniostat simulation is based on Hugoniot relations[12] when a steady one dimensional (planar) shock passes through a material. The properties of the initial and final states are governed by the Hugoniot equation of mass, energy and momentum across the shock front. In our research, the equations (2.30), (2.31) and (2.32) are modified as follows:

Conservation of Mass:

$$\rho_0 u_s = \rho(u_s - u_p) \tag{2.47}$$

where, $u_s$is the shock velocity in the crystals produced by a piston moving into it at velocity u_p. $V = \frac{1}{\rho}$ is the volume per unit mass of the shocked material. From the equation of conservation of mass,

$$1 - \frac{\rho_0}{\rho} = 1 - \frac{V}{V_0} = \frac{u_p}{u_s} = \epsilon \tag{2.48}$$

gives compressive strain ϵ.

Conservation of Momentum:

$$P_{zz} = P_0 + \rho_0 u_s u_p \tag{2.49}$$

From this equation, one can determine the shock velocity u_s as follows:

$$u_s = \sqrt{\frac{P_{zz} - P_0}{\rho_0 \epsilon}} \tag{2.50}$$

and hence,

$$u_p = \sqrt{(P_{zz} - P_0)(V_0 - V)} = \epsilon u_s \tag{2.51}$$

Conservation of Energy:

$$E = E_0 + \frac{1}{2}(P_{zz} + P_0)(V_0 - V) \tag{2.52}$$

As mentioned in section 3.2, Pzz is the normal component of the pressure tensor in the direction of the shock wave. Given the thermodynamic parameters of the initial unshocked state, all the other parameters are determined provided either piston velocity or compression.

In the case of uniaxial Hugoniostat simulation, initial uniaxial compression $\epsilon = \frac{V}{V_0}$ is fixed and applied to the system. The dynamical evolution of the system is computed using

$$\frac{\boldsymbol{d}q_i}{dt} = \frac{\boldsymbol{p}_i}{m} = \dot{\boldsymbol{r}}_{\boldsymbol{i}} \tag{2.53}$$

$$\dot{\boldsymbol{p}}_{\boldsymbol{i}} = \boldsymbol{F}_i - \chi \boldsymbol{p}_i \tag{2.54}$$

where $\boldsymbol{r}_i$ and $\boldsymbol{p}_i$ are the particle co-ordinates and momenta respectively. For the total applied force $\boldsymbol{F}_i$, χ is an input parameter and chosen such that the derivative of the constrain is zero[12]. And,

$$\dot{\boldsymbol{\chi}} = \nu^2 \frac{E - E_0 - \frac{1}{2}(P_{zz} + P_0)(V_0 - V)}{N\epsilon_0} \tag{2.55}$$

where, ϵ_0 is the unit of energy for the interaction potential and frequency ν is linked with the heat-flow rate χ.

Shear stress plays important role in determining whether a material under shock is still solid or structural phase transformation has occurred or plastic deformation has occurred. Therefore, for materials to remain solid and show anisotropy, transverse motion (and hence P_{zz} greater than P_{xx}, and P_{yy}) must occur. For such solids, sufficient amount of shear stress is required so as to overcome the inherent energy barrier to produce defect.

Constant-stress Hugoniostat (NPzzHug)

Here we discuss a simple method for performing equilibrium MD simulations in the stress ensemble. In this research, we used the method proposed by Ravelo *et. al.*[13]. An extra degree of freedom is introduced through a dimensionless strain-rate variable η_α. The equation of motions augmented by barostat (piston) variables are given as follows:

$$\dot{r}_{\alpha i} = \frac{p_{\alpha i}}{m_i} + \nu_p \eta_\alpha r_{\alpha i} \tag{2.56}$$

$$\dot{p}_{\alpha i} = F_{\alpha i} - (\nu_p \eta_\alpha + \nu_H \zeta) p_{\alpha i} \tag{2.57}$$

$$\dot{L}_\alpha = \nu_p \eta_\alpha L_\alpha \tag{2.58}$$

$$\dot{\zeta} = \frac{\nu_H}{B_0 V_0}[E - E_H(t)] - \beta_H \zeta \tag{2.59}$$

This is a ergostat or heat flow equation.

$$\dot{\eta}_\alpha = \frac{\nu_p}{B_0}(\sigma_{\alpha\alpha} - P_{\alpha\alpha}) - \beta_p \eta_\alpha \tag{2.60}$$

This is a barostat or strain-rate equation. In the above equations, ν_H and ν_p are the coupling-rate parameters whereas β_H and β_p are damping coefficients.

$$\sigma_{\alpha\beta} = \sum (p_{\alpha i} p_{\beta i}/m_i + r_{\beta i} F_{\alpha i})/V \tag{2.61}$$

$$E_H(t) = E_0 + \frac{1}{2}[\sigma_{zz}(t) + P_0][V_0 - V(t)] \tag{2.62}$$

where the only strain rate variable η_z dynamically modifies the length of the simulation box in the direction of shock L_z. This is what regulates the instantaneous normal component stress tensor $\sigma_{zz}(t)$ to the preset value P_{zz}. Total internal energy of the system is given by: $E = K + \phi$ (sum of kinetic and potential energy). The dynamic evolution of the internal energy is given as: $\dot{E} = \dot{Q} - \dot{W}$ where,

$$\dot{E} = \sum_i^N [m_i v_i . \dot{v}_i - F_i . \dot{r}_i] \tag{2.63}$$

By using equation $(2.56 - 2.58)$, we can write the equation (2.3) to give strain-rate variables and heat-flow η_z and ζ:

$$\dot{E} = -3NK_B T \nu_H \zeta - \sigma_{zz} V \nu_p \eta_z \tag{2.64}$$

Now, since the change in internal energy is given by $\triangle E = E(t) - E(t=0) = \triangle Q - \triangle W$, one can write $\triangle Q$ and $\triangle W$ as follows:

$$\triangle Q = -3NK_B\nu_H \int_0^t dt'\zeta(t')T(t') \tag{2.65}$$

$$\triangle W = \nu_p \int_0^t dt'\eta_z(t')\sigma_{zz}(t')V(t') \tag{2.66}$$

This work done equals the work done by the piston and represents the area under the normal stress vs. volume[13].

Constant Volume Hugoniostat

In this case the temperature is controlled at a fixed volume to satisfy the Hugoniot energy. The equation of motions for Constant Volume Hugoniostat are given as follows:

$$\dot{p}_{\alpha i} = F_{\alpha i} - \nu_H \zeta p_{\alpha i} \tag{2.67}$$

$$\dot{\zeta} = \frac{\nu_H}{B_0 V_0}[E - E_H(t)] \tag{2.68}$$

$$E_H(t) = E_0 + \frac{1}{2}[P_{zz}(t) + P_0](V_0 - V) \tag{2.69}$$

where, ζ is a dimensionless heat flow variable; ν_H is heat-flow frequency (coupling rate) which provides the timescale for the heat flow and is constant. The ζ is used to relax the instantaneous internal energy E of the system to the Hugoniot energy $E_H(t)$. The relaxation of internal energy by regulating kinetic temperature of the system insures that the final temperature corresponds T to the desired temperature T_0 for the final volume V.

2.6 EAM Potential Functions

In order to use Molecular Dynamics method, we have to define the rules that are governing interaction of atoms in the system. In classical and semi-classical simulations, these rules are mostly expressed in terms of potential function. Construction of energy expression

assumes changes in the lattice energy can be written as a function of the position of the atoms in the material. Interaction energy in a system of N atoms can be expanded in 2-body, 3-body, ...terms:

$$E(1,2,...N) = \sum_i \phi_1(i) + \sum_{i,j} \phi_2(i,j) + \sum_{i,j,k} \phi_3(i,j,k) + ... + \sum_{i_1,i_2,...i_N} \phi_N(i_1,i_2,...i_N) \quad (2.70)$$

where ϕ_1 is one-body term, due to an external field or boundary conditions ϕ_2 is two-body term, or pair potential. The interaction of any pair of atoms depends only on their spacing and is not affected by the presence of other atoms. and ϕ_3 is three-body term arise when the interaction of a pair atoms is modified by the presence of a third atom. Based on the expansion, we can loosely separate potentials into two cases: pair potentials (only ϕ_2 is present) and many-body potentials (ϕ_3 and higher terms are included). The atomic interaction in metal is due to local electron density and can not be realistically described by considering only the pairwise-additive forces[14]. An alternative simple but rather realistic approach to the description of bonding in metallic system is based on the concept of local density that is considered as the key variable. To describe a metallic system, various many-atomic method have been developed based on different physical arguments (tight binding model, effective medium theory, etc.). However, all of these include many body effects and are as follows:

•Embedded Atom Method (EAM) (Daw & Baskes, Phys. Rev. Lett. 50, 1285 (1983))[15]

•Finnis Sinclair (Phil. Mag. A50, 45 (1984))[16]

•Glue Model (Ercolessi, Tosatti & Parrinello, Phys. Rev. Lett., 57, 719 (1986))[17]

Among these, EAM method is the most popular one and is widely used to Ercolessi-Adams (EA)[17], Angelo-Moody-Baskes (AMB)[18], Chantasiriwan and Milstein (CM)[19], Winey, Kubota and Gupta (WKG)[20], Mishin-Farkas (MF)[21], Mei and Davenport (MD)[22], Liu and Ercolessi and Adams (LEA)[23] model the potentials for metallic and alloys system.

2.6.1 Atomic Interaction Models: The Embedded Atom Method Formalism

Starting with the density functional theory (DFT), a typical potential consists of many functions combined in a complex way and usually nested to one into another and can be written as:

$$E_{coh} = F(\rho) + \frac{1}{2}\sum_{i,j}^{'} \frac{Z_i Z_j}{R_{ij}} - \sum_i \int \frac{Z_i \rho(r)}{|r - r_i|} + \frac{1}{2}\int\int \frac{\rho(r_1)\rho(r_2)}{r_{12}} dr_1 dr_2 - E_{atomic} \quad (2.71)$$

where E_{atomic} = energy of isolated atoms

Z_i and R_i = charge and positions of i^{th} nucleus

$F(\rho)$ = kinetic, exchange and correlation energy function

In formulating the above expression, following assumptions are made:

$$F(\rho) = \int f[\rho(r), \nabla\rho(r), \nabla^2\rho(r), ...dr] \quad (2.72)$$

And total electron density is the sum of densities of individual atoms where

$$\rho(r) = \sum_i \rho_i^a (r - R_i) \quad (2.73)$$

2.6.2 Embedded Atom Method Model Potential

As mentioned above, we use the embedded atom method (EAM). It is a semi-empirical, based on DFT where the total energy of any structural arrangement of nuclei (potential energy) is consider as a function of the positions of the atoms. Each atom is influenced by a locally uniform electron gas where total density for N ions in a arbitrary volume V with atomic mass m is given by $\rho = Nm/V$. The energy per atom E_i is summed to give total potential energy of the system.

$$E_{tot} = \sum_i E_i \quad (2.74)$$

The energy per atom E_i is given by

$$E_i = F(\rho_i) + \frac{1}{2}\sum_j \phi(r_{ij}) \tag{2.75}$$

where $\phi(r_{ij})$ is a pairwise potential (short-range) between atom i and neighbour atom j at a distance r_{ij} and is density-independent. $F(\rho_i)$ is the energy of embedding atom i into a homogeneous electron gas of density ρ_i. It is a non-linear function of local electron density for many-body interaction. Where embedding density ρ_i is given as

$$\rho_i = \sum_{j \neq i} f(r_{ij}) \tag{2.76}$$

where f is a spherically symmetric function. The EAM type potential which has functional form as in equation (2.72) and equation (2.73) are invariant under following transformations:

$$f(r) \rightarrow Af(r), \tag{2.77}$$

$$F(n) \rightarrow F(\frac{n}{A}) \tag{2.78}$$

$$\phi \rightarrow \phi + 2Cf(r) \tag{2.79}$$

$$F(n) \rightarrow F(n) - Cn \tag{2.80}$$

where A and C are arbitrary constants. For a pairwise-additive interaction, F is linear in electron density at site ρ_i but nonlinear dependency of embedding function in electron density give rise to the higher order many body contribution. Commonly used functional forms during fitting are:

$$F(\rho) = (E_c - \frac{1}{2}\sum \phi(r)), A\rho ln(\rho), ... \tag{2.81}$$

$$\rho(r) = (e^{-\gamma(\frac{r}{r_0}-1)}) \tag{2.82}$$

$\phi(r)$ = repulsive functions, $C(\frac{r_0}{r})^n$, Morse-type potentials, polynomials, splines, etc.

The elastic constants within the EAM framework can be calculated using the prescription outlined in ref[19]

Let $\boldsymbol{r}(= x_1\boldsymbol{i}+x_2\boldsymbol{j}+x_3\boldsymbol{k})$ and $\boldsymbol{r}_0$ are lattice vectors in the strained and unstrained crystals respectively, where x_i represents the Cartesian component of $\boldsymbol{r}$ in the ith direction. Now the magnitude of the difference of lattice vectors is give by

$$r^2 - r_0^2 = 2\sum_{I=1} X_I \eta_I, \tag{2.83}$$

where, $X_I = x_i x_j$ and I is the Voigt contraction of ij. Now, within the framework of EAM, second-order elastic moduli are calculated as follows:

$$\Omega_0 C_{IJ} = F''(\sum \frac{X_I f'}{r})(\sum \frac{X_J f'}{r}) + F' \sum \frac{X_I X_J}{r^2}(f'' - \frac{f'}{r}) + \frac{1}{2}\sum \frac{X_I X_J}{r^2}(\phi'' - \frac{\phi'}{r}) \tag{2.84}$$

where F' and f' are the derivatives w.r.t. ρ and r respectively. The detail derivation is given in the appendix A. For a crystal of cubic symmetry, the expression for the three independent second-order elastic moduli are written as:

$$\Omega_0 C_{11} = F''(\sum \frac{x_1^2 f'}{r})^2 + F' \sum \frac{x_1^4}{r^2}(f'' - \frac{f'}{r}) + \frac{1}{2}\sum \frac{x_1^4}{r^2}(\phi'' - \frac{\phi'}{r}) \tag{2.85}$$

$$\Omega_0 C_{12} = F''l(\sum \frac{x_1^2 f'}{r})^2 + F' \sum \frac{x_1^2 x_2^2}{r}(f'' - \frac{f'}{r}) + \frac{1}{2}\sum \frac{x_1^2 x_2^2}{r^2}(\phi'' - \frac{\phi'}{r}) \tag{2.86}$$

$$\Omega_0 C_{44} = F'' \sum \frac{x_1^2 x_2^2}{r^2}(f'' - \frac{f'}{r}) + \frac{1}{2}\sum \frac{x_1^2 x_2^2}{r^2}(\phi'' - \frac{\phi'}{r}) \tag{2.87}$$

The summation in the above equations are taken over atoms j around the reference atom i such that $i \neq j$.

2.7 Summary

In this chapter we reviewed the computational techniques that were used to perform the atomistic simulations as part of this work. We also provided a short introduction about the embedded atom method (EAM) formalism and which was used to describe the the atomic interactions. In the next chapter, we present theoretical background pertaining material deformation and determination of the elastic-plastic transition threshold in single crystals subjected to high strain rates of deformation.

Chapter 3

Plastic Deformation and Phase Stability in Metallic Single Crystals

To study the phase diagram, one must look at thermodynamics of first order phase transition. For two phases to be in thermodynamic equilibrium, they must have $T_1 = T_2$, $P_1 = P_2$, and $G_1 = G_2$, where they belong to temperature, pressure and Gibb's free energy of respective phase. According to Phase Rule, a single phase is represented by the area under $P-T$ curve, two phase mixture by the curve or phase line/boundary , and three-phase mixture is represented by a point (e.g. triple point). A one component phase diagram is a plot of areas representing phases, which are demarcated by phase boundaries in the P-T plane. Practical calculation of phase diagrams requires the location of all phase transitions over a given range of T and P. This is normally done by plotting isotherms of A vs. V or G vs. P for each possible phase. For the $G-P$ isotherms, the intersection of two curves locates the equilibrium pressure, and the slopes of the two curves at the intersection point are the equilibrium volumes.

Structural Solid-Solid Transitions

In order to evaluate the solid-solid phase transition boundary, we need to look at the free energies of the two phases in equilibrium. Calculation of small volume and corresponding energy changes across a typical solid-solid transition requires a high accuracy in the calculation of free-energy functions. In general, fcc crystal structure is the most stable structure.[9]

To determine the phase stability, we start from the first and second law of thermody-

namics. First law:

$$dQ = dU + dW, \tag{3.1}$$

Second law:

$$dQ = Tds \tag{3.2}$$

where, dW is the workdone by crystal and dQ is the amount of energy added to the crystal at absolute temperature T, U the internal energy, and S entropy of the crystal. We know that, for an isotropic pressure,

$$dW = PdV \tag{3.3}$$

We also know that, the Helmholtz free energy of the system is given as:

$$F = U - TS \tag{3.4}$$

From above three equations, we can also write as

$$\triangle W \geq \triangle U - T \triangle S = \triangle F \tag{3.5}$$

For a reversible transformation, the equality sign holds true. Let state A is in equilibrium configuration. We move it to nearby state B such that

$\triangle F - \triangle W > 0$. Therefore, for a system to be stable, W must be minimum. Hence, for an unstressed system, $\triangle W = 0$ for a system to be mechanically stable.

Let us consider a thermodynamics system at state A in equilibrium configuration. Now, thermodynamics variables are changed so as to move system out of equilibrium, then there should be a thermodynamic restoring force which tend to move system back to the equilibrium. Such system in initial equilibrium configuration which has the presence of restoring force is considered as a stable. Mathematically, at equilibrium $d^2S < 0$, i.e. the entropy is maximum, with respect to all virtual variation. Equivalently, $d^2U > 0$, internal energy is

minimum, w.r.t. all virtual variations. Thermodynamically stable phase is characterized by the lowest free energy phase in comparison to other phases. The equation for the change in Gibbs free energy $G(p, T)$ is given as:

$$G = U + pV - TS = H - TS \tag{3.6}$$

where, U is an internal energy, S is an entropy and H is the enthalpy of the system. When temperature T tends to $0K$ and system is at equilibrium volume, the phase with lowest G or lowest H will be the most stable phase thermodynamically for a given (p, T). Hence at zero temperature, the point at which the enthalpy difference is zero, determines the location of the phase transition boundary between two phases.

We examined many embedded atom method (EAM) model potentials of Aluminum assessing the stability of the face centered cubic (fcc) phase against other energetically close phases like body centered cubic (bcc) and hexagonal closed packed (hcp). Particularly we looked for models which would exhibit a simple phase diagram with a transition to bcc at higher pressures, determined on a first pass from the enthalpy difference at zero temperature. We chose to examined fcc $\rightarrow$ bcc structural transitions primarily because the nature of the plastic deformation in both of these crystal structures is different. Thus, two primary criteria was used in selecting interatomic potential models for this work:

- The model should incorporate a fcc $\rightarrow$ bcc transition at relative low pressures (close to the elastic-plastic threshold).
- The model should be able to reproduce correctly the plastic deformation of the fcc parent phase.

It should be pointed out that all Aluminum models we examined, undergo artificial structural transitions to either hcp or bcc between 20 and 30 GPa. Since pure Aluminum is experimentally known to remain in the fcc phase at pressures as high as 200 GPa[24], the EAM model chosen for this study should be taken as a model for instigating generic

features and characteristics of defect-mediated structural phase transitions, rather than a model for properly describing Aluminum at high pressures, which none of the sampled models do well, given than their undergo an artificial structural phase transformation to either bcc or hcp.

Table 3.1 summarizes the EAM models we investigated, indicating the transition pressure and corresponding phase the fcc phase is predicted to transform to, from a zero temperature enthalpy difference analysis.

Figure 3.1 shows the enthalpy difference between fcc-bcc and fcc-hcp as a function of pressure for the EAM model of Zope and Mishin[11] model, one of the EAM models listed in table 3.1. This is ultimately the model that was chosen for this study as it predicts an fcc $\rightarrow$ bcc structural transition around 28 GPa and as we will show in the next subsection, it is expected to reproduce plastic deformation in the fcc parent phase quite well compared to other models in table 3.1

Model	Phase Transition pressure (GPa)
EA[17]	20.7 (BCC)
AMB[18]	23.4 (HCP)
CM[19]	23.7 (BCC)
ZM[11]	27.7 (BCC)
WKG[20]	21.3 (HCP)
MD[22]	7.7 (HCP)
MF[21]	28.0 (BCC)
LEA[23]	2.5 (BCC)

Table 3.1: Phase Transition pressures in various EAM Models

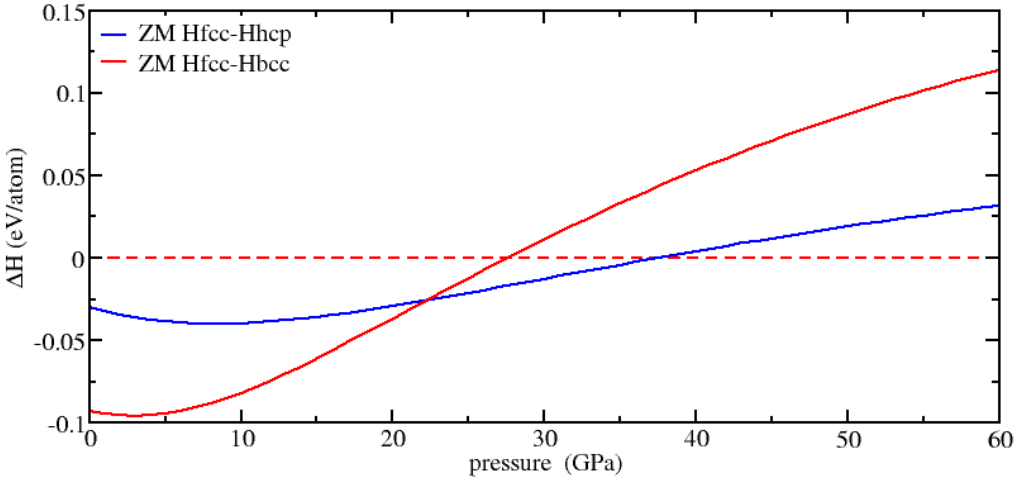

Figure 3.1: Enthalpy difference at T=0 K between the bcc/hcp and ideal fcc crystal phases for ZM model EAM potential[11]

3.1 Elastic-Plastic Transition

Almost all real materials will undergo some permanent deformation, which remains after removal of load. The maximum stress within a solid material that can arise before the onset of such permanent deformation is considered as an elastic limit of the material. Plasticity describes the deformation of a material undergoing non-reversible changes under the influence of applied forces. The classical theory of plasticity came out of the study of metals in the late nineteenth century. In the past, many scientists have studied the micro-structural aspect of plasticity. For example, in 1926 Frenkel made a simple calculation; in the case of metals to measure the shear stress required to initiate plastic deformation, critical resolved shear stress is required which results in sliding one plane along another. Taylor (1934), Orowan (1934) and Polanyi (1934) showed that the critical resolved shear stress is same for all slip system in a given crystal. In 1992, Rice showed that the energy must be greater than

maximum energy-displacement curve also known as the Gamma Surface for the occurrence of plasticity through dislocation nucleation. The intrinsic stacking fault energy, a measure of the energy penalty when two adjacent atomic planes in a crystal lattice are sheared relative to each other, is known to play an important role in the structure and energetics of dislocations formed by slip processes. The gamma surface of a fcc crystal is the energy per unit area needed to shear two (111) planes relative to one another along the $< 11\bar{2} >$ direction. The unstable stacking fault energy, corresponds to maximum value along the displacement direction while the stacking fault energy is the value at the maximum displacement of $d/\sqrt{3}$, where d is the nearest neighbor distance. The difference between the unstable and stable stacking fault energies, is directly related to the energy barrier that partial dislocations must overcome in order to widen the stacking fault and is an important parameter to reproduce the right type of plastic relaxation in fcc crystals.

Figure 3.2 shows the gamma surface of the various EAM models reference in table 3.1 as well as results from DFT calculations[25].

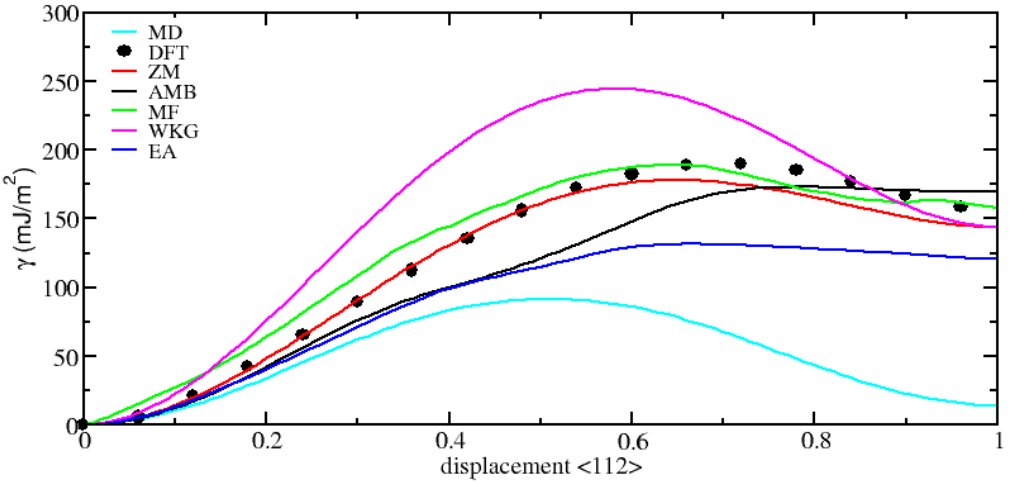

Figure 3.2: Comparision of cross-section of the gamma surface as a function of the displacement $d/\sqrt{3}$ for uniaxial tension, where d is the nearest neighbor distance, for ZM[11] model potential with other computed using the potentials of Ercolessi-Adams (EA)[17], Angelo-Moody-Baskes (AMB)[18],Chantasiriwan and Milstein (CM)[19], Winey, Kubota and Gupta (WKG)[20], Mishin-Farkas (MF)[21], Mei and Davenport (MD)[22], Liu, Ercolessi and Adams (LEA)[23] and DFT[25]

However, the mechanism of plastic deformation do not necessarily agree with these above cases and must be influenced by magnitude of strains. Metal plasticity problem falls under two broad groups. The first one involves relatively small plastic strains, often of the same order as the elastic strains which occur. The second type of problem involves very large strains and deformations, so large that the elastic strain can be disregarded[26]. When a material is subjected to large plastic deformations, the orientations and the grain sizes change in the direction of deformation.

Most metallic single crystals shows cubic symmetry that give rise to anisotropy in their physical properties such as elastics constants and wave propagation speed. The anisotropy leads to more complex wave propagation behavior as well as variation in deformations.

Process which are familiar at an ambient conditions such as plasticity and phase transformation no longer operate in equilibrium under extreme conditions. Any external agencies such as sock waves or quasi isentropic compression under extremely high load moves system far away from equilibrium and show a significant kinetic effects. Under such extreme condition, a key question to ask is whenever solids undergo phase transformations, what is the deformation modes that mediate it? Since the high strain rate affects material behavior both in kinetics of phase transformation and the mechanism of plastic deformation, we are interested to investigate the role of plasticity at the high strain rate regime. But, to understand the high strain rate effect, at first we must determine elastic limit and check the directional dependencies of yield strength at zero pressure.

In this chapter, we look at the condition at which plasticity occurs in the metallic single crystals at zero pressure, their dependence in the direction of wave propagation. In the second half, we give a quick overview of theory behind solid-solid phase transformation. And we conclude this chapter with the theoretical prediction that forms basis for our research.

3.2 Elastic Waves in Crystals

Elastic waves propagate in isotropic materials with equal velocity in every direction. Wave energy may propagate in longitudinal mode and shear mode. The faster mode in which the vibration of particles is parallel to the propagation of wave energy is refer as longitudinal mode. The slower mode in which the particle vibrations are perpendicular to propagation direction is termed as shear mode. The direction of the particle vibration is referred as the polarization.

The propagation of elastic waves in anisotropic media, i.e. in crystals, is more complicated than for the case of isotropic media. The most significant difference is that elastic waves propagate with a velocity that depends on direction. In contrast to isotropic case, three waves modes can propagate: one longitudinal and two transverse waves. However,

these modes are not necessarily pure modes as the particle vibration, or polarization is neither parallel nor perpendicular to the propagation direction. To investigate such waves, lets look at the general equation of motion.

3.2.1 Equation of Motion

The starting point to derive the equation for elastic wave velocity in an anisotropic solid is Hooke's law. For small strain, this law relates the stress σ acting on an elastic body to the strain ϵ. The stress tensor σ_{ik} describes stress acting on the ıth face in the kth direction of an elemental cube within the material. The elastic strain in a solid can also be described as a symmetrical tensor, ϵ_{ik}, and is related to the stress tensor through the elastic stiffness tensor C_{ikjl}. To be consistent with the following part of derivation, we use u_{jl} in place of ϵ_{jl}.

$$\sigma_{ik} = C_{ikjl} u_{jl} \tag{3.7}$$

The next step in computing equation of motion is by using Newton's second law of motion which says the acceleration at a point is not related to stress at that point (force per unit area), but to the spatial derivative of stress. By combining Hooke's law and Newton's second law of motion, we get

$$\rho \frac{\partial^2 u_i}{\partial t^2} = \frac{\partial \sigma_{ik}}{\partial x_k} \tag{3.8}$$

Here, ρ is the density of the cube and u_i is the displacement of a particle in the body in the ıth direction.

$$\rho \frac{\partial^2 u_i}{\partial t^2} = C_{ikjl} \frac{\partial u_{jl}}{\partial x_k} \tag{3.9}$$

Since,

$$\frac{\partial u_{jl}}{\partial x_k} = \frac{1}{2}\left(\frac{\partial^2 u_l}{\partial x_k \partial x_j} + \frac{\partial^2 u_j}{\partial x_k \partial x_l}\right) \tag{3.10}$$

Substituting the expression for $\frac{\partial u_{jl}}{\partial x_k}$, we get

$$\rho \frac{\partial^2 u_i}{\partial t^2} = C_{ikjl} \frac{\partial u_l}{\partial x_k \partial x_j} \tag{3.11}$$

Now, for a cubic crystal with displacement u_1 along x-direction, we get

$$\rho \frac{\partial^2 u_1}{\partial t^2} = C_{1111} \frac{\partial^2 u_1}{\partial {x_1}^2} + C_{1122} \frac{\partial^2 u_2}{\partial x_1 \partial x_2} + C_{1133} \frac{\partial^2 u_3}{\partial x_1 \partial x_3} + C_{1212} \frac{\partial^2 u_2}{\partial x_2 \partial x_1} + C_{1221} \frac{\partial^2 u_1}{\partial {x_2}^2} + C_{1313} \frac{\partial^2 u_3}{\partial x_3 \partial x_1} + C_{1331} \frac{\partial^2 u_1}{\partial {x_3}^2} \tag{3.12}$$

Here, the direction x_1, x_2, x_3 are parallel to the cube edges. And, u_1, u_2, u_3 are the components of the displacement vector of the deformation.

$$= C_{1111} \frac{\partial^2 u_1}{\partial {x_1}^2} + C_{1112} \left(\frac{\partial^2 u_2}{\partial x_1 \partial x_2} + \frac{\partial^2 u_3}{\partial x_1 \partial x_3} \right) + C_{1212} \left(\frac{\partial^2 u_2}{\partial x_2 \partial x_1} + \frac{\partial^2 u_1}{\partial {x_2}^2} + \frac{\partial^2 u_3}{\partial x_3 \partial x_1} + \frac{\partial^2 u_1}{\partial {x_3}^2} \right) \tag{3.13}$$

Therefore, by employing Voigt notation, we can re-arrange and re-write the above equation as

$$\rho \frac{\partial^2 u_1}{\partial t^2} = C_{11} \frac{\partial^2 u_1}{\partial {x_1}^2} + (C_{12} + C_{44}) \left(\frac{\partial^2 u_2}{\partial x_1 \partial x_2} + \frac{\partial^2 u_3}{\partial x_1 \partial x_3} \right) + C_{44} \left(\frac{\partial^2 u_1}{\partial {x_2}^2} + \frac{\partial^2 u_1}{\partial {x_3}^2} \right) \tag{3.14}$$

Similarly, for the x_2 and x_3 directions, we have the following equation of motion:

$$\rho \frac{\partial^2 u_2}{\partial t^2} = C_{11} \frac{\partial^2 u_2}{\partial {x_2}^2} + (C_{12} + C_{44}) \left(\frac{\partial^2 u_3}{\partial x_2 \partial x_3} + \frac{\partial^2 u_1}{\partial x_2 \partial x_1} \right) + C_{44} \left(\frac{\partial^2 u_2}{\partial {x_1}^2} + \frac{\partial^2 u_2}{\partial {x_3}^2} \right) \tag{3.15}$$

$$\rho \frac{\partial^2 u_3}{\partial t^2} = C_{11} \frac{\partial^2 u_3}{\partial {x_3}^2} + (C_{12} + C_{44}) \left(\frac{\partial^2 u_2}{\partial x_3 \partial x_2} + \frac{\partial^2 u_1}{\partial x_3 \partial x_1} \right) + C_{44} \left(\frac{\partial^2 u_3}{\partial {x_2}^2} + \frac{\partial^2 u_3}{\partial {x_1}^2} \right) \tag{3.16}$$

$$\rho \frac{\partial^2 u_i}{\partial t^2} = C_{ikjl} \frac{\partial^2 u_l}{\partial x_k \partial x_j} \tag{3.17}$$

One must note that the equation (3.11) is the special case when the applied stress is zero. For any initially stressed linearly elastic body, the elastic stiffness coefficients govern

the proper stress-strain relations at finite strains. The elastic coefficients C_{ikjl} must be therefore replaced by B_{ikjl}.

For small amplitude waves, the linearized equations of motion are obtained by evaluating the above expression for B_{ikjl} in a homogeneous initially stressed body. The elastic coefficient are given by[27]

$$B_{ikjl} = \sigma^0{}_{kl}\delta_{ij} + C_{ikjl} \tag{3.18}$$

Now, introducing the wave propagation coefficients B_{ikjl}, the equation (3.11) reduced to

$$\rho\frac{\partial^2 u_i}{\partial t^2} = B_{ikjl}\frac{\partial^2 u_l}{\partial x_k \partial x_j} \tag{3.19}$$

And, substituting the expression of B_{ikjl} in the above equation, we obtained

$$\rho\frac{\partial^2 u_i}{\partial t^2} = \sum_{kjl}(\sigma^0_{kl}\delta_{ij} + C_{ikjl})(\frac{\partial^2 u_l}{\partial x_k \partial x_j}) \tag{3.20}$$

For a wave propagation that is limited to single direction, the disturbance at a given instant will be the same at all points in a plane normal to the direction of wave propagation and it is termed as a plane wave. For the differential equation as given above, solution obtained are the plane waves. We look for solutions, u_i of the following form, in terms of $\boldsymbol{u}$ the displacement amplitude vector (which defines polarization), displacement in a plane wave of frequency ω and wave vector $\hat{\boldsymbol{k}} = \frac{\boldsymbol{k}}{|k|}$ is given as

$$u_i = u_{0i}e^{i(\boldsymbol{k}.\boldsymbol{r}-\omega t)} \tag{3.21}$$

Now, partially differentiating equation (3.15) twice and substituting it into the equation (3.15), and using the relation $v = \frac{\omega}{|k|}$, where v is the wave speed, we get

$$\rho v^2 u_{0i} = (\sigma^0_{kl}\delta_{ij} + C_{ikjl})\hat{k_k}\hat{k_j}u_{0l} \tag{3.22}$$

The equation 3.16 represents the eigenvalue problem, where the phase velocities v are the eigenvalues, and the u_{0l} vectors (polarization vectors) are eigenvectors.

There are three normal modes of wave motion in a crystal for a given magnitude and direction of the wavevector $\boldsymbol{k}$. In general, the polarizations of these modes are not exactly parallel or perpendicular to $\boldsymbol{k}$. In the special propagation directions [100], [110] and [111] of a cubic crystal, two of the three modes for a given $\boldsymbol{k}$ are such that the particle motion is exactly transverse to $\boldsymbol{k}$ and in the third mode the motion is exactly longitudinal (parallel to $\boldsymbol{k}$). Now we look for a simple special solutions in a given direction $\boldsymbol{k}$. As an example, lets look at the wave propagation along [100] direction in a crystal at zero pressure.

3.2.2 Waves in the [100] Direction

Let $\boldsymbol{k} = k(1, 0, 0)$ be the direction of propagation of waves along x-direction, then the solution for a differential equation is given by a longitudinal wave

$$u_1 = u_{01} e^{i(kx_1 - \omega t)} \tag{3.23}$$

where, u_1 is the x-component of the particle displacement. Both the wavevector and the particle motion are along the x-cube edge. Here $k = \frac{2\pi}{\lambda}$ is the wavevector and $\omega = 2\pi\nu$ is the angular frequency. Now substituting (3.15) into (3.5), we get

$$\omega^2 \rho = C_{11} k^2; \tag{3.24}$$

thus the velocity $\frac{\omega}{k}$ of a longitudinal wave in the [100] direction is

$$v_s = \nu\lambda = \frac{\omega}{k} = (\frac{C_{11}}{\rho})^2 \tag{3.25}$$

Now, consider a transverse or shear wave with the wavevector along the x_1 cube edge and with the particle displacement u_2 in the x_2 direction:

$$u_2 = u_{02} e^{i(kx_1 - \omega t)} \tag{3.26}$$

On substitution in (3.9) this gives the dispersion relation

$$\omega^2 \rho = C_{44} k^2 \tag{3.27}$$

Thus, the velocity $\frac{\omega}{k}$ of a transverse wave in the [100] direction is

$$v_s = \sqrt{\frac{C_{44}}{\rho}} \tag{3.28}$$

The same velocity is obtained if the particle displacement is in the x_3 direction. Hence, for $\boldsymbol{k}$ parallel to [100] the two independent shear waves are degenerate and have an identical velocities. This is not true for $\boldsymbol{k}$ in a general crystallographic direction.

Similarly, we can show that for waves in [110] direction, the longitudinal velocity can be shown as:

$$v = \sqrt{\frac{C_{11} + C_{12} + 2C_{44}}{2\rho}} \tag{3.29}$$

And for waves in [111] direction, the longitudinal velocity is given as:

$$v = \sqrt{\frac{C_{11} + 2C_{12} + 4C_{44}}{3\rho}} \tag{3.30}$$

The velocity of propagation of the wave (the group velocity) is given by the derivative of the frequency w.r.t. the wave vector. In an isotropic body, the frequency is proportional to the magnitude of $\boldsymbol{k}$, and so the direction of the velocity is the same as that of $\frac{\partial \omega}{\partial \boldsymbol{k}}$. In the crystal this relation doesn't hold true, and the direction of propagation of the wave is therefore not the same as that of its wave vector. Since, there are three possible relations between ω and $\boldsymbol{k}$ for any direction in the crystal, there are in general three different velocities of propagation of elastic waves. These velocities are the same only in a few exceptional directions.

In the crystal, to each velocity of propagation there corresponds a wave in which the displacement vector has components both parallel and perpendicular to the direction of propagation.

Hence, for a given direction in a solid, three-small amplitude plane waves with mutually perpendicular polarizations can propagate. Waves with polarization vectors parallel or

perpendicular to the propagation direction are denoted as longitudinal or transverse (shear) wave respectively. In general, a wave is neither purely longitudinal nor transverse. Two special types of directions are commonly of interest in wave propagation experiments: (1) pure mode direction with one pure longitudinal wave and two pure transverse waves. (2) quasi-pure mode directions, which have one pure transverse wave and two mixed waves. Symmetry direction of a crystal are always pure mode directions.

3.3 Wave propagation instabilities

An important concept to introduce at this stage is the wave propagation instability. An instability curve is a plot of the velocity (units are therefore km/s or equivalent) as a function of strain. Typically, an instability curve is produced by choosing a plane in the material of interest, and then calculating the longitudinal velocity for a selection of propagation directions. Velocity is then plotted as a function of strain.

When $|v_s| = 0$, equation (3.16) reduced to

$$|v_s|^2 = 0 \rightarrow \sum_{kl} (\sigma^0_{kl}(\epsilon, T)\delta_{ij} + C_{ikjl}(\epsilon, T))\hat{k_k}\hat{k_l} = 0 \tag{3.31}$$

the wave propagation instability occurs and the acoustic wave velocity as a function of the strain will be 0. One must note this point, since it is of great importance in determining the elastic-plastic transition in monoatomic crystals. Here, the notation $\sigma_{kl}(\epsilon)$ and $C_{ikjl}(\epsilon)$ is used to show the elastic constants and the stress are dependent of strain. The elastic constant as a function of strain $\sigma_{ik}(\epsilon)$ under uniaxial compression reflects symmetry dependence. Such symmetry dependence helps to reduce the terms on the solution of the sound speed propagation given by last equation. For an uniaxial compression along the low-index directions (100), (110) and (111), we found that the elastic constants as function of strain acquired following symmetries:

•FCC compressed along (100) ⇒ Face Centred Tetragonal (FCT)

•FCC compressed along (110) ⇒ Body Centred Tetragonal (BCT)

•FCC compressed along (111) ⇒ Rhombohedral

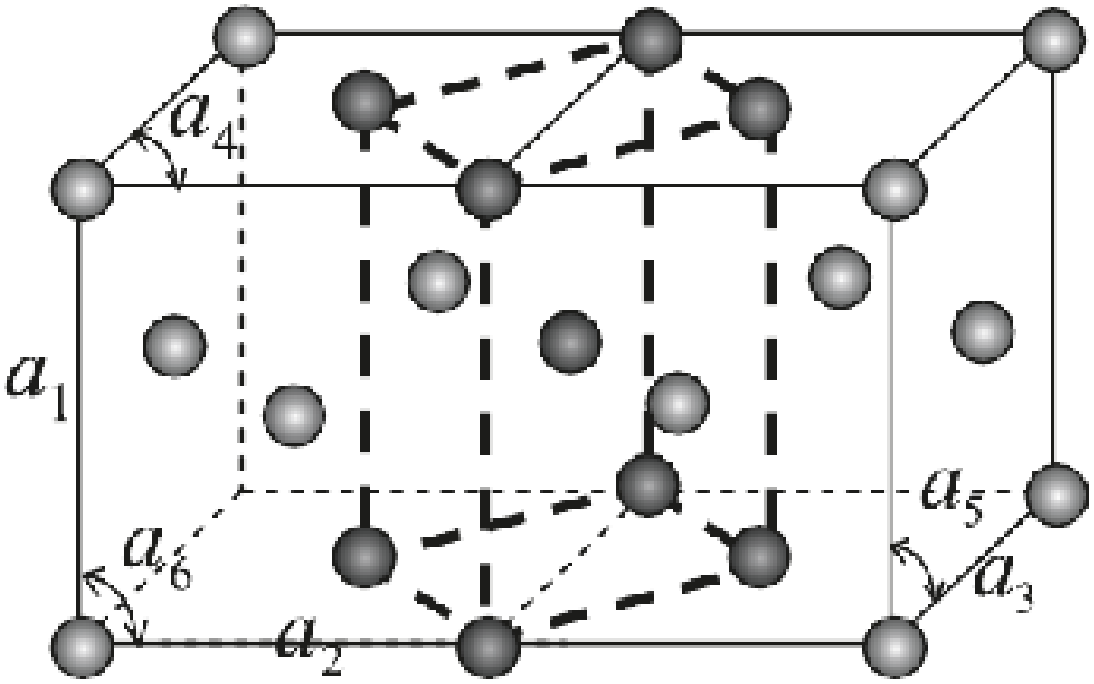

Figure 3.3: Two unit cells of a FCC crystal.

As an example, the above figure shows that two unit cells of a FCC crystal is subjected to a uniaxial stress parallel to edge a_1 and perpendicular to other two edges a_2 and a_3. Hence, edges a_1, a_2 and a_3 will remain mutually perpendicular throughout the loading path; i.e. at least until failure occurs and the angles between edges as represented by a_4, a_5 and a_6 will reconfigure to their initial value of $\frac{\pi}{2}$. Also, no shear stress acts on the faces of the cell. The starting state is the FCC cubic lattice with lattice parameter a_0. Under compressive load along $< 100 >$ direction, the cubic symmetry of initial state is broken. The metal adopts face centred tetragonal (FCT) lattice with tetragonal axis parallel to the direction of applied compression. Such deformation path is called primary tetragonal path. In the following subsection we show the instability in a metallic single crystals compressed unaxially along (100), (110) and (111) direction.

3.3.1 Elastic-plastic transition for compression along (100)

At the point where instability occurs (a point where wave velocity as a function of strain is zero), P is constant after elastic-plastic transition as $Pzz = P$ and, the pressure is isotropic. The following table shows how much do we need to compress crystal uniaxially to reach elastic-plastic transition. It also includes the strain required for a material to go under phase transformation.

Table 3.2: Determination of strain, stress tensor along z-direction and pressure for elastic plastic transition and phase transformation

$Direction(100)$	ϵ	$P_{zz}(GPa)$	$Pressure(GPa)$
Elastic-plastic	0.14	18.48	14.61
FCC$\longrightarrow$ BCC	0.24	25.88	27.67

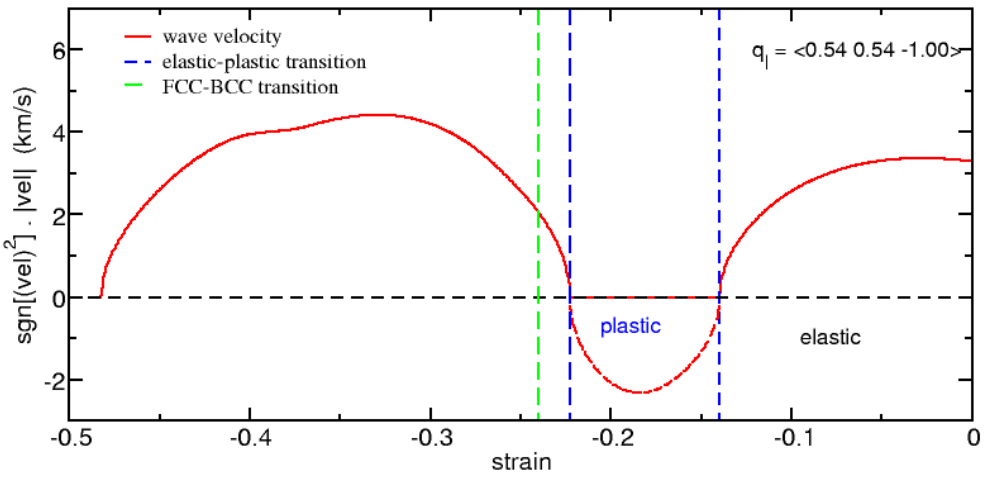

Figure 3.4: Sound velocity as a function of strain in a perfect crystal Al using ZM potential along (100) direction.

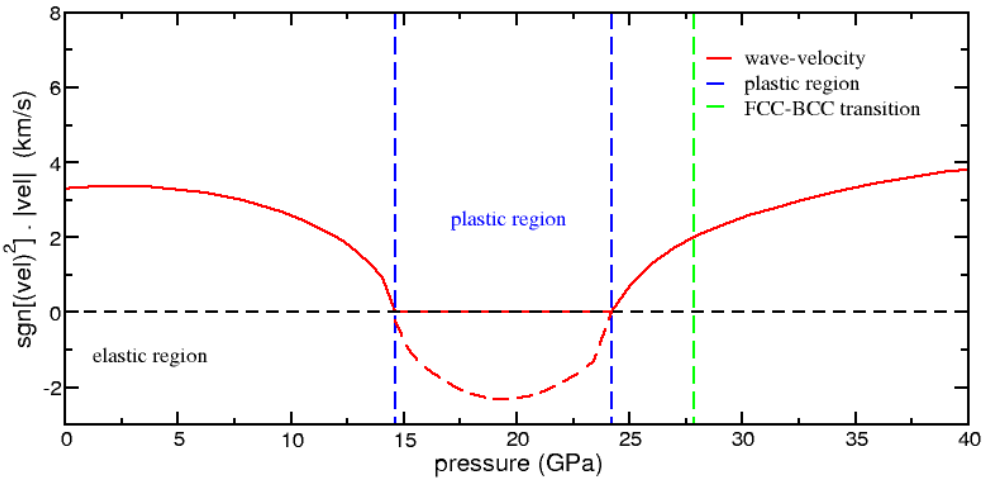

Figure 3.5: Sound velocity as a function of pressure in a perfect crystal Al using ZM potential along (100) direction.

3.3.2 Elastic-Plastic Transition for Compression along (110)

Table 3.3: Determination of strain, stress tensor along z-direction and pressure for elastic plastic transition and phase transformation

$Direction(110)$	ϵ	$P_{zz}(GPa)$	$Pressure(GPa)$
Elastic-plastic	0.1598	34.64	20.82
FCC$\longrightarrow$ BCC	0.195	47.68	27.67

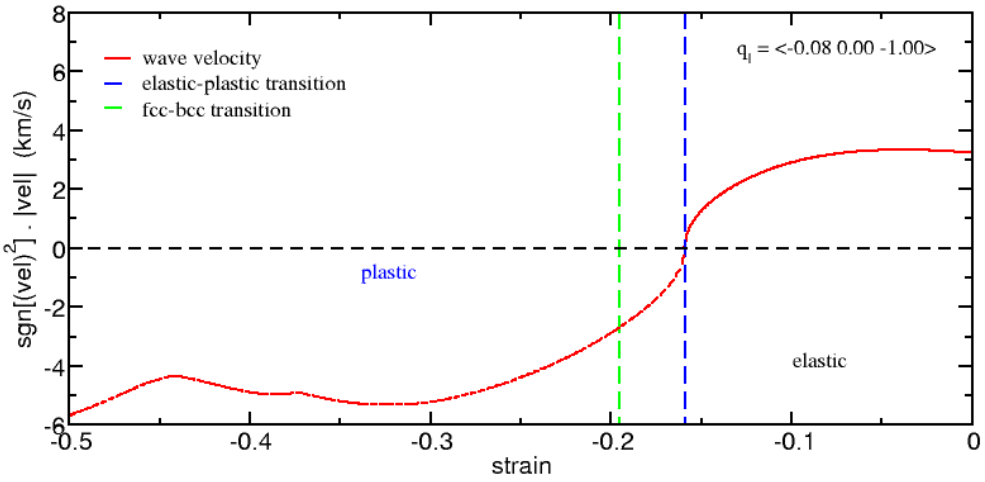

Figure 3.6: Sound velocity as a function of strain in a perfect crystal Al using ZM potential along (110) direction.

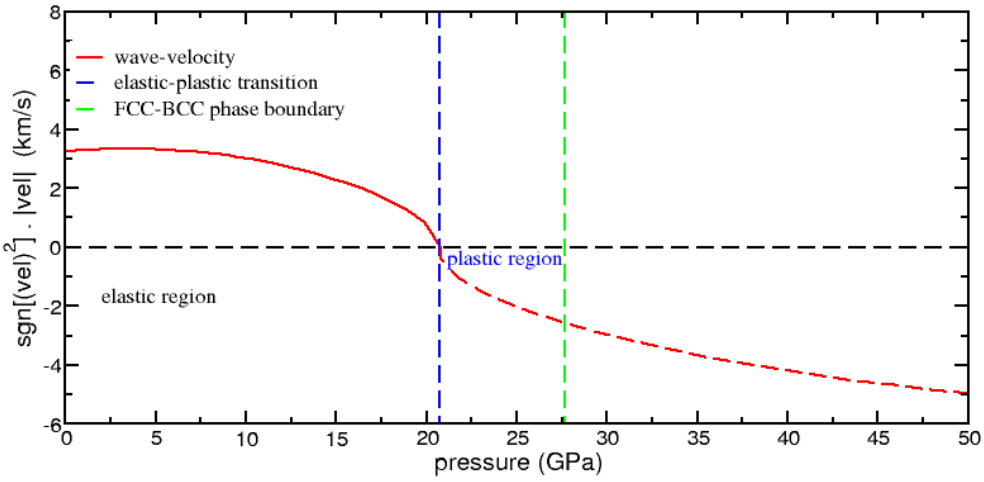

Figure 3.7: Sound velocity as a function of pressure in a perfect crystal Al using ZM potential along (110) direction.

3.3.3 Elastic-Plastic Transition for Compression along (111)

Table 3.4: Determination of strain, stress tensor along z-direction and pressure for elastic plastic transition and phase transformation

$Direction(111)$	ϵ	$P_{zz}(GPa)$	$Pressure(GPa)$
Elastic-plastic	0.22	54.60	34.15
FCC$\longrightarrow$ BCC	0.19	45.37	27.67

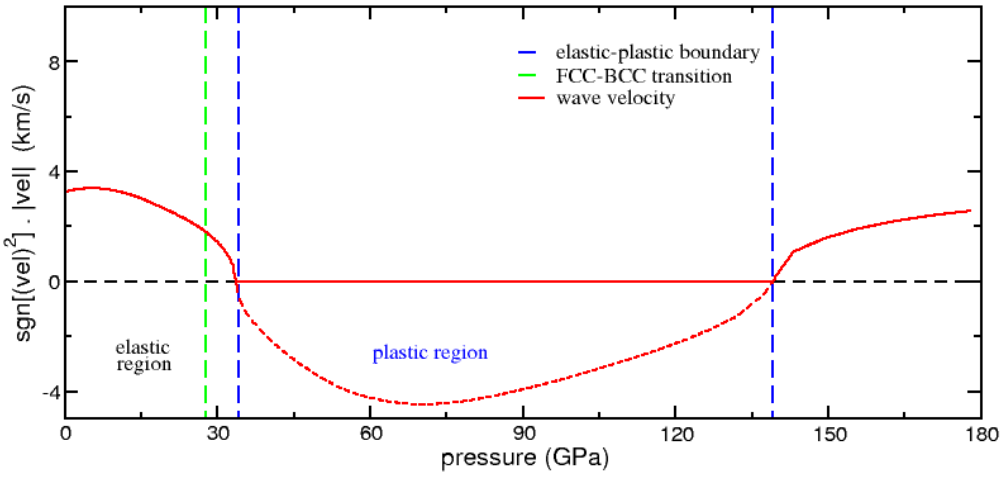

Figure 3.8: Sound velocity as a function of pressure in a perfect crystal Al using ZM potential along (111) direction.

3.4 Summary

In the next chapter, I will show the results and analysis from the study of elastic-plastic transition of FCC crystals in particular ZM[11] model potential under uniaxial quasi-isentropic

compression simulations in a 'very fast' regime and shock using MD simulation. We used the EAM type potential to model the atomic interactions.

Chapter 4

Molecular Dynamics Study of Phase Transitions: FCC $\rightarrow$ BCC

In this chapter we present and discuss our atomistic simulations and results for the fcc $\rightarrow$ bcc phase transition under shock and uniaxial deformation using the ZM EAM model. We studied the plastic deformation in ZM model potential under compression along (100) and (110) directions. Molecular Dynamics (MD) computer simulations on model potential predicts that the elastic-plastic threshold occurs at high HEL along $< 110 >$ comparatively to along $< 100 >$ direction. We also observed the orientation dependence of plasticity. We also show the nature of defect formation for fcc$\longrightarrow$bcc transformation.

4.1 Atomistic Simulations: Details

Initially, we created pristine almost cubic crystal configuration consisting of 80,000-100,000 atoms, by using a crystal generator software. Then the initial configuration was thermalized by compressing in the z-direction at constant temperature of $T = 300K$. This thermalized sample is then used to carry out other MD simulations. The atomic interaction were described by the EAM type ZM model potentials as mentioned in the previous section. In what follows, time will be given in picoseconds (ps) or in dimensionless time units of $t0$ where, $1t0 = 0.05287$ ps. The uniaxial compression was applied along the low-index crystallographic directions: (100) and (110) and (111). However, here we show the simulation details for (100) and (110) directions only. We performed three different types of atomistic simulations:

•Hugoniostat Simulations[13]

•Non-equilibrium Molecular Dynamic Simulation (NEMD)

•Quasi-isentropic Compression (QIC)

After running simulation for a fixed run time, we identified the elastic-plastic transition by sudden increase in temperature, drop in shear stress, and change in pressure.

4.1.1 FCC to BCC Phase Transition Under Isotropic Homogeneous Compression

In order to investigate the kinetics of the fcc $\rightarrow$ bcc phase transition in this model, we performed quasi-isentropic MD simulations with systems comprising $\sim$ 7 million atoms arranged approximately in a cube of dimensions 50 nm x 50 nm x 50 nm. The atoms were initially thermalized at 800K and the system was then homogeneously and isotropically compressed at a volumetric strain rate of $\sim 10^{-9}$ s^{-1} to a final volume corresponding to a pressure of about 33 GPa (above the fcc–bcc transition pressure of $P =$ 27 GPa). The simulations were performed utilizing the Los Alamos code SPaSM[28],[29]

Figure 4.1 shows a series of snapshots of the atomic configuration at three different times during the simulation. The top frames show atoms colored according to their corresponding phase (blue=fcc, red=bcc, yellow=unknown). The phase identification was obtained by performing a common neighbor analysis. From the time evolution analysis, the fcc-bcc commences within $\sim$ 5 ps and most atoms have transform to bcc by 50 ps. The bcc to fcc volume fraction is shown in Fig. 4.2. The decrease in FCC atoms are supplemented by increment of BCC atoms. The phase diagram and melt temperature of this model system is shown in Fig. 4.3. The equilibrium melt curve (fcc and bcc) of the ZM model was determined from solid-liquid co-existence simulations[?] over a pressure range between 0-100 GPa. The results were fitted to a Simon equation,[31] $T_m(P) = T_0(1 + P/\alpha)^\beta$ for each phase. The phase which melted at the higher temperature was chosen as the most stable phase and the intercept of the fcc and bcc melt lines was identified as the triple point for this

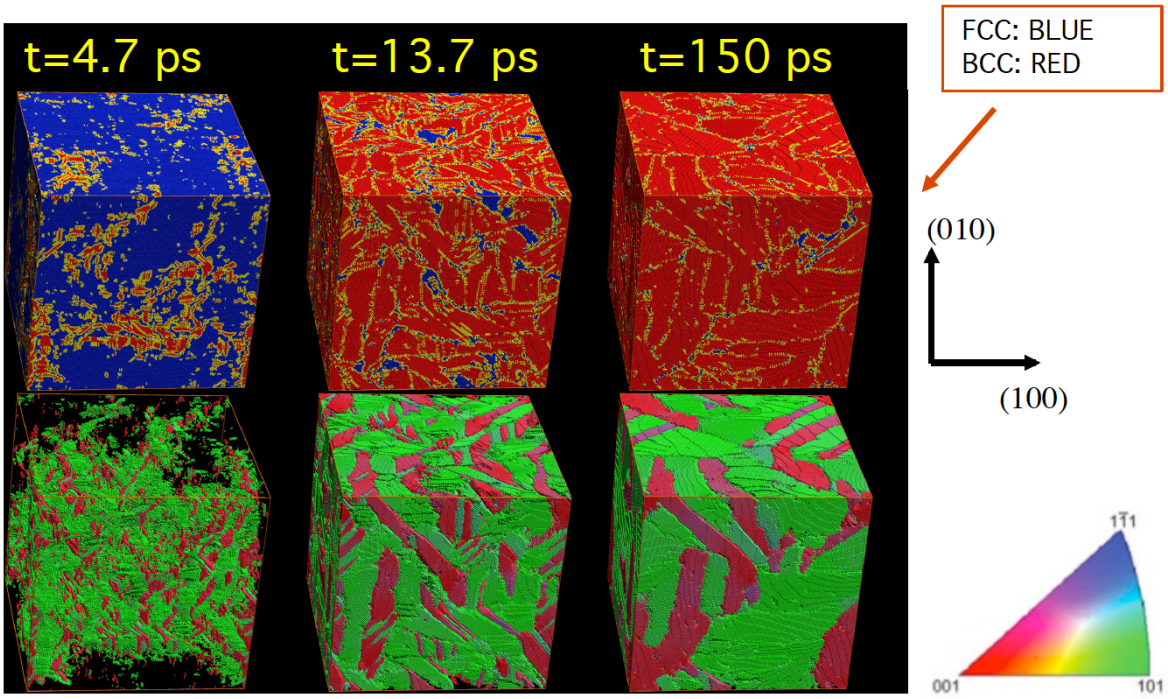

Figure 4.1: Time snapshots of phase transformation in ZM potential compressed isotropically to a final strain of 27%. The top sequence shows atoms colored according to their local coordination; blue FCC and red BCC. And any other colors indicate interfaces and other defects. The bottom sequence shows bcc atoms which are colored according to an orientation order parameter[30]. Here different colors correspond to different grains of bcc daughter phase.

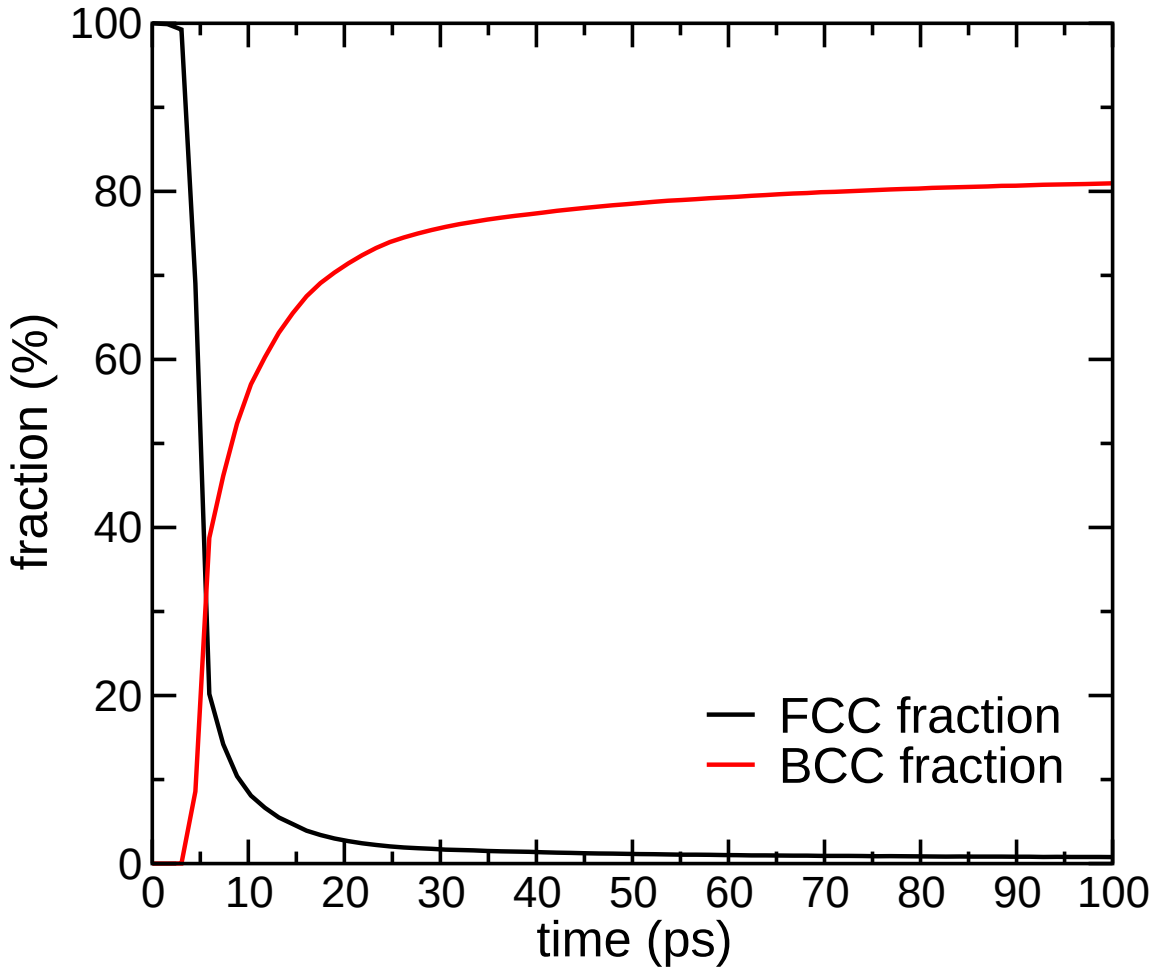

Figure 4.2: Fcc and bcc fraction as a function of time for isotropic homogeneous compression at 27% strain.

system[32]. Also shown in Fig. 4.3 is a data point corresponding to the pressure-temperature final state of the 7 million atoms molecular dynamics simulation discussed above.

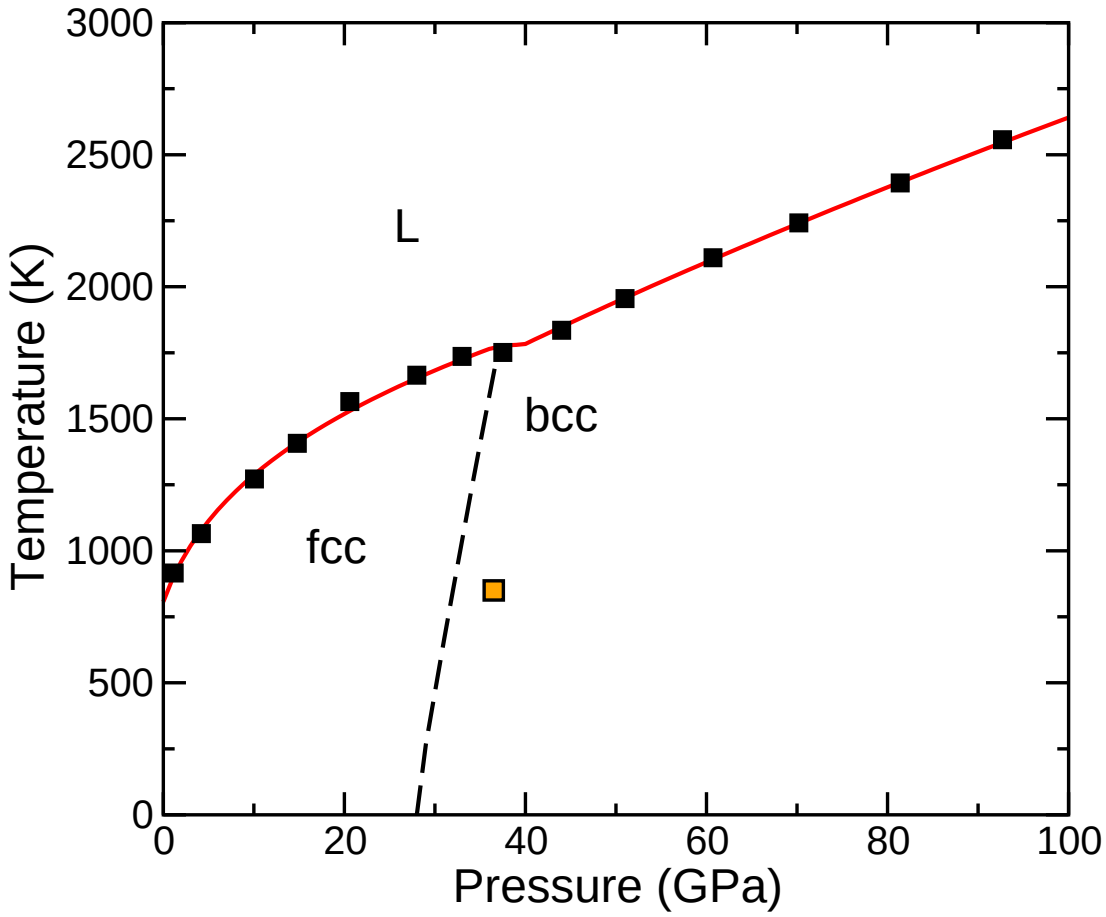

Figure 4.3: Phase diagram of ZM potential for isotropic homogeneous compression.

4.1.2 Simulation Results for ZM Model Potentials for Compression along (100)

Hugoniostat Simulations

We carried out constant-stress (constant P_{zz}) Hugoniostat[13] simulations with sample of 80,000 atoms arranged approximately in a cube (26x26x29). We took an unshocked configuration vibrating about unstrained crystal lattice sites (at initial pressure $P_0 = 0$, volume V_0, and internal energy E_0 and low temperature $T_0 = 300K$). We compressed the crystals uniaxially and homogeneously (dynamically) to a final preset normal stress value (P_{zz} = 10-75 GPa) in the direction (z) of the shock. ν_H and ν_p are frequencies described by the

Table 4.1: Summary of temperature controlling parameters for Hugoniostat simulation at constant stress along (100).

Shock direction	V_0 ($\AA^3$)	E_0 (eV/atoms)	ν_H	ν_p	β_H	β_p
(100)	16.857	-3.28	-12.00	0.2	12.00	0.5

equations (2.59-2.60) in Chapter-2 and equations (2.56-2.66) were used to compute the trajectory of the normal stress as a function of volume with a time step $dt = 0.01t_0$. Here the stress and temperature evolves dynamically and naturally. The value of ν_p is chosen so as to reproduce as closely as possible the strain-rate produced by the passage of an NEMD shock wave through the crystals. The time evolution of the stress tensors and temperature resembles very closely that generated in NEMD. The internal energy set initially (E_0) relaxes to the final shocked-state energy (Hugoniot energy). And the change from initial to final state gives the work done by the piston plus the heat flow into the system.

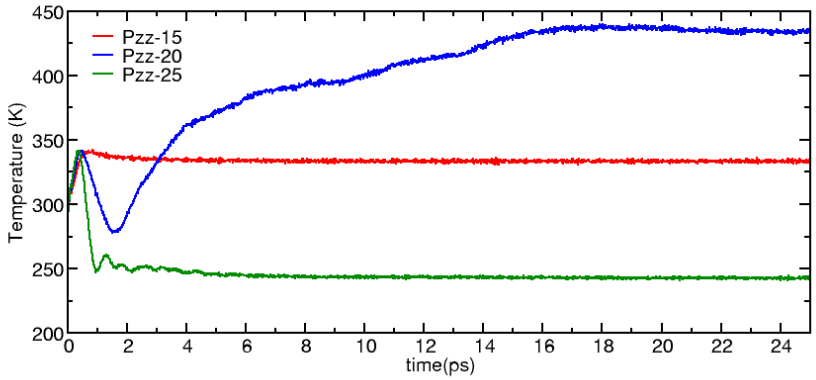

Figure 4.4: Typical temperature profiles from Hugoniostat simulations of shock wave propagation along (100) to a final P_{zz} of 15, 20 and 25 GPa, utilizing the ZM model potential.

The 'jump' in temperature as a function of time can be correlated with elastic-plastic transition or a structural phase transformation.

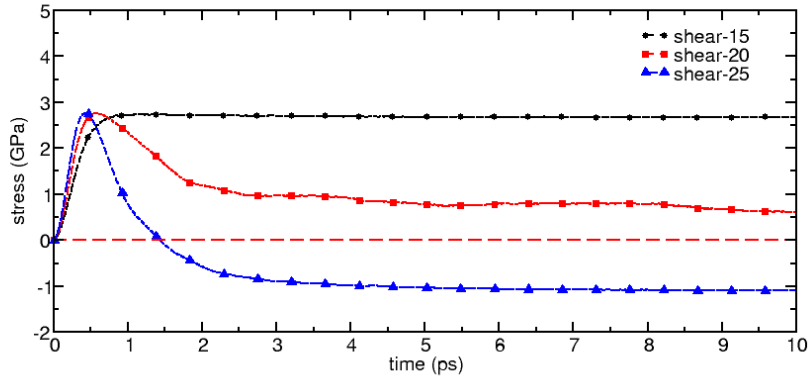

Figure 4.5: Stress profile for Hugoniostat simulation of ZM model potentials along (100).

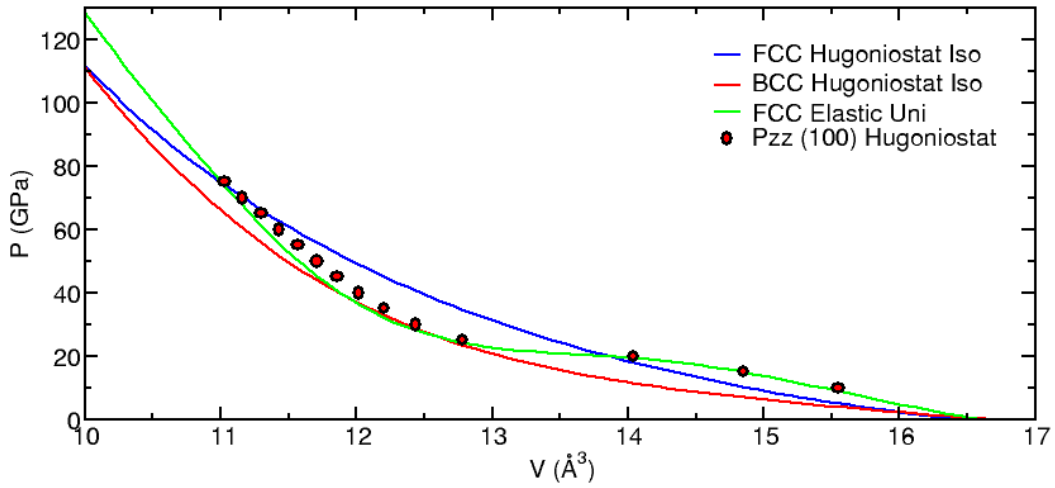

Figure 4.6: Pressure-Volume Hugoniot of ZM model potential for wave propagation along (100), obtained from Hugoniostat simulations (filled circles); isotropic Hugoniot of BCC phase (red-line) and FCC phase (blue line) . Also shown is the zero-temperature longitudinal stress or elastic EOS (green line).

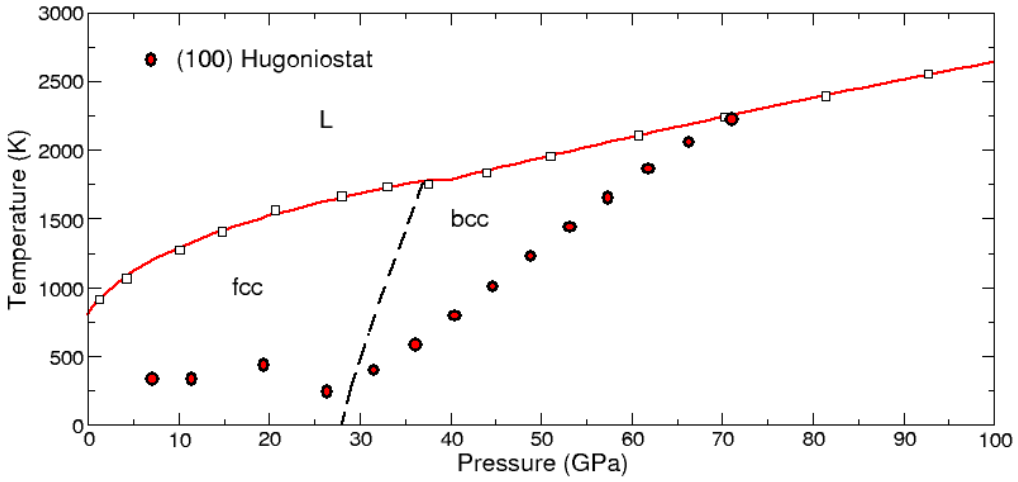

Figure 4.7: Phase diagram of ZM model potentials for Hugoniostat simulation along (100).

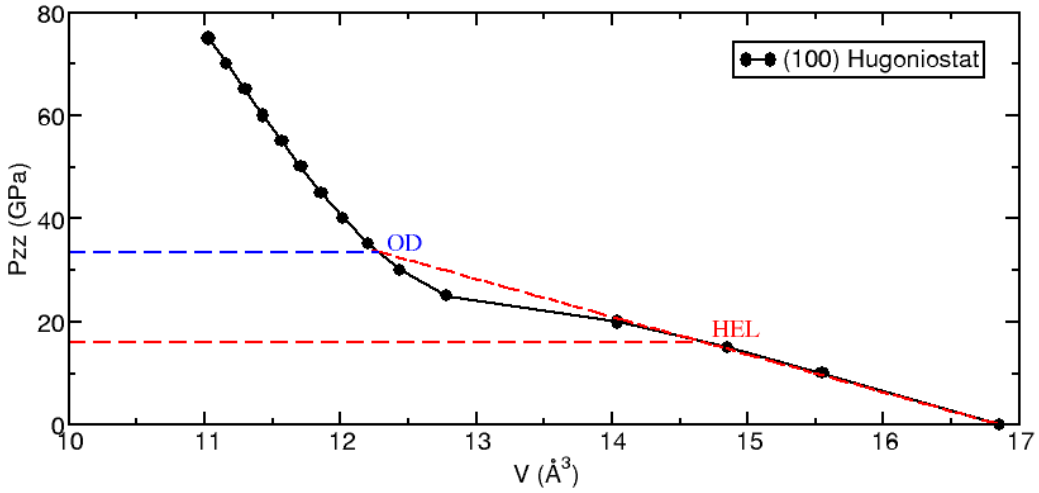

Figure 4.8: A Hugoniot along (100). The dashed curve between the Hugoniot elastic limit (HEL) and the over-driven (OD) points is a region of the Hugoniot inaccessible from the initial state ($P_{zz} = 0$, $V_0 = 16.857$ $\AA^3$. It is characterized by an elastic wave travelling at ${u^{HEL}}_s$ (i.e. (V_0, P_0)-HEL line) and a plastic wave whose velocity $u_s < {u^{HEL}}_s$.

The region of the Hugoniot between the HEL and the OD points, indicated by the dashed curve, corresponds to shock states inaccessible from the initial state. Shock states in this region (in between HEL and OD), are characterized by a two-wave structure: an elastic wave that compresses the material up to the HEL and travels with a velocity ${u^{HEL}}_s$, and a plastic wave that compresses the material from the HEL to the intermediate state and travels at $u_s < u_s^{HEL}$. Slopes of the straight $P-V$ lines (Rayleigh lines) are proportional to the square of the wave speeds. The plastic wave speed u_s increases with shock compression until $u_s = u_s^{HEL}$. This condition gives the OD point. For compression above OD, plastic wave speed exceeds the elastic, which give rise to a single-plastic wave state.

Table 4.2: Determination of Hugoniostat limit for (100).

$Direction$	ϵ_{HEL}	$P_{HEL}(GPa)$	ϵ_{OD}	$P_{OD}(GPa)$
(100)	-0.129	15.9985	-0.272	33.598

In order to check the accuracy of the Hugoniostat simulation results, we carried out multimillion-atom NEMD simulations in the elastic-plastic region of the Hugoniot.

Shock Compression Simulations

We studied shock compression via large-scale (multi-million atom) NEMD and constant-stress Hugoniostat simulations. The large-scale NEMD simulations were performed with the Los Alamos National Laboratory massively parallel MD code SPaSM[28],[29] for system with a 80nm x 80nm x 980nm slabs and sizes containing up to 380 million atoms, in which atoms were arranged in a perfect fcc $< 100 >$ and $< 110 >$ rectangular crystal slab. The periodic boundary conditions were imposed in the transverse (x and y) directions. The shock wave propagation follows Rankine-Hugoniot conditions as given by equations (2.30-2.32) in Chapter-2. And for a shock propagation along z-direction, the final shock state is given by equations (2.33-2.34) described in the chapter-2. We generated a shock wave by pushing a material by an infinitely massive piston moving at velocity u_p. All particles coming in contact with the piston face were specularly reflected by a flat momentum mirror. This is equivalent to keeping piston at rest such that the unshocked target material is given an initial velocity of $-u_p$. The shock wave then moves out from the stationary piston face at velocity $u_s - u_p$. In the shock front region, we obtained shock-wave profiles from NEMD simulations, such as stress profiles, normal and transverse to the propagation direction and shear stress τ. We performed shock simulation for a range of particle velocities and up to 1.8 km/s (P = 33 GPa).

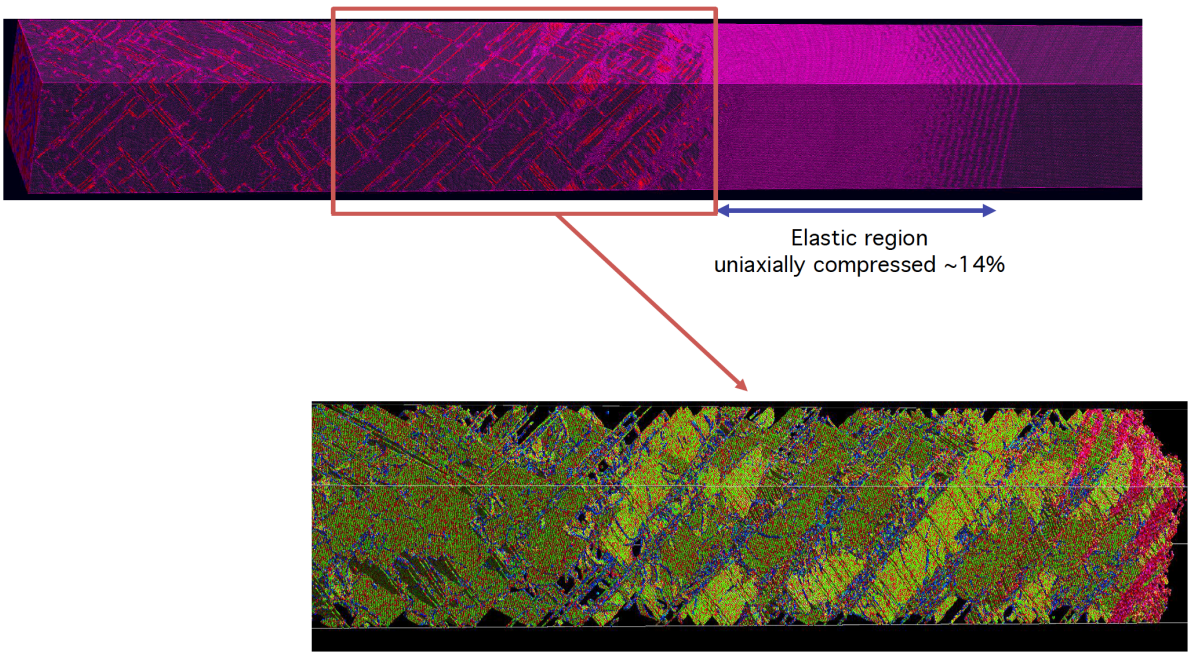

Figure 4.9: Atomic configurations of Al shocked to a particle velocity $u_p = 1.1\ km/s$ ($P = 19$ GPa) and below transition pressure 27 GPa. Atoms are colored according to local co-ordination.

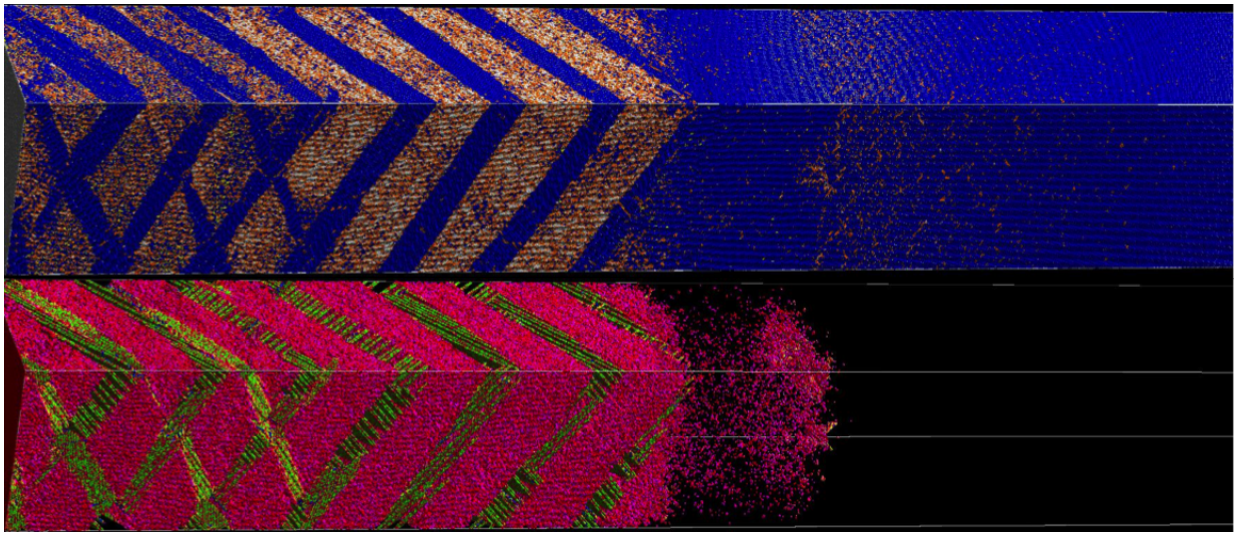

Figure 4.10: Atomic configurations of Al shocked to a particle velocity $u_p = 1.48\ km/s$ ($P = 26$ GPa). In the top frame, atoms are colored according to local co-ordination: blue being fcc and brown being fct. In the last frame, atoms are colored according to CSP (Centro symmetry parameter)

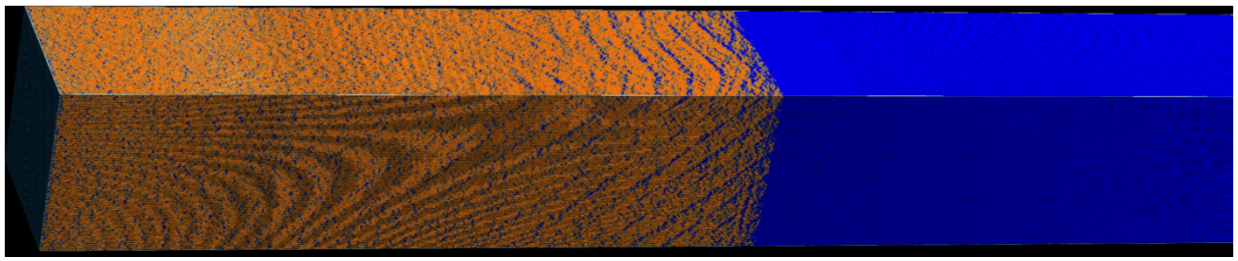

Figure 4.11: Atomic configurations of Al shocked to a particle velocity $u_p = 1.8\ km/s$ ($P = 33$ GPa) and above transition pressure 27 GPa. In the top frame, atoms are colored according to local co-ordination: blue being fcc and brown being fct. In the last frame, atoms are colored according to CSP (Centro symmetry parameter)

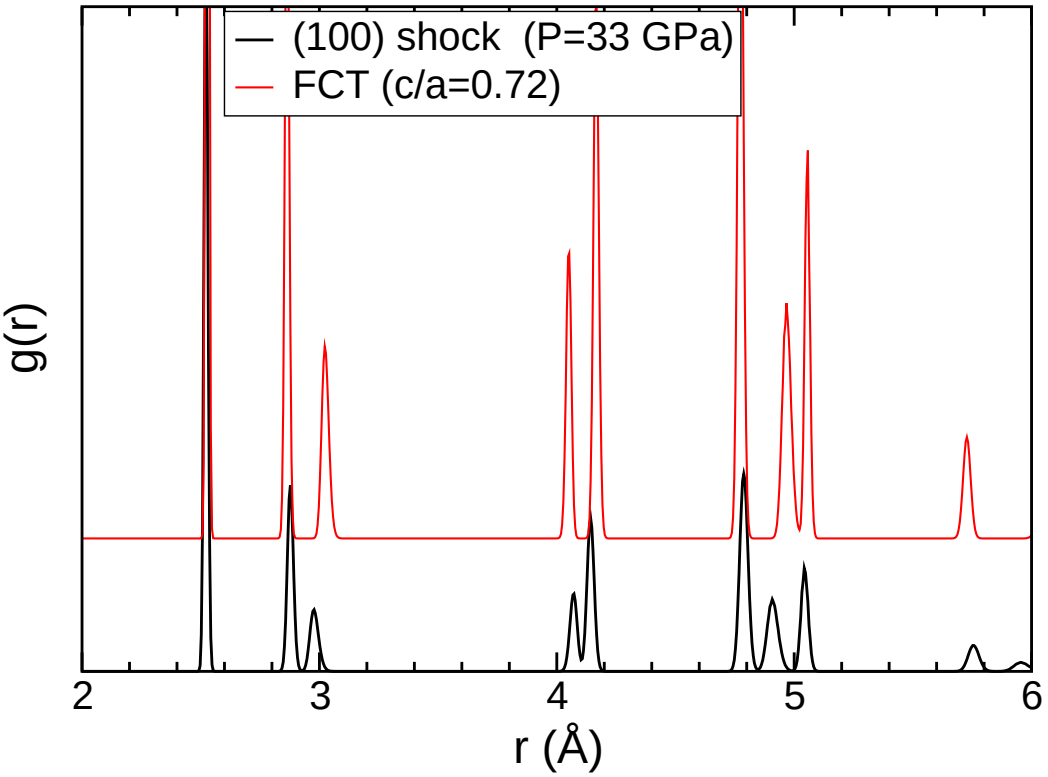

Figure 4.12: Along the (100) direction at the particle velocity of $u_p = 1.8km/s$.

To compare shock simulation result, we also performed quasi-isentropic compression.

Quasi-isentropic Compression

The initial configuration was compressed in the z-direction at constant temperature at 300K. We performed the constant strain rate quasi-isentropic MD simulation of metallic single crystals. The simulation consists of about 44 million atoms. A simulation box was compressed uniaxially and deformed quasi-isentropically along the z-direction. The maximum constant strain rate was computed using final preset strain and total time for

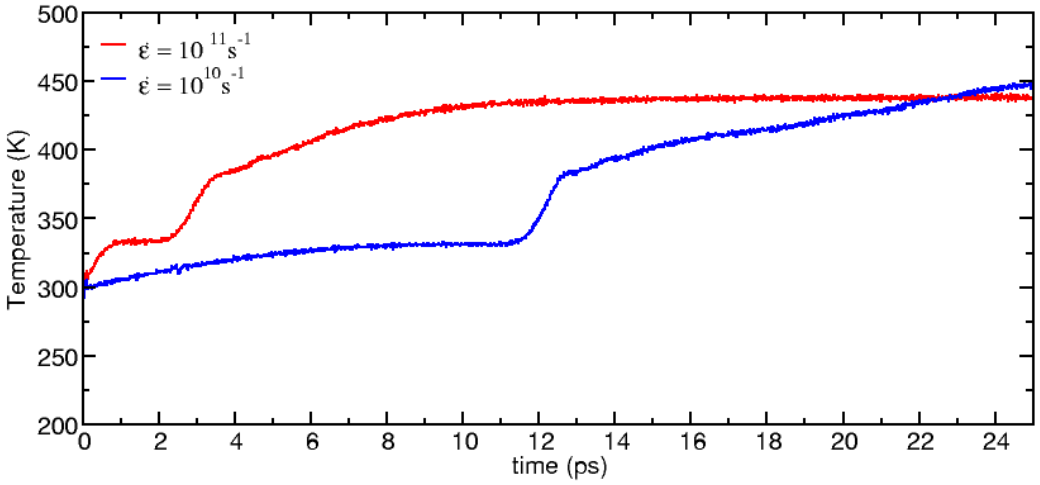

Figure 4.13: Temperature time profile for compression along (100) to a final strain of 14% at two different strain rates

compression (t_{rise}). The equation of motions described in equation (2.35-2.46) of Chapter-2 were used to compute the time evolution of the system. The following figures Fig. 4.10 and Fig. 4.11 show the Normal stress time profile of fast compression ($\dot{\varepsilon} = 10^{12}$ s^{-1} and normal stress time profile at a slower compression rate ($\dot{\varepsilon} = 10^{11}$ s^{-1}) respectively. The time step was about 1 femtosecond. The elastic-plastic transition can be identified by a marked jump in the temperature and a reduction in the shear stress.

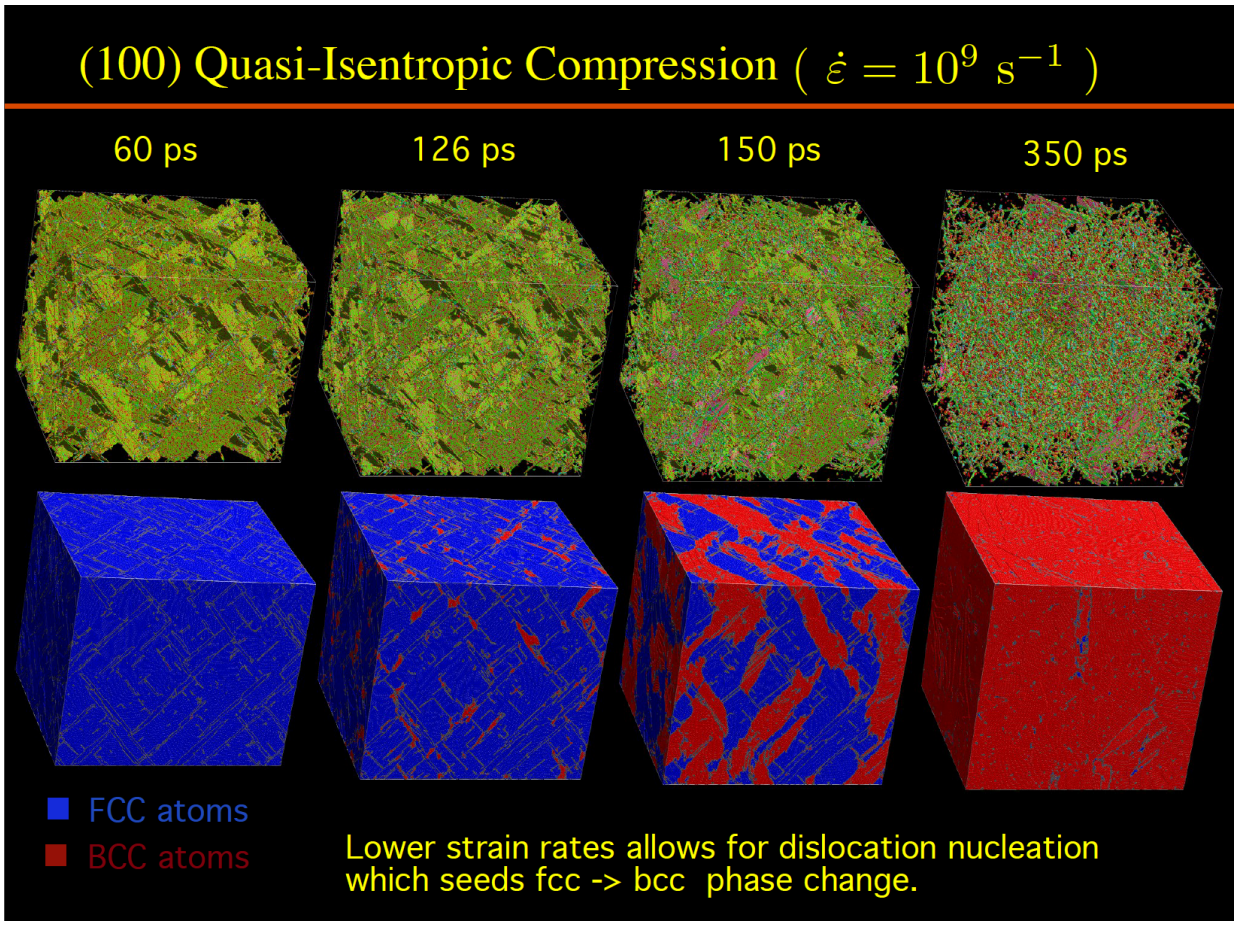

Figure 4.14: Time snapshots at a 60 ps, 126 ps, 150 ps, and 350 ps(left to right) of deformation in ZM potential compressed quasi-isentropically by strain-rate $\dot{\epsilon} = 10^9\ s^{-1}$. The top sequence shows atoms which are colored according to centro symmetry parameter. The bottom sequence shows atoms colored according to local coordination; blue FCC and red BCC.

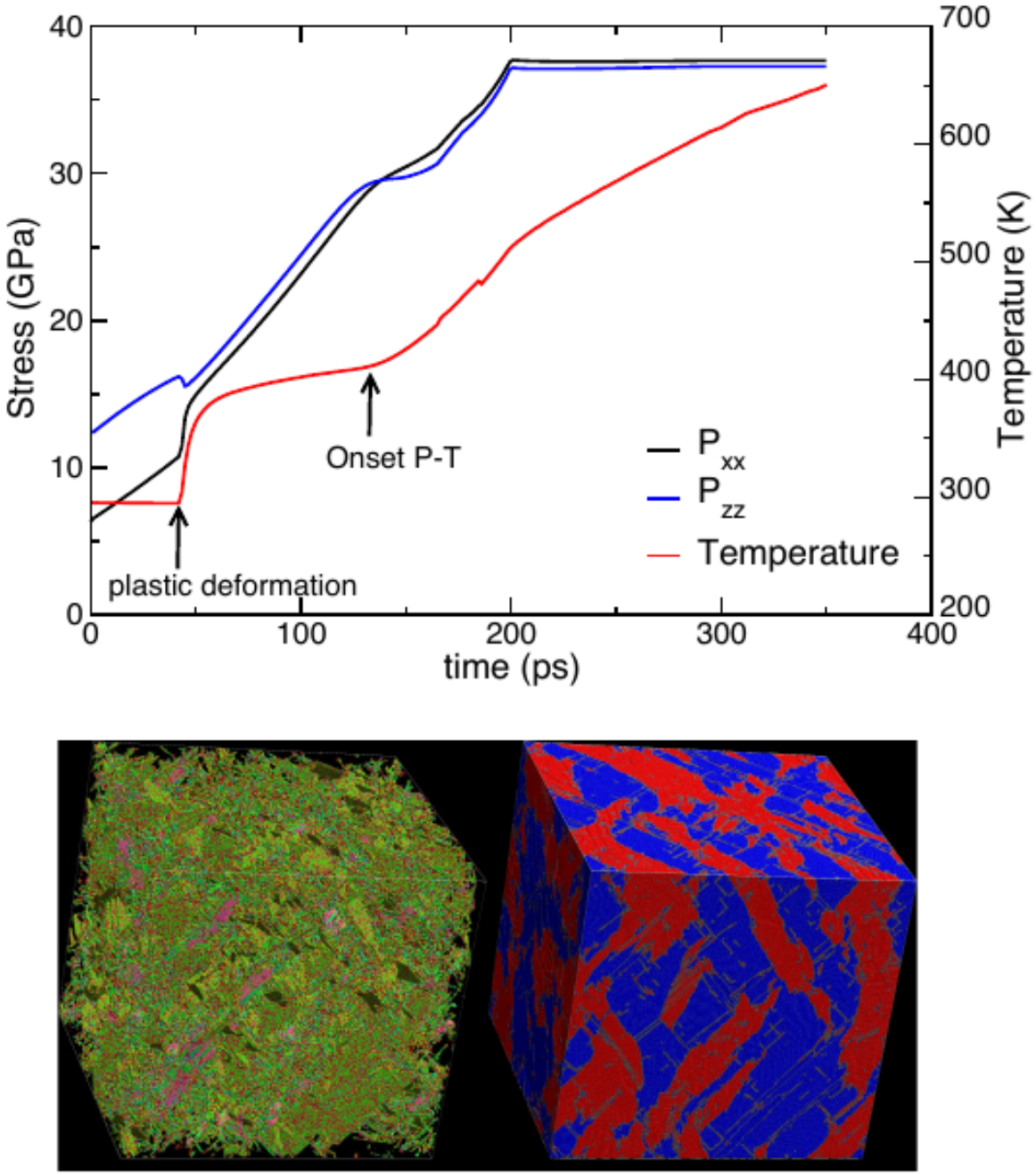

Figure 4.15: The top graph shows stress and temperature profiles and the bottom frame shows deformation in ZM potential for quasi-isentropic compression along (100) direction at the strain rate $\dot{\epsilon} = 10^9\ s^{-1}$ and pressure $P = 36$ GPa.

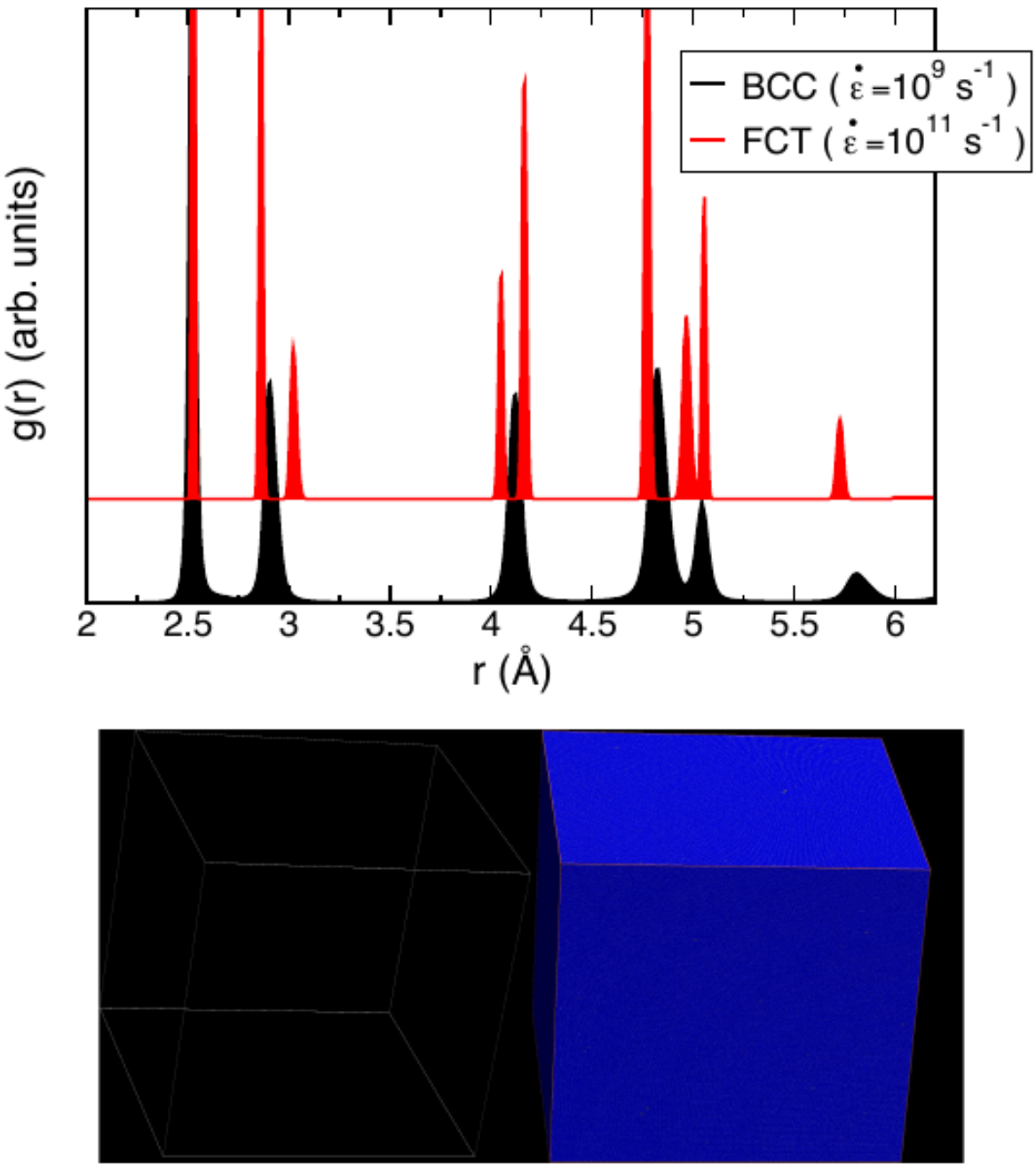

Figure 4.16: The top graph shows RDF comparison between bcc and fct structures and the bottom frame shows deformation in ZM potential for quasi-isentropic compression along (100) direction at the strain rate $\dot{\epsilon} = 10^{10} - 10^{11}\ s^{-1}$.

4.1.3 Simulation Results For ZM Model Potentials For Compression Along (110)

Hugoniostat Simulation

Similar to (100) direction, we also carried out constant-stress (constant P_{zz}) Hugoniostat simulations with sample of 80,000 atoms arranged approximately in a cube. It follows the same equation of motion as compression along (100). That is equations 2.30-2.34 of Chapter-2. ν_H and ν_p are frequencies and are given in the equations (2.59-2.60) described

Table 4.3: Summary of temperature controlling parameters for Hugoniostat simulation at constant stress for compression along (110).

Shock direction	V_0 ($\AA^3$)	E_0 (eV/atoms)	ν_H	ν_p	β_H	β_p
(110)	16.8567	-3.28036	-12.00	0.2	12.00	0.5

in Chapter-2 and equations (2.56-2.66) were used to compute the trajectory of the normal stress as a function of volume with a time step $dt = 0.01t_0$.

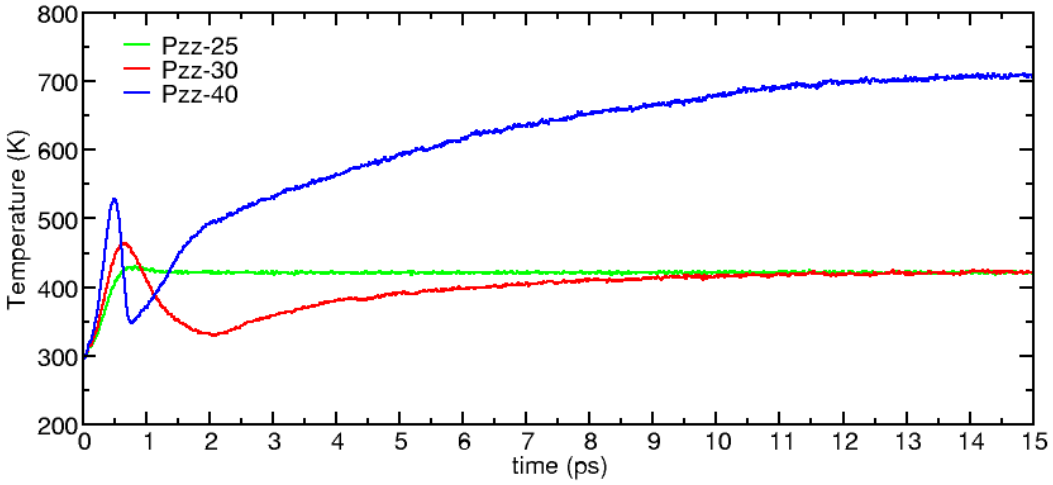

Figure 4.17: Temperature profile for Hugoniostat simulation of ZM potential along (110).

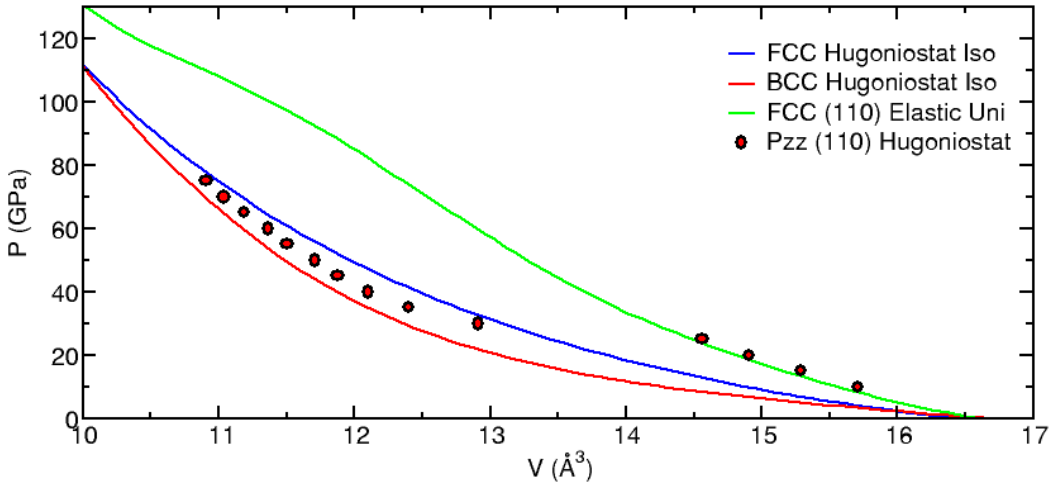

Figure 4.18: Pressure as a function of volume for ZM model potential for (110).

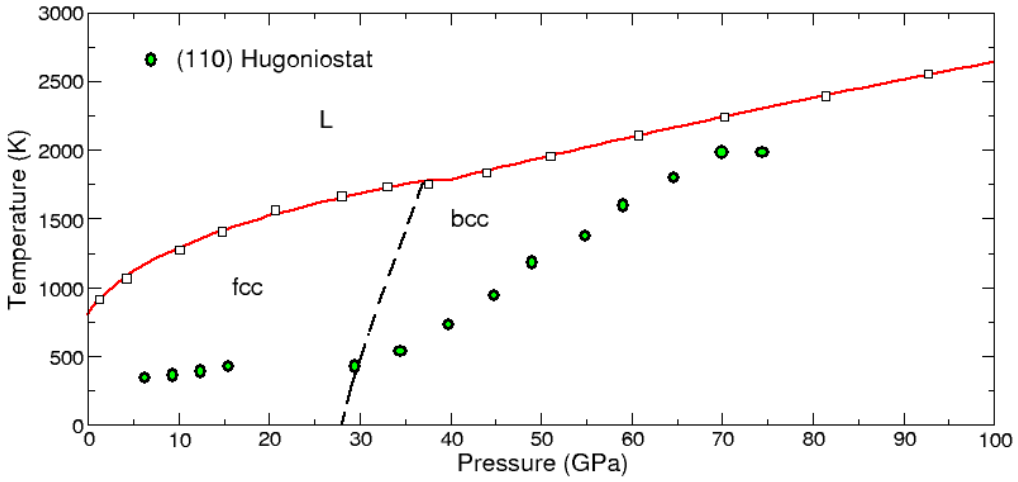

Figure 4.19: Phase diagram of ZM model potential for Hugoniostat simulations along (110).

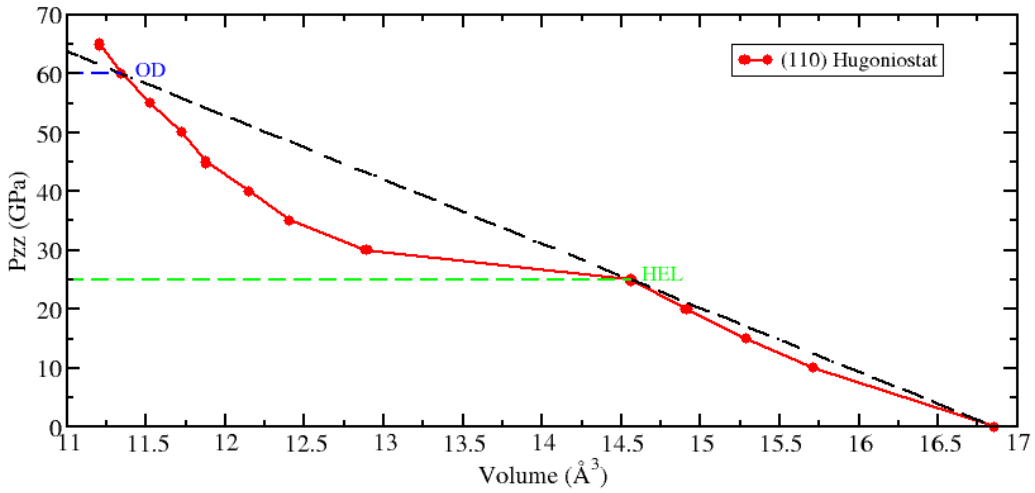

Figure 4.20: A Hugoniot along (110). The dashed curve between the Hugoniot elastic limit (HEL) and the over-driven (OD) points is a region of the Hugoniot inaccessible from the initial state ($P_{zz} = 0$, $V_0 = 16.8567$ $\mathring{A}^3$. It is characterized by an elastic wave travelling at ${u^{HEL}}_s$ (i.e. (V_0, P_0)-HEL line) and a plastic wave whose velocity $u_s < {u^{HEL}}_s$.

The region of the Hugoniot between the HEL and the OD points, indicated by the dashed curve, corresponds to shock states inaccessible from the initial state. Shock states in this region (in between HEL and OD), are characterized by a two-wave structure: an elastic wave that compresses the material up to the HEL and travels with a velocity ${u^{HEL}}_s$, and a plastic wave that compresses the material from the HEL to the intermediate state and travels at $u_s < u_s^{HEL}$. Slopes of the straight $P-V$ lines (Rayleigh lines) are proportional to the square of the wave speeds. The plastic wave speed u_s increases with shock compression until $u_s = u_s^{HEL}$. This condition gives the OD point. For compression above OD, plastic wave speed exceeds the elastic, which give rise to a single-plastic wave state.

Table 4.4: Determination of Hugoniostat limit for (110).

$Direction$	ϵ_{HEL}	$P_{HEL}(GPa)$	ϵ_{OD}	$P_{OD}(GPa)$
(110)	-0.136	25.0	-0.327	60.0

Shock Simulation

The large-scale NEMD simulations were performed with the Los Alamos National Laboratory massively parallel MD code SPaSM for system with containing up to 380 million atoms, in which atoms were arranged in a perfect fcc $<$ 110 $>$ rectangular crystal slab. The periodic boundary conditions were imposed in the transverse directions. Shock simulation along (110) also follows exactly the same equation of motion as in the case of (100) mentioned above.

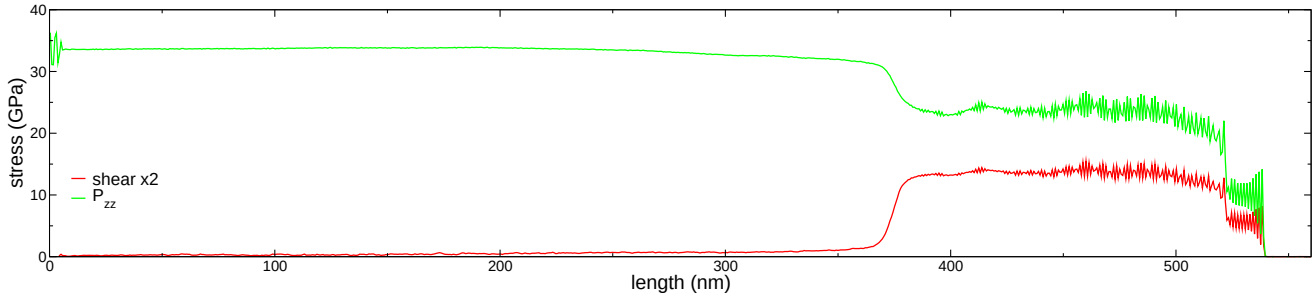

Figure 4.21: Stress profile for shock propagation along (110) and particle velocity of $u_p = 1.8$ km/s (P=33 GPa)

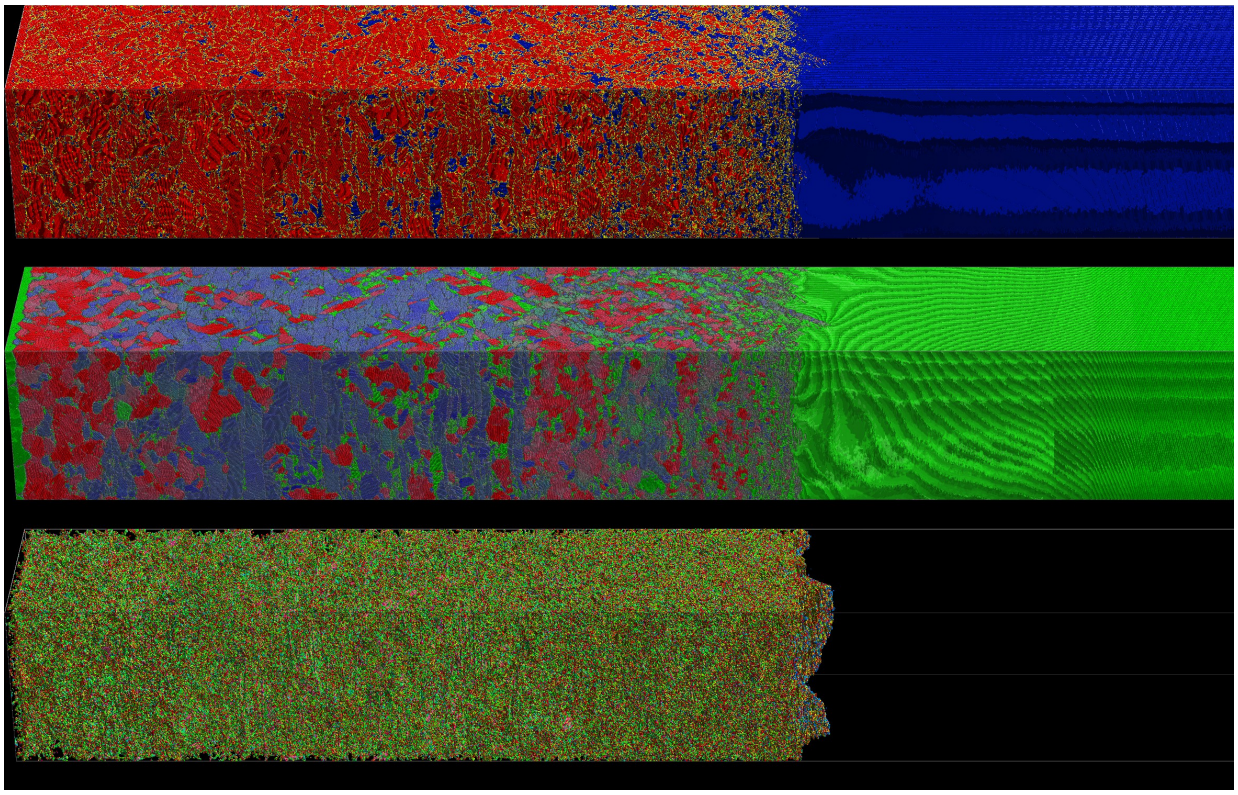

Figure 4.22: Atomic configurations in ZM model potential shocked to a particle velocity $u_p = 1.8\ km/s$ ($P = 33$ GPa). In the top frame, atoms are colored according to local co-ordination: blue being fcc and red being bcc. In the middle frame, atoms are colored according to an orientation order parameter. In the last frame, atoms are colored according to CSP (Centro symmetry parameter)

We also carried out QIC along (110) to compare the result with shock simulations. Here the final pressure = 83 GPa for a system size of (40nm x 40nm x 56 nm) 5.6 million atoms.

Quasi-isentropic Compression

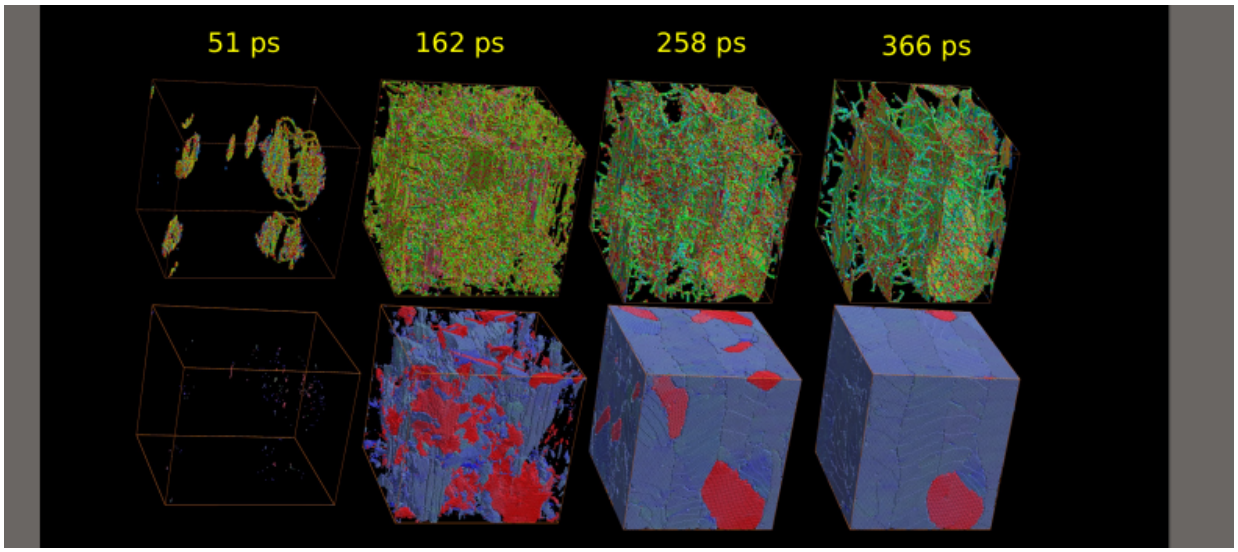

Figure 4.23: Time snapshots of deformation in ZM potential compressed quasi-isentropically by strain-rate $\dot{\epsilon} = 10^9\ s^{-}1$. The top sequence shows non-centro symmetric atoms. The bottom sequence shows only BCC atoms, which are colored according to orientation with respect to (110) direction.

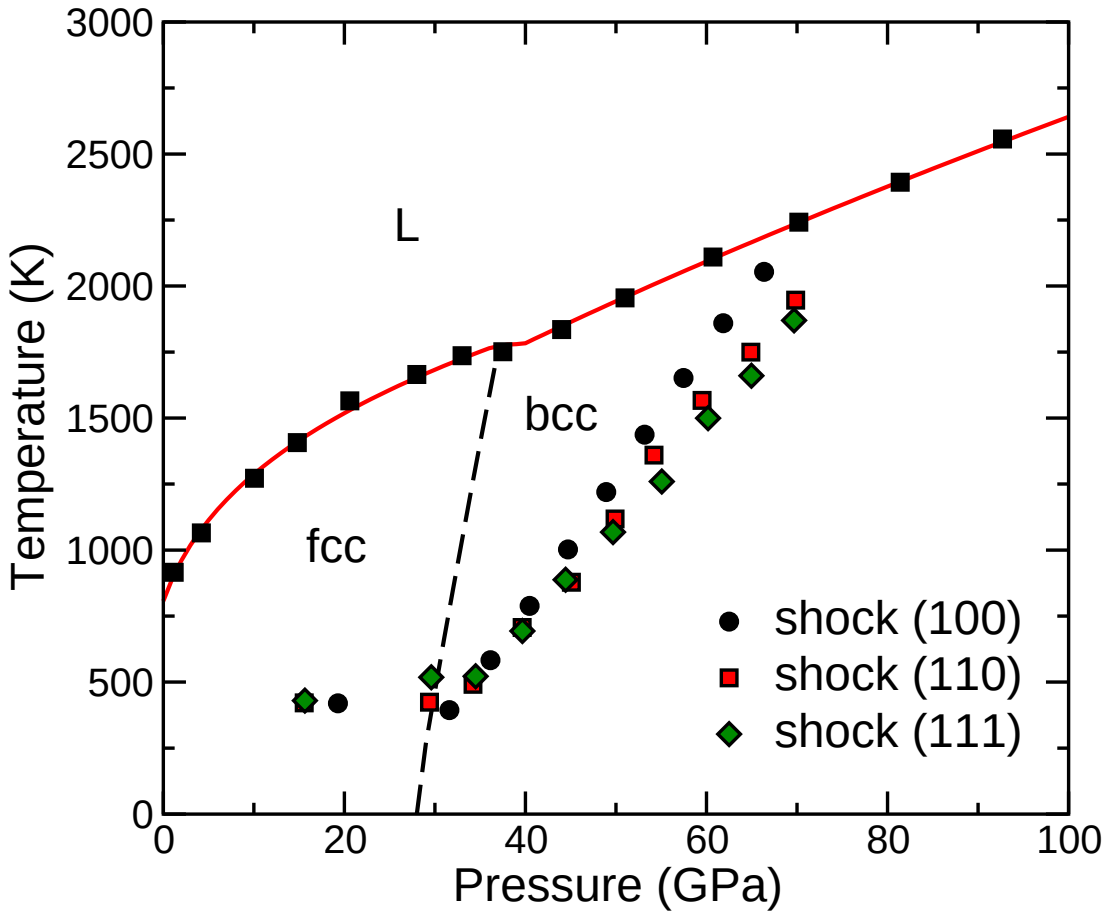

Figure 4.24: Equation of state for ZM potential compared with shock temperatures along (100), (110) and (111) directions.

In the next section, we analyse of our results from each simulations.

4.2 Observation of Plasticity

The following Figure 4.22 and Figure 4.24 predicted that the wave-propagation instabilities occur when wave velocity is 0. The point where instability occurs is where elastic-plastic transition takes place.

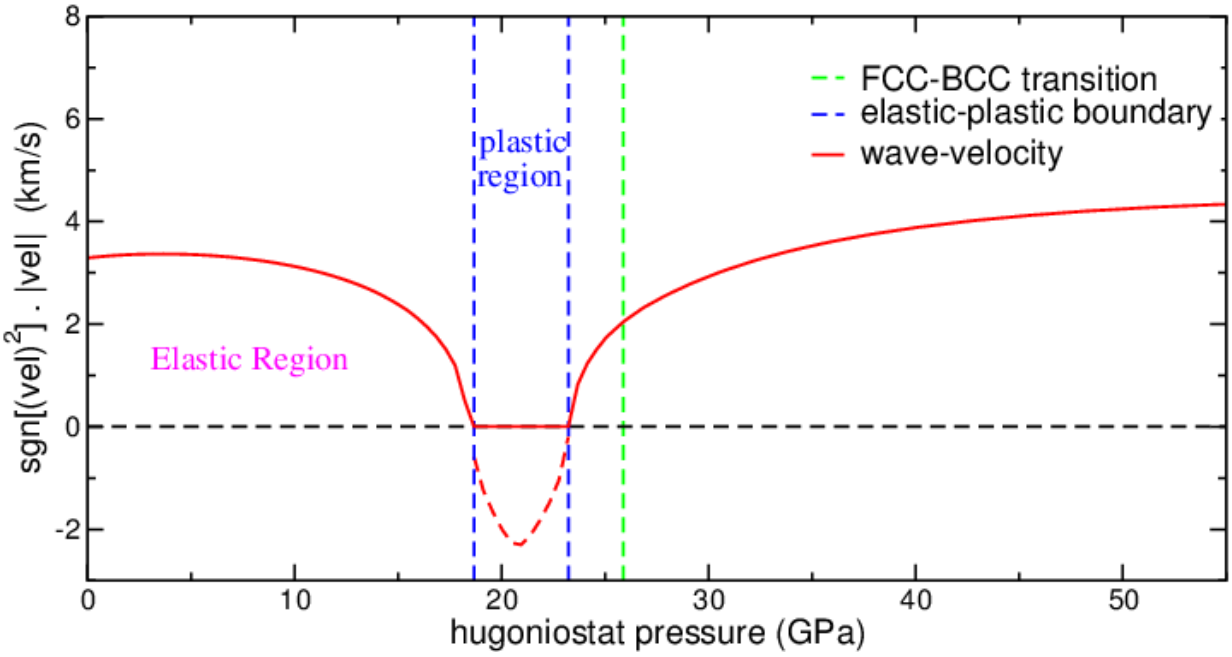

Figure 4.25: Sound velocity as a function of Hugoniostat pressure for a ZM model potentials along (100) direction at $T = 0$ K.

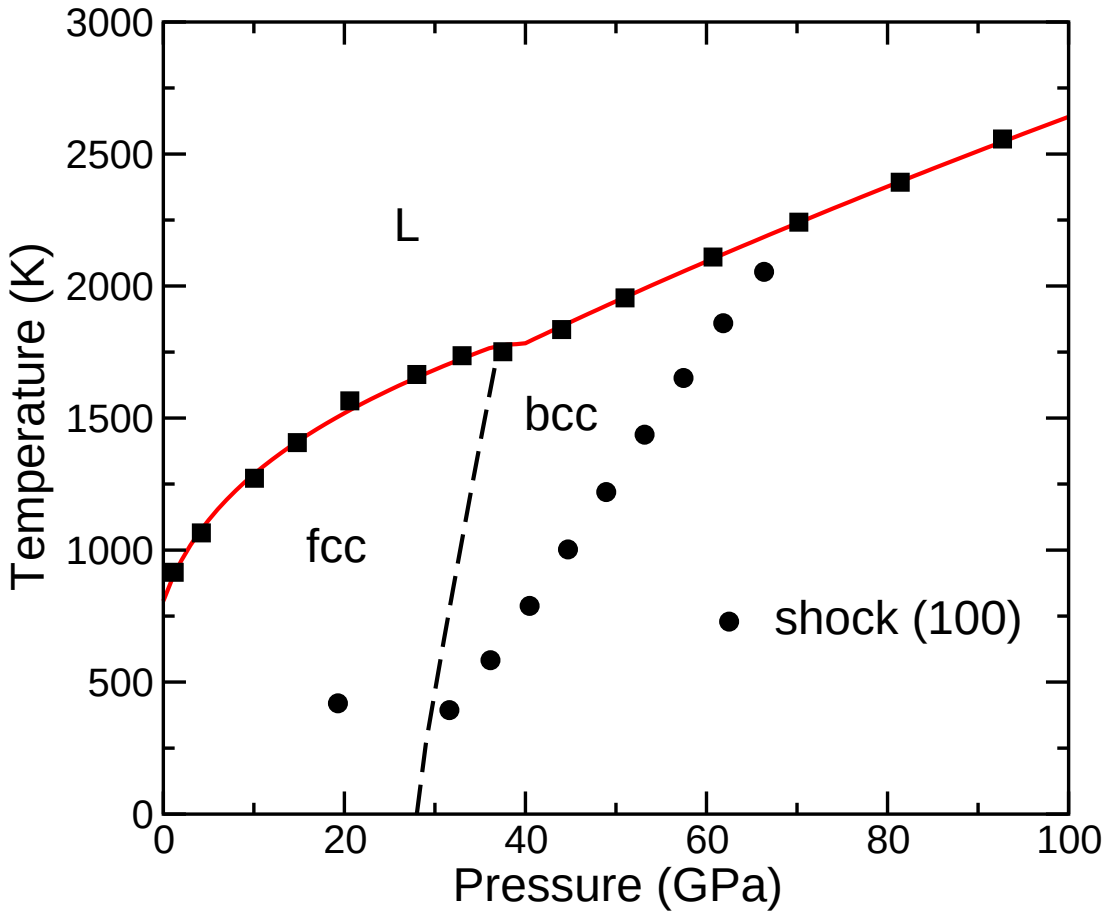

Figure 4.26: Phase diagram of ZM model potential for compression along (100).

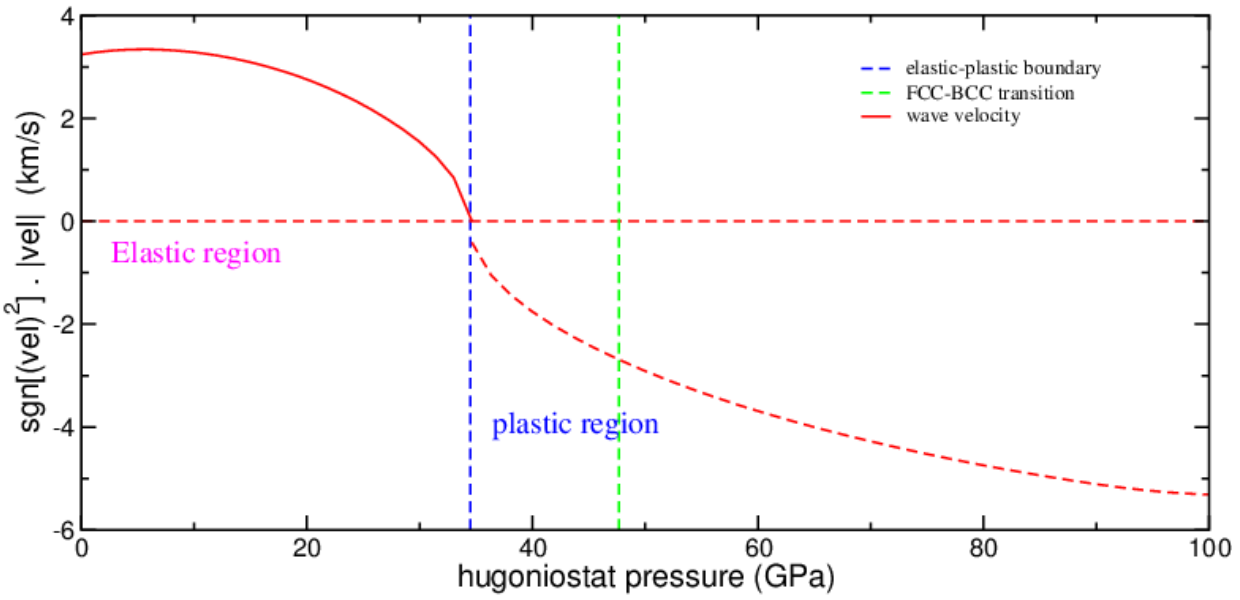

Figure 4.27: Sound velocity as a function of Hugoniostat pressure for a ZM model potential compressed along (110) at $T = 0$ K. direction.

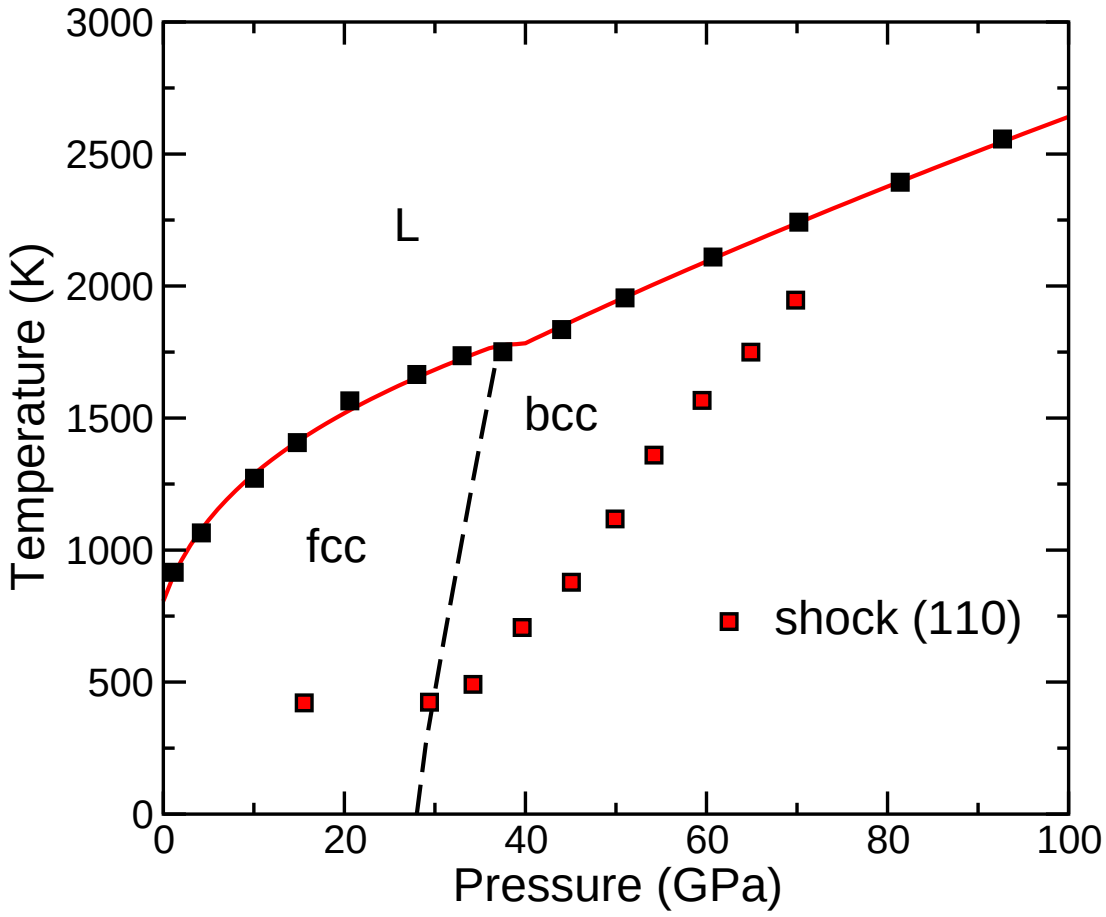

Figure 4.28: Phase diagram of ZM model potential for shock compression along (110).

In the region between two blue dashed lines (elastic-plastic boundary) in Figure 4.22 and Figure 4.24, pressure P must be equal to normal stress P_{zz} (Hugoniostat pressure). Since from the instability curves for (100) and (110), the elastic-plastic transition are at different Hugoniot pressures, different plastic deformation in phase change was predicted for shock propagation along (100) and (110).

We expected plasticity only in the short region (18.5 -23.5 GPa) before phase change, for the compression along (100) (Figure 4.22), whereas along (110), we predicted the occurrence of plastic deformation for a wide-range of Hugoniot pressure ($>$ 35) GPa (Figure 4.21). Our independent evaluation of the elastic-plastic boundary from MD simulations confirms our prediction. The shock simulation along (100), as shown in the Figure 4.6 for 19 GPa (the pressure below phase transition 27 GPa), we found that the plastic zone is characterized primarily by stacking faults. But the plastic zone disappears above $P_{zz} =$ 22 GPa, and around nominal pressure (P = 26 GPa) as shown in the Figure 4.7. Therefore, for (100) direction, we observed split wave-structure but no phase transition in pico-second time scales as the compressed state was fct with varying c/a ratio as shown in the Figure 4.8. From QIC along (100) direction, at higher strain rate we do not observed fcc$\longrightarrow$ bcc phase change. However, a lower strain-rate allows for dislocation nucleation which eventually give rise to fcc$\longrightarrow$bcc phase change. No plasticity or phase change observed for high strain rates in a fast regime $10^{10} - 10^{11}$ $s^{-}1$. For (110), the elastic-plastic transition was predicted for pressures above 20 GPa. However, for shock compression, plastic deformation creates an isotropic plastic state at a pressure in the bcc region of the phase diagram. Therefore, (110) shocks have plastic deformation at the shock front followed by fcc$\longrightarrow$bcc phase change behind as shown in the Figure 4.20. Therefore, the dislocation emission precedes phase change behind shock front.

4.3 Kinetics Effects on Structural and Elastic-Plastic Transitions

Phase transformation do not occur instantaneously. We described the time-dependence of phase transformation at a given temperature in terms of the time dependence of the fraction of transformation. As shown in the Figure 4.13, when we compressed approximately cubic structure quasi-isentropically (100), at a slow strain rate $\dot{\epsilon} = 10^9$ s^{-1}, we observed that

the homogeneous nucleation of dislocation give rise to phase transition fcc$\longrightarrow$bcc. In other words, nucleation of the equilibrium structure takes time and the phase change is delayed. However, for fast strain rate compression ($\dot{\epsilon} = 10^{10} - 10^{11}\ s^{-1}$) as shown in the Figure 4.14, we do not observe any defect and thus no phase transformation. Such system do not have any thermally activated elementary process. The resulting structure is simply a fct lattice structure; a type of coincidence lattice. It means that there is not enough time for defect formation (in MD ps time scale) and the resulting equilibrium structure is not the product of phase change. The resulting fct structure is confirmed by the radial distribution function calculation (top curve in the Figure 4.14) and from CAT[33] analysis. From the beginning, we predicted different kinetics of phase transformation for compression along (110) direction. We observed that all strain rates provided enough time for heterogeneous nucleation which seeds fcc$\longrightarrow$bcc phase change. One of such time snapshot of quasi-isentropic compression is given in the Figure 4.21.

Density of dislocation on a given glide plane gives information about the dislocation distribution. The total dislocation density is defined as the ratio of total length of dislocation lines divided by the volume of the computational box. For quasi-isentropic compression along (110) at the rate of $\dot{\epsilon} = 10^{11}\ s^{-1}$ in the Figure 4.22, shows that bcc phase growth co-relates with annealing rate of fcc dislocation density. As we know that the microstructure is strongly affected by the rate of compression, we believe that one can co-relate dislocation density with daughter phase grain-size as the defects formed initially in the parent phase (fcc phase) anneal out in the daughter phase (bcc phase). Also at lower temperature, grain growth is reduced, and at slow compression rate one could expect fine-grain structure. And at higher compression rate, one should expect coarse-grain structure.

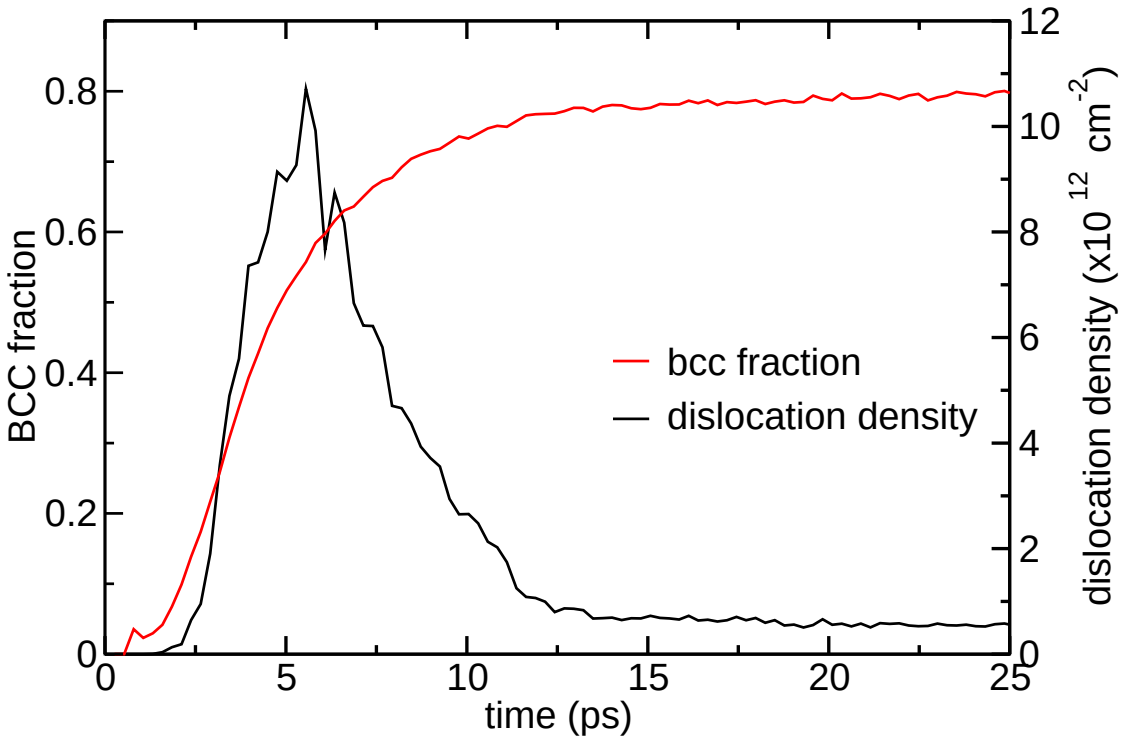

Figure 4.29: Defect density and bcc-fraction as a function of time for quasi-isentropic compression for (110) at rate of $\dot{\epsilon} = 10^{11}\ s^{-1}$.

Finally, we examined shock temperatures of the ZM model potential for shock wave propagation along the low index directions: (100), (110) and (111). From the melt curve Figure 4.4, and Figure 4.17, we predicted the fcc-bcc boundary for shock along (100) and (110) to be at different temperatures. The equilibrium melt curve (fcc and bcc) of the ZM model potentials was determined from solid-liquid co-existence simulations[?] over a pressure range between 0-100 GPa. The results were fitted to a Simon-type equation,[31] $T_m(P) = T_0(1 + P/\alpha)^\beta$ for each phase. The phase which melted at the higher temperature was chosen as the most stable phase and the intercept of the fcc and bcc melt lines was identified as the triple point for this system[32]. The main purpose of this part of our study was to investigate the effect of defect morphology and single-crystal plasticity on the phase

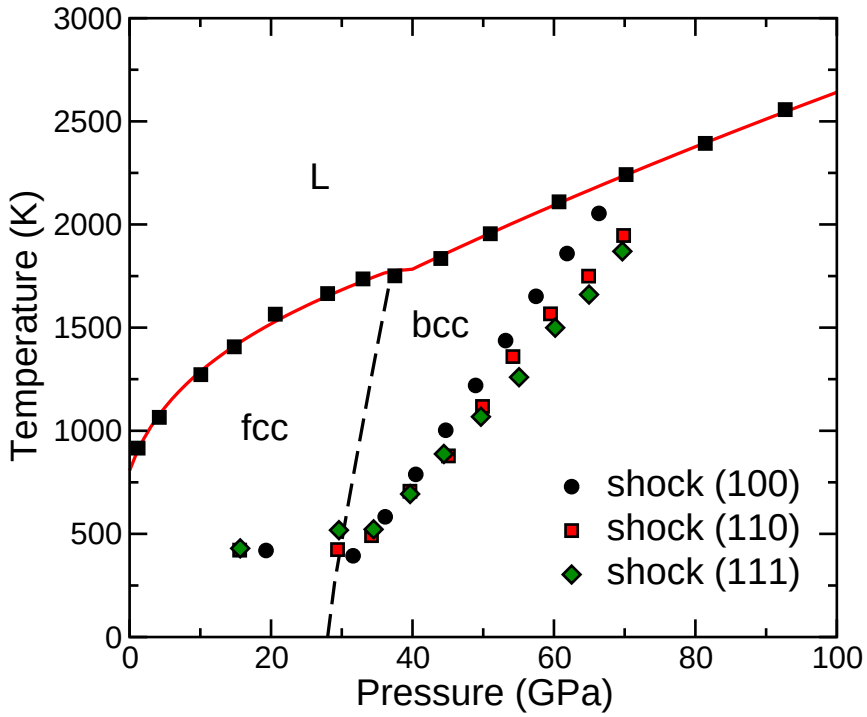

Figure 4.30: Equation of state for ZM potential compared with shock temperatures along (100), (110) and (111) directions.

transformation. We found that all shock temperatures for (100), (110) and (111) shock propagation are lower than temperature of fcc crystal below phase transition (PT = 27 GPa). The fcc-bcc phase change occurs at much higher temperature for shock along (111) than for shocks along (110).This difference in shock temperature along (100) and (110) suggest that the defect formation during shock propagation through crystal resulted in structural phase transition via different modes.

4.4 Summary and Conclusion

We have studied the plastic-deformation mechanism and its role in phase transformation due to shock-wave using NEMD and high strain-rate compression via quasi-isentropic simulations of ZM model potential for different low index directions. Particularly, we looked at (100) and (110) directions. We also performed quasi-isentropic compression. We observed that plastic deformation precedes phase transition along (110) direction. However, along (100), we observed anomalous phenomena. At low strain rate regime ($\dot{\epsilon} = 10^9\ s^{-1}$), fcc$\longrightarrow$bcc transformation takes place. However, for fast strain rate regime ($\dot{\epsilon} = 10^{10} - 10^{11}\ s^{-1}$), crystal structure exhibit fct structure and no phase change is observed. Finally, we examined shock temperatures of the ZM model potentials for (100) and (110) and (111) orientations, and investigated the effect of defect morphology and single-crystal plasticity on the phase transition.

References

[1] K. Kadau, T. Germann, P. Lomdahl, and B. Holian, Science **296**, 1681 (2002).

[2] V. Dupont and T. Germann, Phys. Rev. B **86**, 134111 (2012).

[3] N. Gunkelmann, E. Bringa, D. Tramontina, C. Ruestes, M. Suggit, A. Higginbotham, J. Wark, and H. Urbassek, Phys. Rev. B **89**, 140102 (2014).

[4] C. Truesdell and R. Toupin, in *Principles of Classical Mechanics and Field Theory / Prinzipien der Klassischen Mechanik und Feldtheorie*, Encyclopedia of Physics / Handbuch der Physik, Vol. 2 / 3 / 1, edited by S. Flgge (Springer Berlin Heidelberg, 1960) pp. 226–858.

[5] T. Barron and M. Klein, Proceedings of the Physical Society **85**, 523 (1965).

[6] C. Zener, *Elasticity and Anelasticity of Metals* (University of Chicago Press, 1956).

[7] M. Allen and D. Tildesley, *Computer Simulation of Liquids* (Clarendon Press, New York, NY, USA, 1989).

[8] S. Nosé, Molecular Physics **52**, 255 (1984).

[9] D. Young, *"Phase Diagrams of the Elements"* (University of California Press, 1991).

[10] R. "Ravelo, B. Holian, and T. Germann, "AIP Conference Proceedings" **"1195"** ("2009").

[11] R. Zope and Y. Mishin, Physical Review B **68**, 024102 (2003).

[12] J. Maillet, M. Mareschal, L. Soulard, R. Ravelo, P. Lomdahl, T. Germann, and B. Holian, Phys. Rev. E **63**, 016121 (2000).

[13] R. Ravelo, B. Holian, T. Germann, and P. Lomdahl, Phys. Rev. B **70**, 014103 (2004).

[14] B. Holian, A. Voter, N. Wagner, R. Ravelo, S. Chen, W. Hoover, C. Hoover, J. Hammerberg, and T. Dontje, Phys. Rev. A **43**, 2655 (1991).

[15] M. S. Daw and M. Baskes, Phys. Rev. B **29**, 6443 (1984).

[16] M. Finnis and J. Sinclair, Philosophical Magazine A **50**, 45 (1984), http://www.tandfonline.com/doi/pdf/10.1080/01418618408244210 .

[17] F. Ercolessi and J. Adams, EPL (Europhysics Letters) **26**, 583 (1994).

[18] J. Angelo, N. Moody, and M. Baskes, Modelling Simul. Mater. Sci. Eng. **3** (1995).

[19] S. Chantasiriwan and F. Milstein, Phys. Rev. B **53**, 14080 (1996).

[20] J. Winey, A. Kubota, and Y. Gupta, Modelling and Simulation in Materials Science and Engineering **17**, 055004 (2009).

[21] Y. Mishin, D. Farkas, M. Mehl, and D. Papaconstantopoulos, Physical Review B **59**, 3393 (1999).

[22] J. Mei, J. Davenport, and G. Fernando, Phys. Rev. B **43**, 4653 (1991).

[23] X. Liu, F. Ercolessi, and J. Adams, Modelling and Simulation in Materials Science and Engineering **12**, 665 (2004).

[24] J. Boettger and S. Trickey, Phys. Rev. B **53**, 3007 (1996).

[25] R. Ravelo, Unpublished.

[26] J. Lubliner, *Plasticity Theory*, Dover books on engineering (Dover Publications, 2008).

[27] A. Montanaro, Journal of Elasticity **46**, 217 (1997).

[28] P. Lomdahl, P. Tamayo, N. Grø nbech Jensen, and D. Beazley, in *Proceedings of Supercomputing '93, IEEE, Piscataway, NJ* (IEEE, 1993).

[29] K. Kadau, T. Germann, and P. Lomdahl, International Journal of Modern Physics C **17**, 1755 (2006).

[30] R. Ravelo, T. Germann, O. Guerrero, Q. An, and B. Holian, Phys. Rev. B **88**, 134101 (2013).

[31] F. Simon and G. Glatzel, Zeitschrift fr anorganische und allgemeine Chemie **178**, 309 (1929).

[32] L. Burakovsky, S. Chen, D. Preston, A. Belonoshko, A. Rosengren, A. Mikhaylushkin, S. Simak, and J. Moriarty, Phys. Rev. Lett. **104**, 255702 (2010).

[33] A. Stukowski and K. Albe, Modelling and Simulation in Materials Science and Engineering **18**, 085001 (2010).

Appendix A

Evaluation of Second Order Elastic Constants

The following derivations follow closely those in Ref.[19]. Within the potential approximation, we can consider the dependency of elastic free energy per unit mass, $G(\eta)$ on only the Lagrangian strain matrix η_{ij}. The Taylor series expansion of $G(\eta)$ about the unstressed state (reference state) gives

$$\rho_0 G(\eta) = \rho_0 G(0) + \frac{1}{2} c_{ijkl}\eta_{ij}\eta_{kl} + \frac{1}{6} c_{ijklmn}\eta_{ij}\eta_{kl}\eta_{mn} + ..., \tag{A.1}$$

where ρ_0 is the density at the reference state and the standard summation convention is employed ($i, j, k, l = 1, 2, 3$). Using the Voigt notation, we can write c_{1122} as C_{12} and so on and η_{11} with η_1, etc., we get

$$\rho_0 G(\eta) = \rho_0 G(0) + \frac{1}{2}\sum_{I=1}^{6} C_{II}\eta_I^2 + \sum_{I<J} C_{IJ}\eta_I\eta_J + \frac{1}{6}\sum_{I=1}^{6} C_{III}\eta_I^3 + \frac{1}{2}\sum_{I\neq J} C_{IJJ}\eta_I\eta_J^2 + \sum_{I<J<K} C_{IJK}\eta_I\eta_J\eta_K + ... \tag{A.2}$$

Correspondingly, nth-order elastic moduli $C_{IJKL...}$ are defined as

$$C_{IJKL...} = \frac{1}{\Omega_0}\left(\frac{\partial^n G}{\partial\eta_I \partial\eta_J \partial\eta_K ...}\right) \tag{A.3}$$

where Ω_0 is the volume per atom at the reference state. Here the elastic energy G corresponds to the configurational energy E in the EAM format. To evaluate the above derivatives, $\frac{\partial}{\partial\eta_I}$ are expressed in terms of $\frac{\partial}{\partial r}$, where r is the distance between lattice points in the crystal. For $\boldsymbol{r}(= x_1\boldsymbol{i} + x_2\boldsymbol{j} + x_3\boldsymbol{k})$ and $\boldsymbol{r}_0$ are lattice vectors in the strained and

unstrained crystals respectively, where x_i represents the Cartesian component of $\boldsymbol{r}$ in the ith direction. Now the magnitude of the difference of lattice vectors is give by

$$r^2 - r_0^2 = 2\sum_{I=1} X_I \eta_I \tag{A.4}$$

where, $X_I = x_i x_j$ and I is the Voigt contraction of ij. Now, within the framework of EAM, second-order elastic moduli are calculated as follows:

$$\Omega_0 C_{IJ} = F''(\sum \frac{X_I f'}{r})(\sum \frac{X_J f'}{r}) + F' \sum \frac{X_I X_J}{r^2}(f'' - \frac{f'}{r}) + \frac{1}{2}\sum \frac{X_I X_J}{r^2}(\phi'' - \frac{\phi'}{r}) \tag{A.5}$$

where F' and f' are the derivatives w.r.t. ρ and r respectively. For a crystal of cubic symmetry, the expression for the three independent second-order elastic moduli are written as:

$$\Omega_0 C_{11} = F''(\sum \frac{x_1^2 f'}{r})^2 + F' \sum \frac{x_1^4}{r^2}(f'' - \frac{f'}{r}) + \frac{1}{2}\sum \frac{x_1^4}{r^2}(\phi'' - \frac{\phi'}{r}) \tag{A.6}$$

$$\Omega_0 C_{12} = F'' l(\sum \frac{x_1^2 f'}{r})^2 + F' \sum \frac{x_1^2 x_2^2}{r}(f'' - \frac{f'}{r}) + \frac{1}{2}\sum \frac{x_1^2 x_2^2}{r^2}(\phi'' - \frac{\phi'}{r}) \tag{A.7}$$

$$\Omega_0 C_{44} = F'' \sum \frac{x_1^2 x_2^2}{r^2}(f'' - \frac{f'}{r}) + \frac{1}{2}\sum \frac{x_1^2 x_2^2}{r^2}(\phi'' - \frac{\phi'}{r}) \tag{A.8}$$

The summation in the above equations are taken over atoms j around the reference atom i such that $i \neq j$.

Curriculum Vitae

Punam Ghimire was born and raised in Nepal. She graduated from high school in Nepal in 2006 at Bharabi Science Acadmy from Dharan-1, Sunsari Nepal. In 2007, she received an scholarship from the Indian government to pursue her Bachelor of Science at autonomous institution Mount Carmel College (MCC), in Bangalore, India. She had the opportunity to meet many other international students and explore different parts of India. While at MCC, she served as an executive member for the Federation of International Students' Association- Bangalore (FISA-B) from 2007-2010. In 2008-2009, she served as vice-president of the Foreign Student Association at MCC. She received her Bachelor of Science in 2010 from MCC with triple majors in Physics, Chemistry and Mathematics, and in 2011 she was accepted at The University of Texas at El Paso (UTEP), USA where she continued her education as an international transfer student. In 2013 she received her Bachelor of Science in Physics from UTEP and in 2015 she received her Masters of Science in Physics. While student at UTEP, she worked as a teaching assistant/research assistant.

Email: punamg@me.com